

General Disclaimer

One or more of the Following Statements may affect this Document

- This document has been reproduced from the best copy furnished by the organizational source. It is being released in the interest of making available as much information as possible.
- This document may contain data, which exceeds the sheet parameters. It was furnished in this condition by the organizational source and is the best copy available.
- This document may contain tone-on-tone or color graphs, charts and/or pictures, which have been reproduced in black and white.
- This document is paginated as submitted by the original source.
- Portions of this document are not fully legible due to the historical nature of some of the material. However, it is the best reproduction available from the original submission.

8 "Made available under NASA sponsorship
in the interest of early and wide dis-
semination of Earth Resources Survey
Program information and without liability
for any use made thereof."

Pt 1

NASA CR-

144642

A PHOTOGEOLOGIC COMPARISON OF SKYLAB AND LANDSAT IMAGES

E7.6-10251

OF SOUTHWESTERN NEVADA AND SOUTHEASTERN CALIFORNIA

Prim. Invest.?

by

D. W. O'Leary

and

H. A. Pohn

(E76-10251) A PHOTOGEOLOGIC COMPARISON OF
SKYLAB AND LANDSAT IMAGES OF SOUTHWESTERN
NEVADA AND SOUTHEASTERN CALIFORNIA Final
Report (Geological Survey) 79 P HC \$5.00

N76-20598

Unclas
00251

CSCL 08B G3/43

Part I, Final report of EREP Investigation 487

Branch of Petrophysics and Remote Sensing

U.S. Geological Survey

Denver, Colorado 80225

Original photography may be purchased from:
EROS Data Center
10th and Dakota Avenue
Sioux Falls, SD 57198

Abstract

A comparison of Skylab and Landsat (formerly ERTS) images of the area around Goldfield, Nev., shows that for photogeologic interpretation of basin-and-range terrain the Skylab images are generally superior. The images provide geological data restricted to surficial or morphological features such as alluvium, playa deposits, bedrock-massif borders, lineaments, and, to an extent, altered-bedrock areas. Bedrock map units or lithologies must be inferred; contacts and actual faults cannot be unequivocally recognized. The spatial resolution of the Landsat images renders them suitable for small-scale morphological studies and lineament analyses.

The Skylab normal-color stereophotos are an excellent source for preparing provisional or preliminary maps of basin-and-range terrains; maps derived from these photos would best show surficial units, borders of major physiographic features, possible faults and contacts, and very broadly inferred lithologic units. These stereophotos have potential limited use in the search for alteration zones. Areas of altered rock may also be accurately recognized in these photos.

For many features, spectral-band images showing the greatest contrast give the most photogeologic information. Individual-band images are not as useful as composite images or normal-color images. The value of photogeologic interpretation depends heavily on the quality of the images used. For lineament analysis a certain amount of graininess or misregistration seems to improve recognition, however.

The images used by us in this study were those commercially available from the EROS Data Center, Sioux Falls, S. D. Of the images available to us for this test area, the most useful for photogeologic analysis in the Skylab system are the normal-color stereopair and the single-band 0.5-0.6 μm image. The most useful images in the Landsat system are the false-color IR image and individual bands 5 and 7. The Skylab normal-color stereopair is especially useful for recognition and mapping of altered areas. When compared with procedures involving image enhancement, analyses based on relationships of pattern, color, topography, and alluvium provide quick and perhaps surprisingly accurate identification of altered areas.

Introduction

This study was made to determine in what ways Landsat (formerly ERTS) images differ from Skylab images as tools for photogeologic interpretation of the area around Goldfield, Nev. Our object was to decide which of the two imaging systems provides more geological information on geologic units, structural features, lineament patterns, and landforms.

As Rowan and others (1974) have amply demonstrated, interpretation of geologic features in this region from Landsat images is potentially of great utility and precision. Accurate photogeologic interpretation of the whole imaged area or of selected features will save considerable time and expense where field work is especially arduous and where access is limited. The main value of unenhanced high-altitude images, such as Skylab photos, is in reconnaissance; they provide an accurate basis on which the geologic relationships of major physiographic features may be reasonably inferred, so that groundwork may be efficiently directed to areas of particular interest. Certain problems must be countenanced, however. In this study these included degraded resolution and poor color balance, probably due to variations introduced by the fact that the prints and negatives were several generations removed from the original images. Lack of good ground control and suitable geologic data for comparison with the interpretations are problems that also influenced our conclusions.

Despite these restraints, a precise photogeologic map of the study area can be produced from these images, although it must be essentially

a physiographic-surficial map. The photogeologic-interpretation product is rated here in relation to spectral and spatial resolution of the images and is compared with published geologic maps to arrive at a general evaluation of accuracy, scope of application, and ease of recognition of pertinent geologic features.

Study area, geologic setting, and images

The study area, shown in Landsat frame E 1324-18005, dated June 1973, includes parts of southwest Nevada and southeast California (fig. 1). The portion of California (Inyo County) includes parts of the Inyo Mountains, the Panamint Range, Grapevine Mountains, and Death Valley (fig. 2); the portion of Nevada (Esmeralda and Nye Counties) includes Mud Lake, the Montezuma Range, the Cactus Range, part of the Kawich Range, and the northern part of the Grapevine Mountains (fig. 2). The principal town in the area is Goldfield, Nev. This region has excellent bedrock exposure and generally clear atmospheric conditions, which prevailed at the time the data were recorded. Vegetal cover is sparse or absent. Control information for the whole area is available in geologic maps of both Nevada and California (Jennings, 1958; Strand, 1967; Stewart and Carlson, 1974).

Physiographically, the study area is characterized by rugged, relatively deeply dissected, fault-block mountain groups. These massifs are more-or-less surrounded and partly buried by alluvial fans and playas. Elevations range from 11,107 feet (3,387 m) on Mt. Inyo, Calif., to -200 feet (-61 m) in Death Valley, Calif. In most cases drainage

is closed or ephemeral. The physiography is shown in detail on the following 2° quadrangles, at scale of 1:250,000: Death Valley, Calif., Nev.; Goldfield, Nev., Calif.; and Tonopah, Nev.

The general geology is that of the Basin-and-Range Province: chiefly clastic and carbonate units variously faulted and tilted and locally intruded or overlain by volcanic rocks. Rocks are present to lesser extent, especially near the California-Nevada border. The massifs are mantled by coalescing alluvial fans and talus cones. These feed down to braided stream washes, which lead to playas, ephemeral lake bottoms floored with clay and evaporites.

The images used from Skylab are the S190-A 70-mm photographs in the following spectral bandwidths: 0.5-0.6, 0.6-0.7, 0.7-0.8, and 0.8-0.9 μm , and a color-IR print. A normal-color stereopair, in which the Skylab-Landsat image overlap delimits the study area, was also included. The corresponding Landsat images are band 4 (0.5-0.6 μm), band 5 (0.6-0.7 μm), band 6 (0.7-0.8 μm), and band 7 (0.8-1.1 μm), and a commercially available color-IR-image composite of bands 4, 5, and 7. Scales of the images are between 1:500,000 and 1:1,000,000. All of the images are paper prints.

Method

Our method of comparing the Skylab and the Landsat images for this study area is basically an item-by-item comparison keyed to data presented in the geologic maps of the area. The items of geological interest are those that can be directly interpreted from the unenhanced

image, defined by a boundary line, and drawn on a map at the scale of the image. Such items are functions of morphology, structure, and material composition. Because only morphology is directly observable—structure and composition can only be inferred from the images—we ought logically to choose landform patterns as the geologic units rather than lithologies or even formations. This approach is especially practical where a good stereoscopic model is available. Otherwise, we are restricted to one- and two-dimensional elements of landforms; i.e., linear elements, represented by such features as gorge bottoms, stream segments, scarp edges, ridge crests and other slope divides, and straight boundaries between surfaces of different texture, and planar elements of distinct textural and tonal character, such as various kinds of slopes and shapes. Morphological units (features made of two or more slopes) are of two general kinds: erosional landforms (inselbergs and massifs) and depositional landforms (volcanic flows and cones, playas, and alluvial fans). The kinds of photogeologic features considered in this study are listed in Table 2, along with appropriate features shown in geologic maps.

The features recognized and defined in the images were drawn on an overlay map. Because of uncertainties in the mapped geology, devising an objective statistical test to evaluate these data, except for the lineament data, was impossible. The lineament analysis was done by one operator. To minimize increased recognition of features due to familiarity with the image pattern and, hence, uncontrolled bias, lineaments were recorded over a three-week period and each

image was accorded the same amount of time during analysis.

Nevertheless, a "learning" effect developed and a rough correlation exists (Table 1) between the order of mapping and the number of lineaments per image correlated with mapped faults compiled from the State maps.

Photogeologic observations

The following paragraphs summarize comparisons of each kind of mapped feature observed in the images. An evaluation of the images with respect to each feature is given.

Playas- Recognition and shape discrimination of playas was better in the normal-color Skylab images than in the Landsat color composite, because of the better spatial resolution, the color contrast, and the stereomodeling.

Twenty playas were recognized in each of the Skylab images (fig. 3). Of the single-band photos, the 0.5-0.6 band image provides the best discrimination because of high tonal contrast in this band; recognition in other photos was difficult because of lower contrast and excessive graininess. Thirty-two playas were identified in each Landsat image (fig. 4); of these images, bands 4 and 5 provided the greatest ease of recognition because of the greater tonal contrast. On the other hand, tonal variations in the larger playa surfaces are shown in bands 6 and 7. These variations indicate subtle contrasts in texture and, probably, moisture content. All 20 playas recognized in the Skylab images were among those recognized in the Landsat frames.

Fifteen playas are shown on geologic maps of the study area. It was determined that 27 of the 32 Landsat-identified playas were spurious: some highly reflecting material other than playas led to misidentification. Of the 20 Skylab-identified playas, 6 were misidentified for the same reason. One playa shown on the geologic map was not recognized in these photos. Clearly, the Skylab photos are a superior source for identifying playas in basin-and-range terrain.

Alluvium - Source maps for the California State map distinguish among different kinds of alluvium, but the compiled maps show it as a single general unit. The images all allow recognition of stream-laid alluvium versus cone, talus, or fan deposits (figs. 3 and 4), and the relationships correspond with those mapped on the California quadrangles. In general, the Skylab photos provide the better discrimination because of superior spatial resolution. Spectrally, the two systems seem to respond differently: the Landsat band-5 image is the best of the Landsat bands for distinguishing alluvium, but the Skylab frame 0.5-0.6 is the best of the Skylab bands. The quality of the 0.6-0.7 frame in the Skylab series (which corresponds to Landsat band 5) is poor, probably because of a processing irregularity; however, the cause is uncertain as a valid band-to-band comparison between the two systems was not possible. Of all the images, the Skylab normal-color stereopair is the best, because of excellent chromatic contrast and the stereomodel.

Bedrock areas - Bedrock boundaries drawn from the Landsat images (fig. 4) are more deeply embayed and circumscribe smaller areas than

do those drawn from the Skylab photos (fig. 3), owing to the low tonal contrast between much of the alluvium (talus deposits) and the adjacent bedrock. Because much of the distinction depends on texture, the relatively low spatial resolution of the Landsat images puts them at a disadvantage. Thus, a conservative estimate of bedrock areas tends to err in favor of alluvium. The boundaries observed from the Skylab color photos show the best correspondence with mapped contacts. The borders were recognized in these photos by the additional tonal and color contrast and by the stereorelief. The stereorelief is especially helpful because of the sharp morphological distinction between bedrock and alluvium. However, bedrock with very shallow fan cover (pediments), bedrock with albedo similar to adjacent fan deposits, rotten or disaggregated bedrock with surface texture similar to alluvium, and small, scattered outcrops below the spatial resolution of the sensor were included as alluvium. In the California portion of the area, for example, younger nonmarine units are not distinguishable from older nonmarine units, because these units have spectral characteristics similar to those of recent alluvium and have no significant physiographic expression (Jennings, 1958).

Of the Landsat images, the false-color composite and band 5 offer the best tonal contrast for determining outcrop boundaries. Band 5 has the better tonal contrast, but it suffers from striping. By far the best images for bedrock definition are the Skylab normal-color stereopair. The color-IR print offers very poor tonal contrast, and the individual band images are too grainy or have low tonal contrast.

Bedrock units - In the Nevada portion of the study area, geologic units interpreted from both Skylab and Landsat images show no relationship to units presented on the State map, because the map units do not represent unique, spectrally distinctive lithologies. In the California portion, however, the Skylab photos provide surprisingly good identification of contacts but not lithologies. Photogeologic units are distinguished according to texture, tone, and color. The volcanics are particularly easy to recognize in both Landsat and Skylab photos, because of their distinctive morphology and dark tone and color (figs. 3 and 5). Band 4, Landsat, is an inferior image for this purpose, however; band 0.5-0.6 is the best of the Skylab group. Not all recent volcanics shown on the maps were recognized in the images because of variations in image quality. Some features interpreted as volcanics cannot be confirmed, because they fall in unmapped areas on the geologic maps; others appear to have been incorrectly identified, probably because they are located near the edges of images, where resolution fall-off occurs.

Contacts in the Grapevine Mountains are particularly well distinguished in the Skylab normal-color images (fig. 3). In the area south of Dry Mountain, at the west end of the Cottonwood Mountains, Precambrian and Pennsylvanian units are well defined. In the Inyo Mountains, along the west side of Eureka Valley, two contacts between Cambrian and granite units are identified. And at the north end of the Last Chance Range, the Furnace Creek fault zone and a contact between granite and Cambrian rock is well defined. The recognized

contacts separate map units of broadly different lithologies and textural and (based on the stereomodel) morphological expressions.

Low tonal contrast hampered attempts to identify geologic units from the Landsat images. Volcanics are fairly well defined on the images (fig. 5), but the shapes and locations of many volcanics are not accurately determined.

For these data, the Skylab normal-color photos have the best contrast, and the color-IR photo, the worst. Spectral resolution in the individual band images is too low to be useful for discriminating bedrock units both in the Skylab and in the Landsat images.

Lineaments - Most of the lineaments interpreted from the Skylab and Landsat images do not correspond to mapped faults, chiefly because the mapped faults are short segments within massifs or along borders of massifs and alluvium, whereas the lineaments include features outside of massifs. Lineaments that coincided with mapped faults were counted in each of the 11 images. Results are shown in Table 1.

The Skylab black-and-white images appear to be more useful than the Landsat images for mapping lineaments, probably because of the higher contrast, which produces sharp grain edges on the Skylab images, and because of the higher resolution of the Skylab images. However, the Landsat color-IR image appears to be superior for this purpose to either the Skylab color-IR or normal-color photos, possibly because of the slight edge enhancement caused by imperfect registration of the three bands used to produce the Landsat false-color composite.

General summary - The Skylab stereophotos are recommended for

use in making surficial geologic maps and for making preliminary geologic maps in arid terrains, in which the map units include areas of bedrock exposure, playas, alluvial fans, stream-laid alluvium, and lineament patterns. In other areas, dune deposits, swamp deposits, and glacial deposits may be defined. Broadly defined lithologic contacts may be outlined from these photos, and, to an extent, preliminary identification of altered areas in arid regions may be achieved.

Interpretations and restrictions

Our interpretations depended directly on the spatial and spectral characteristics of the images used here. The Skylab photos have a relatively high spatial resolution (30 to 75 m), whereas the Landsat resolution is lower (80 m). Because of the better spatial resolution and the excellent stereomodel offered by the Skylab photos, they are superior sources of physiographic data. The high resolution is not necessarily of value for recognizing the extent and position of lineaments and other features that compose a large number of resolution elements. Neither image system provides a superiority in shadow enhancement, as there is only a 4° difference in sun-elevation angles between the images (62° for Landsat, 66° for Skylab). Likewise, where similar bandwidths are covered, spectral resolution is similar in the multiband images for both systems. The Skylab normal-color photos offer the advantage of good resolution combined with the enhanced visual discrimination of color tones relative to gray tones. The spectral contrast of the Skylab color-IR photo, on the other hand, is low; and the photo is not particularly useful.

Despite the general utility of Skylab color photos, both Skylab and Landsat data have serious limitations. Our interpretations of the images, or of the photogeologic units, led to a geomorphic synthesis of the study area. We found that, though useful, the geologic information contained in each kind of image was not suitable for making a geologic map of the area and was only marginally useful for improving the information already contained in the maps for two reasons: (1) conventional geologic maps depict lithologic units, which are not unequivocally identifiable in Skylab or Landsat images, and (2) most lineaments, to be documented as fault traces, must be field-checked. Alteration effects are best displayed in a special-purpose map ordinarily made in the interests of economic geology. The Nevada State map, for example, is a preliminary compilation; the map units are essentially lithologic units grouped according to broad compositional and textural distinctions; e.g., "Intrusive rocks: aphanitic, porphyritic, and granitic rocks ranging in composition from diorite to granite," or "Ash-flow tuffs, rhyolite flows, and shallow intrusive rocks." The correlation of units based on wide ranges of origin, grain size, and bulk composition with units based on spectral reflectance is virtually impossible.

An attempt was made to evaluate the geologic data control in the regional maps. An examination of the Mina quadrangle (Ferguson and others, 1954), a good example of detailed mapping in the study area, revealed the same inadequacies. A sparsity of attitude symbols in the central and southwest quarter of the map indicates poor control

for structural interpretation; fault mapping is inadequate throughout most of the map area. Map units embrace abrupt facies changes and changes of metamorphic grade, such as "sandstone (tuffaceous in part), shale, calcareous marl, limestone, diatomite and local basalt conglomerate. Locally interbedded rhyolite tuff is present."

Crystalline units, based on a broad range of compositions, are lumped. Intrusive rock units, for example, contain rocks ranging from granite to gabbro to serpentine.

Two source maps in the California section were examined (Blackcap Mountain quadrangle, Bateman, 1965; Blanco Mountain quadrangle, Nelson, 1966). These maps show units grouped according to origin and age (i.e., marine vs nonmarine) but not according to lithology. In some areas, units mapped by reconnaissance are sharply juxtaposed with units mapped by detailed work, with blank "unmapped" borders. Both of these maps show units and structure in excellent detail. The problem here, however, is too fine a division of units. For example, in the Blackcap Mountain quadrangle, there are four units of quartz monzonite and five units of granodiorite. Individual map units of this sort were indistinguishable in the Skylab and Landsat images; although there is a broad matching of contacts between widely different lithologies, it is impossible to distinguish one granodiorite or one quartz monzonite from another in the images.

Rowan and others (1974), faced with the same problem but with considerably superior image data, compared an "excellent color photograph" obtained from the S-190 photographic experiment with a

map showing the distribution of the main rock types. They concluded that the appearance of the rocks in the photo is dominated by albedo, which is not a reliable guide to rock type; the characteristic colors of the rock units are too muted to be consistently shown on small-scale orbital photographs. Further, except for a few small limonitic altered areas southeast of Stonewall Mountain, Nevada, the mineralized areas are not distinctive in the Skylab photograph. Rowan and others noted that rock-type discriminations on the standard Landsat MSS images are severely limited, even if only a two-component classification system of mafic and felsic rocks is used; spectral-reflectance differences among rock types and between altered and unaltered rocks are generally too small to be detected by visual comparison of the MSS images or through analysis of color-IR composites.

The comparative study of Skylab and Landsat images for the purpose of lineament analysis does not make optimum use of the better resolution of the Skylab system. If all the resolvable lineaments were portrayed, the resulting illustration would show a cloud of lines representing lineaments tens to hundreds of metres in length. In order to deal with a manageable amount of data, lineaments in the analysis were limited to an arbitrary minimum length of 3 km.

A systematic study of lineaments shows that the percentage of lineaments that coincide with mapped faults differs according to the images used for data. This variation is due chiefly to the effects of contrast, photographic grain, and edge enhancement. Visual inspection of the photos shows that the Skylab photos are generally

higher in contrast than the Landsat images. So many steps of photo processing have occurred between the original data and the images used for the analysis, that it is impossible to determine whether the higher contrast is due to inherent properties of the systems or is a product of the photographic-reproduction process. However, the Landsat prints have to be considered as an example of what the user can expect in the way of working materials. A subjective judgment is that, in general, the Skylab prints used in this study appear to be grainier than the Landsat images. Sharp grain boundaries in the Skylab photos may actually enhance the contrast associated with most lineaments. Grain boundaries in the Landsat images appear to be soft. Edge enhancement is important in the Landsat false-color composite, where a slight misregistration of three separate images is present. A close examination of this print shows that the misregistration is due to both a shift in registration of the bands and a slight scale change from band to band. This effect of broadening individual lines seems to facilitate recognition of a greater number of lineaments than can be observed on the individual band images.

Although spectral resolution figures in the recognition of lineaments, this phenomenon is also difficult to evaluate. Because of decreased scattering at longer wavelengths and hence better atmospheric penetration and concomitant blacker shadows, we would expect more lineaments to be recognized on longer wavelength images. In fact, this may be reflected in the Landsat data in Table 1, although the small increase in lineament recognition with wavelength may not be statistically significant.

Further potentials for photogeologic analysis

Practical applications of satellite-image data have yet to be fully explored. Rowan and others (1974) have made impressive advances using Landsat MSS data in the search for mineralized areas in Nevada, but with respect to using unenhanced images and photogeologic interpretations for this purpose, they are not enthusiastic:

"...preliminary evaluation suggests that small-scale photographs such as the Skylab example, although useful for morphological and structural studies, are not adequate for detecting and mapping mineralized areas" (p. 12). Their objections, however, are based on the use of color as the sole criterion for recognition of alteration; the Skylab stereophoto pair available to us provides us with a variety of diagnostic features.

Critical features in altered areas are related to topography and microrelief. McKinstry (1948, p. 223) pointed out a basic relationship useful in the search for ore deposits:

"In the arid basin-and-range country of the southwestern United States, pediments are specially favorable situations for vein deposits. Whereas the mountains represent in general the more massive and resistant rocks, the pediments develop on those parts of the rock mass which faulting, fracturing, and chemical decay have rendered vulnerable to erosion. It is in just these places that hydrothermal ore deposits are to be expected, not only because zones of structural disturbance are hospitable, but because hydrothermal solutions soften the rocks and because pyrite, by furnishing sulfuric acid, promotes weathering."

Another topographic association occurs where a resistant, unaltered rock overlies altered rock, such as that described by Anderson and others (1965). Based on field work, they suggested a search for

concealed mineral deposits in the area between Stonewall Mountain and Mountain Helen, and north of Mountain Helen where isolated patches of altered rocks are surrounded by the unaltered Thirsty Canyon Tuff. This area is characterized by ridges of gray to red-gray dense, silicified rocks that are bounded by valleys formed in light-gray, pink, and tan, intensely argillized rock. In many places the altered areas abut the tuff and probably extend beneath it.

A search for such altered areas was made on the Skylab normal-color stereopair, which partly overlaps the study area of Rowan and others (1974). Approximately 50 percent of the altered areas that they detected in this restricted area were recognized in the Skylab photos (figs. 6a, b). Other areas included rocks similar in color and weathering to altered materials. Two sites were spotted at the north end of Stonewall Mountain that were not detected on the image of Rowan and others; these sites are marked by mines or prospects. Areas missed were principally those where cloud cover made interpretation very doubtful. Probably more altered areas would have been detected had the scene been cloudless. These areas were identified entirely on the basis of the criteria listed below; during the search no reference was made to the results of Rowan and others. The results obtained in this study indicate that, lacking sophisticated image-enhancement facilities, areas can be located on the photos that are worth investigating on the ground. This approach is quick and rough, but it is cost effective and it extends the usefulness of the raw Skylab images to more geologists. The use of cloud-free photos

printed to maximum sharpness and correct color balance would help greatly in this pursuit.

The criteria used for interpreting altered areas are as follows:

- 1) Pattern: areas show a mottled, "stained," irregular pattern of generally light tones. Borders are typically irregular but are sharp.
- 2) Color: colors are distinct from surrounding rock: typically off-white (clay and silica), pale tan (limonite, sulfate staining) and/or rusty red (hematite). These colors are commonly mottled together.
- 3) Topography: areas are adjacent to harder rock; hence they are recognizably bedrock areas but are rather low. Because of variable resistance of altered products and association with faulting, the areas are topographically rough: highly dissected with a subdued, bumpy, or somewhat deflated appearance. Adjacent hard rock may form an obvious cap over or around such areas, or be present as knoblike outliers.
- 4) Alluvium: As McKinstry (1948) pointed out, such areas are typically adjacent to pediment borders; hence a good deal of distinctive slope wash is present, streaked with the typical alteration colors.

Conclusions

Skylab photographs provide more and better detailed information

at scales useful for topical studies and initial detailed mapping projects in terrain of the basin-and-range type; Landsat images provide a useful small-scale data base to prepare regional geomorphic-tectonic compilations or syntheses where much geologic mapping has already been done. The images are marginally useful in delineating broad areas of distinct lithologies. In most cases it is difficult to reconcile photogeologic information with mapped geology, because individual concepts have gone into making a map and because the definition of a formation is not always compatible with a spectrally distinct lithology as shown on a remote-sensor image. The Skylab photographs are especially valuable because of the excellent stereomodel they provide. On the whole, the most useful photos in the Skylab system are the normal-color stereopair and the single band 0.5-0.6 μm .

The Landsat false-color image and individual bands 5 and 7 are the most useful in the Landsat system for small-scale regional-landform and tectonic-pattern analyses.

Areas of altered rock can be recognized in the Skylab normal-color stereophotos using the criteria outlined in the previous section. The image-enhancement procedure developed by Rowan and others (1974) provides a more objective, machine-controlled process in which spectral information is gained from the images. On the other hand, this machine process causes information on topography and texture to be lost. This lost information is essential to the identification of altered areas through the use of Skylab photos. To make the most of all the information potentially available to the analyst, both

procedures should be used in conjunction. Otherwise, the Skylab photos alone may provide relatively quick and cheap reconnaissance of altered areas.

References cited

- Anderson, R. E., Ekren, E. B., and Healey, D. L., 1965, Possible buried mineralized areas in Nye and Esmeralda Counties, Nevada, in Geological Survey research 1965: U S. Geol. Survey Prof. Paper 525-D, p. D144-150.
- Bateman, P. C., 1965, Geologic map of the Blackcap Mountain quadrangle, Fresno County, California: U.S. Geol. Survey Geol. Quad. Map GQ-428, 1:62,500.
- Ferguson, H. G., Muller, S. W., and Cathcart, S. H., 1954, Geologic map of the Mina quadrangle, Nevada: U.S. Geol. Survey Geol. Quad. Map GQ-45, 1:125,000.
- Jennings, C. W., 1958, Geologic map of California--Death Valley Sheet: California State Dept. Nat. Resources, 1:250,000.
- McKinstry, H. E., 1948, Mining geology: New York, Prentice-Hall, Inc., 680 p.
- Nelson, C. A., 1966, Geologic map of the Blanco Mountain quadrangle, Inyo and Mono Counties, California: U.S. Geol. Survey Geol. Quad. Map GQ-529, 1:62,500.
- Rowan, L. C., Wetlaufer, P. H., Goetz, A. F. H., Billingsly, F. C., and Stewart, J. H., 1974, Discrimination of rock types and detection of hydrothermally altered areas in south-central Nevada by the use of computer-enhanced ERTS images: U.S. Geol. Survey Prof. Paper 883, 35 p.

Stewart, V. H., and Carlson, V. E., 1974, Preliminary geologic map of
Nevada: U.S. Geol. Survey Misc. Field Inv. Map MF-609, 1:500,000.
Strand, R. G., 1967, Geologic map of California--Mariposa sheet:
California State Dept. Nat. Resources, 1:250,000.

Table 1. Percent correlation of lineaments and mapped faults in each Skylab and Landsat image, Goldfield area, Nevada

Skylab S190A images			
Image	% correlation	Order of lineament mapping	Number of lineaments observed
0.5 - 0.6 μm	25.0	8	124
0.6 - 0.7 μm	21.8	9	119
0.7 - 0.8 μm	34.0	10	94
0.8 - 0.9 μm	24.1	11	108
normal color	13.7	1	183
color IR	17.4	2	178
Landsat images			
Image	% correlation	Order of lineament mapping	Number of lineaments observed
0.5 - 0.6 μm (4)	14.2	4	127
0.6 - 0.7 μm (5)	14.8	5	168
0.7 - 0.8 μm (6)	15.4	6	175
0.8 - 1.1 μm (7)	17.6	7	199
false-color IR	22.5	3	193

Table 2. Criteria for recognizing photogeologic features

Photogeologic feature	Criteria	Map unit
1. lineament	location and extent of aligned tonal or topographic features (i.e., streams, gorges, alluvium-bedrock contacts, ridges, textural boundaries, etc.) along straight or slightly curved lines	mapped and projected faults and major unit contacts
2. erosional landforms (bedrock areas - inselbergs)	extent and outline of inselbergs and massifs based on relief (stereo-model) texture, tonal contrast, surface (e.g., drainage) patterns, shadowing, and color	all bedrock units
3. depositional landforms (alluvium: stream deposits, cone deposits, playas)	extent and outline based on texture, tonal and color contrast, surface patterns, and boundary relationships	alluvium, playa deposits
4. lithologic units	delineation and interpretation based on color, tone, texture, boundaries	geologic units (formations)

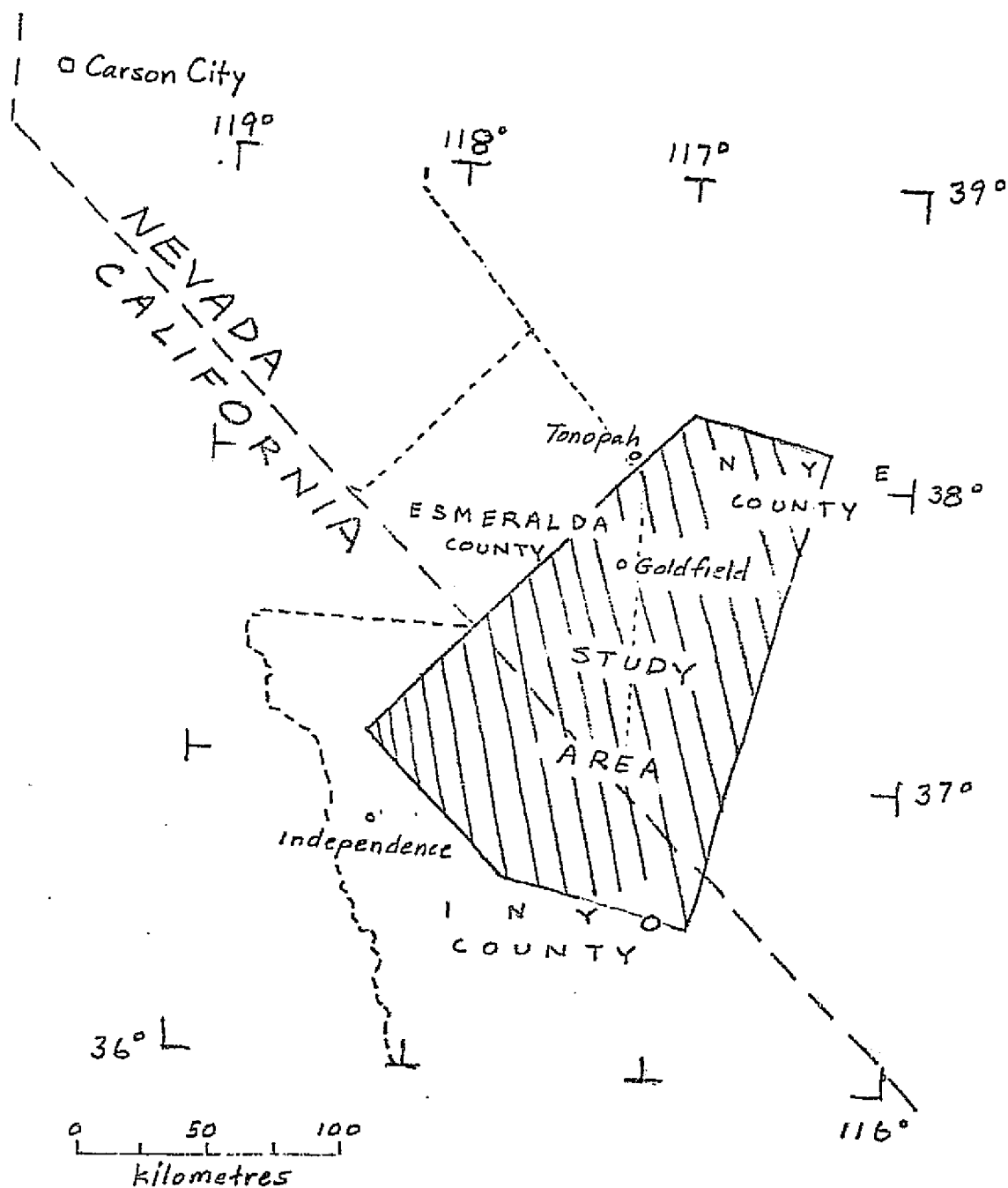


Figure 1. Location and shape of the study area.

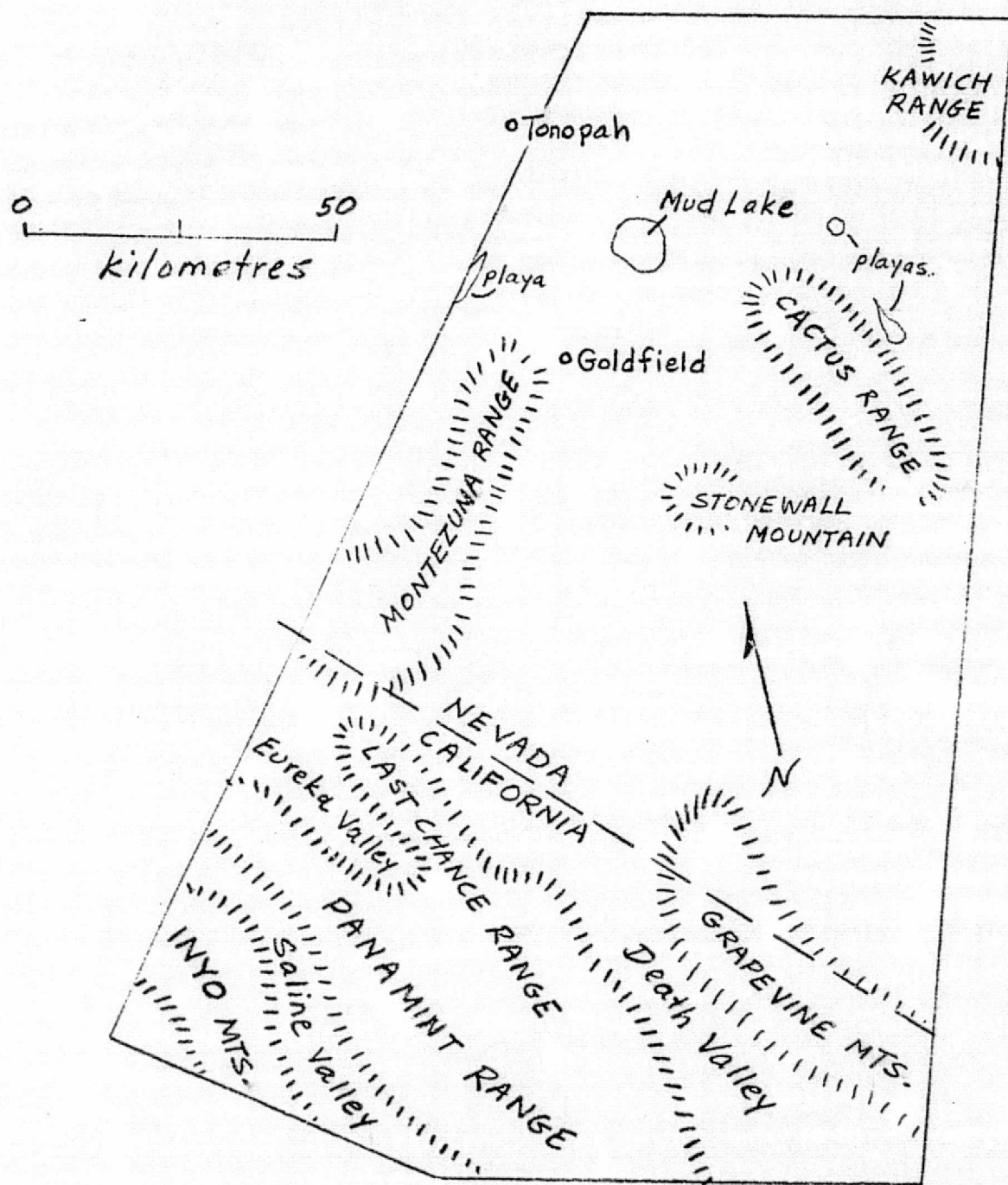


Figure 2. General physiographic features of the study area.

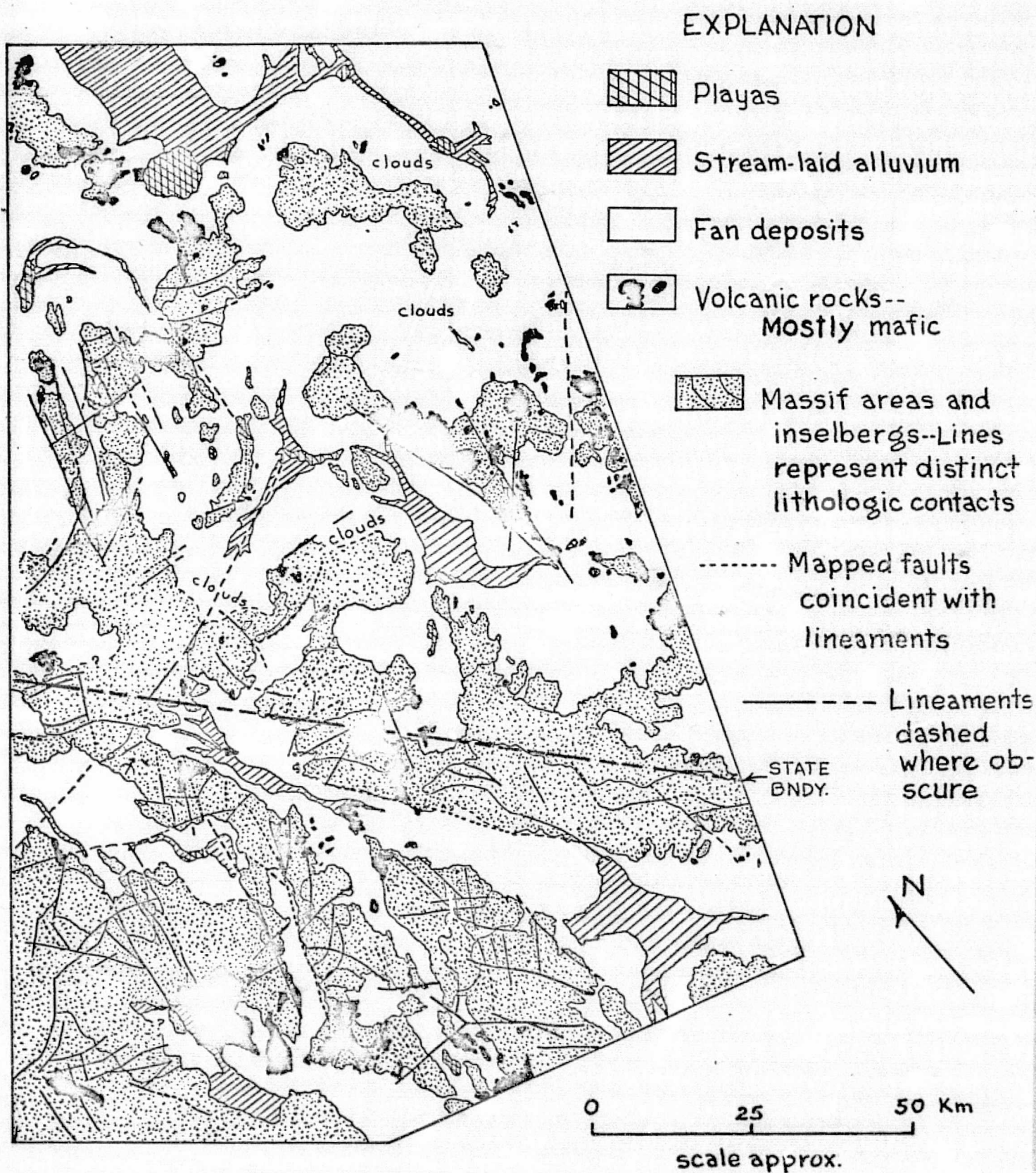
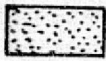


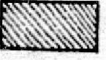
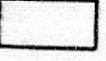


Figure 3. PHOTOGEOLOGIC MAP MADE FROM SKYLAB NORMAL
COLOR STEREO IMAGES

REPRODUCIBILITY OF THE
ORIGINAL PAGE IS POOR

EXPLANATION

-  Massif areas and inselbergs
-  Volcanic rocks-- Mostly mafic
-  Stream-laid alluvium
-  Playas
-  Fan deposits

----- Lineaments--
Dashed where obscure

STATE
BN DY

0 25 Km
SCALE APPROX.

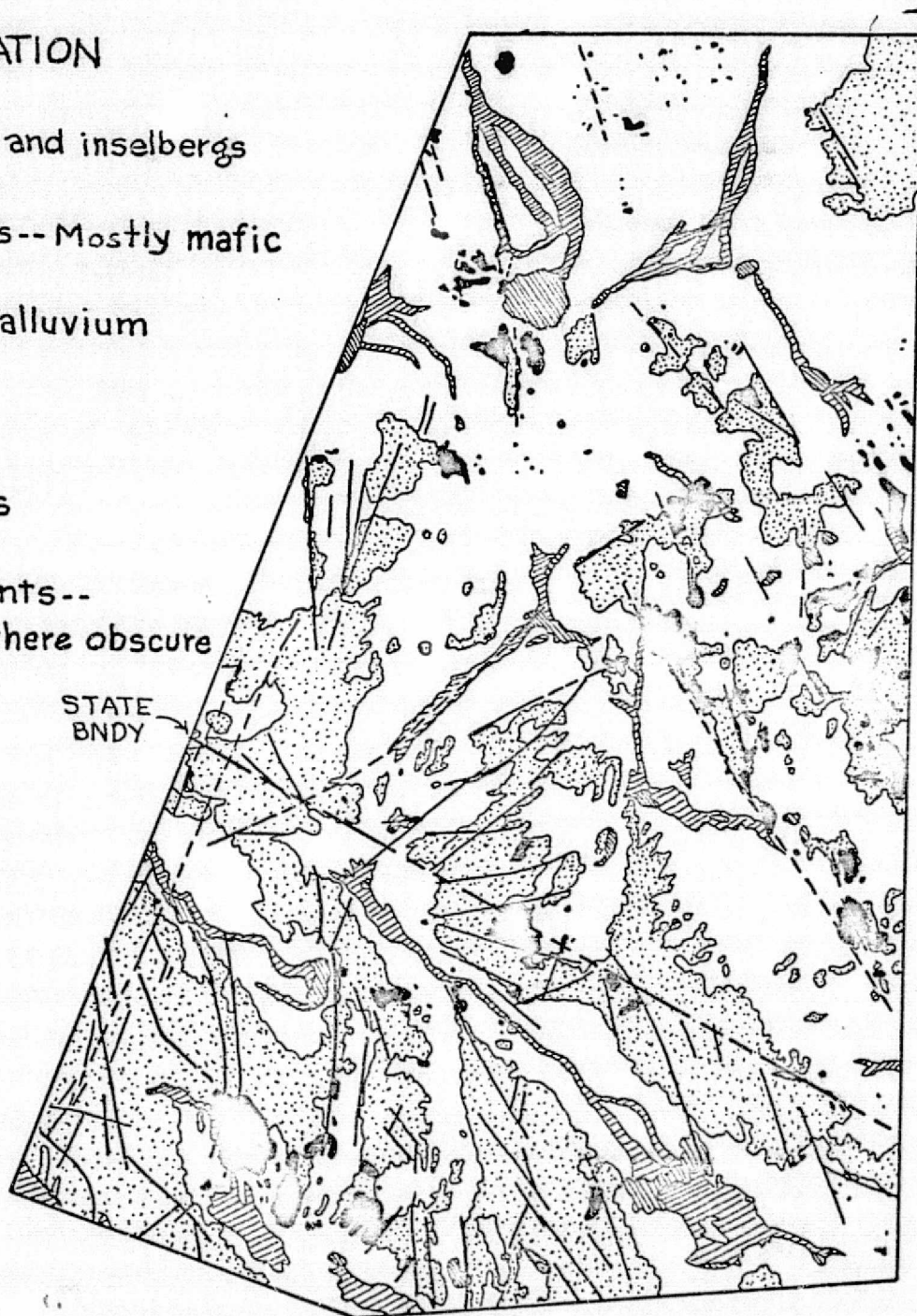


Figure 4. PHOTOGEOLOGIC MAP MADE FROM LANDSAT FALSE-COLOR IMAGE

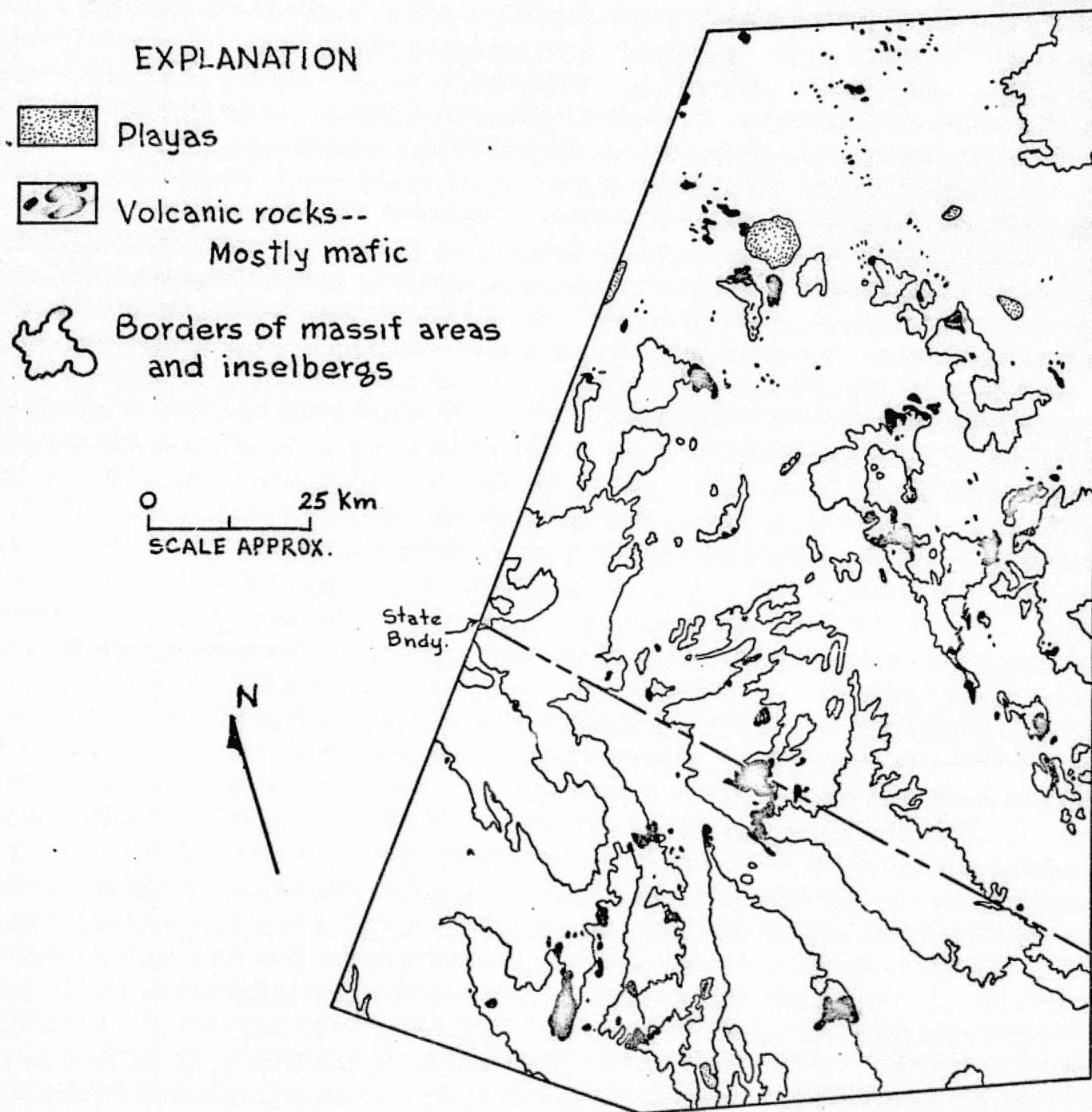


Figure 5. AREAS OF VOLCANIC ROCKS, INFERRED TO BE ALL OR MOSTLY MAFIC, MAPPED FROM LANDSAT BAND 7 IMAGE

REPRODUCIBILITY OF THE
ORIGINAL PAGE IS POOR

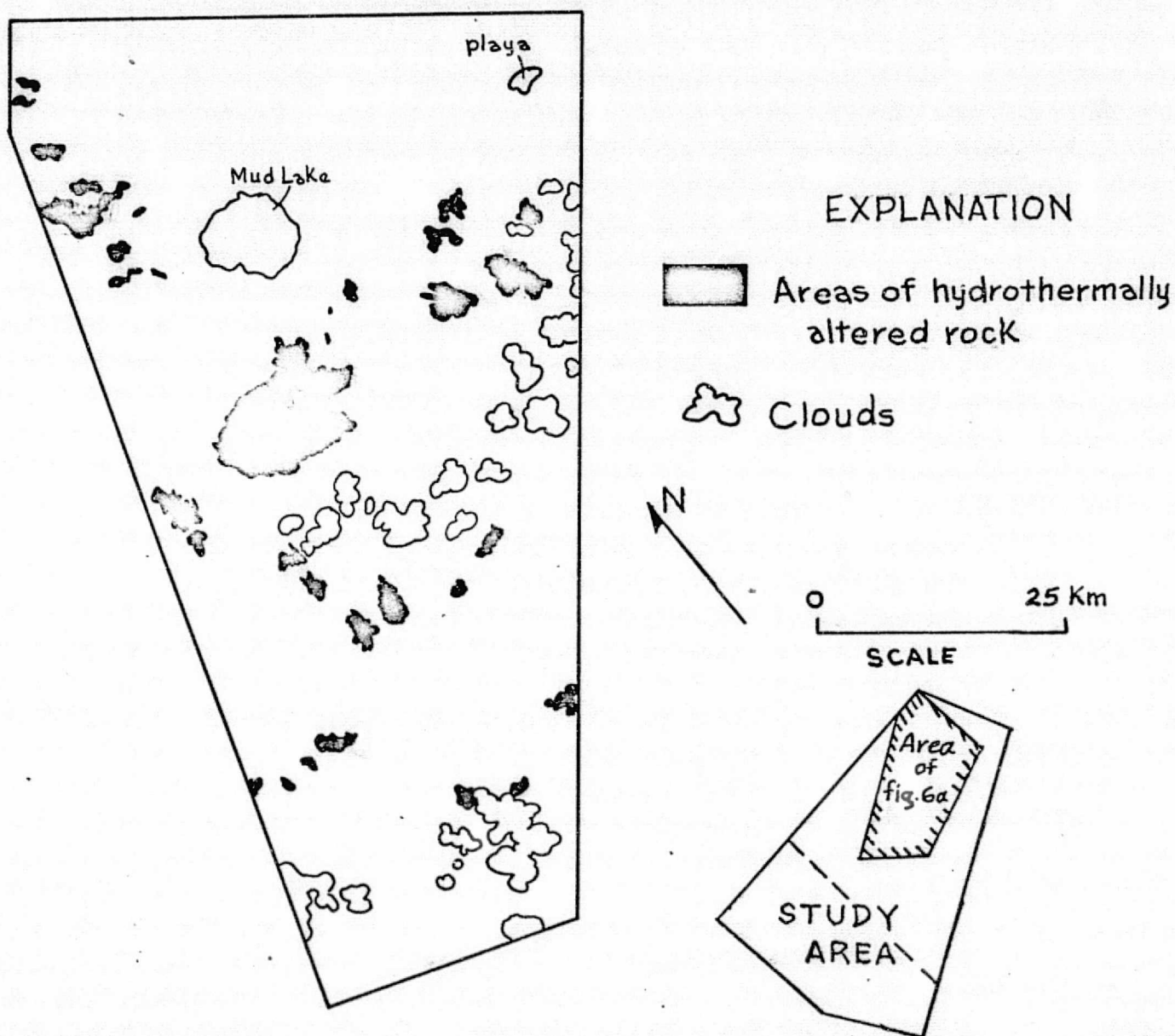


Figure 6a. AREAS OF HYDROTHERMALLY ALTERED ROCK
MAPPED FROM SKYLAB NORMAL COLOR
STEREO IMAGES

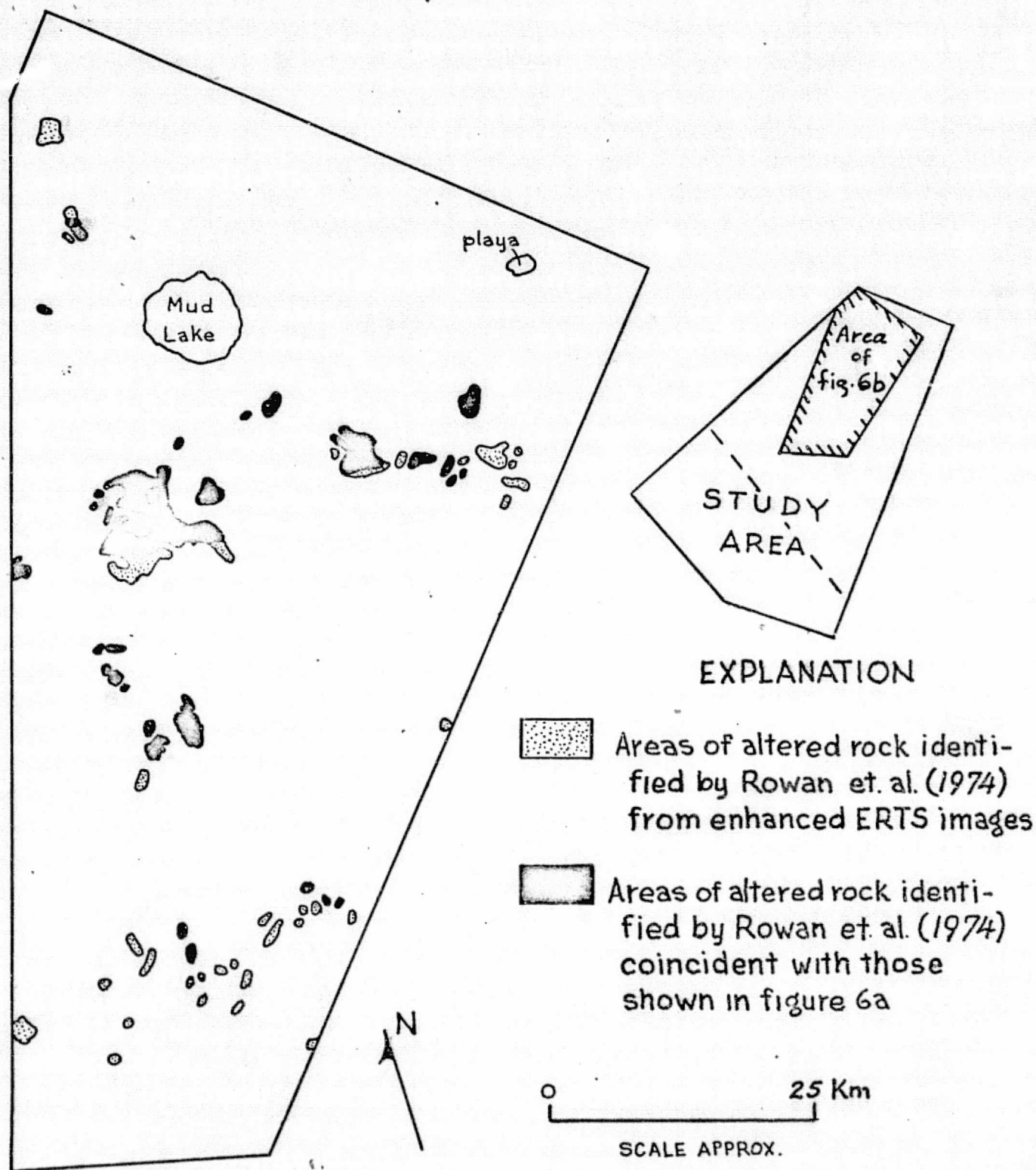


Figure 6b. AREAS OF ALTERED ROCK IDENTIFIED BY ROWAN ET. AL. (1974), COMPARED WITH THOSE IDENTIFIED FROM SKYLAB NORMAL COLOR STEREO IMAGES

Pt 2
"Made available under NASA sponsorship
in the interest of early and wide dis-
semination of Earth Resources Survey
Program information and without liability
for any use made thereof."

Published articles relating to Skylab investigations

Part II, Final report of EREP Investigation 487

Branch of Petrophysics and Remote Sensing

U.S. Geological Survey

Denver, Colorado 80225

Near-Infrared Reflectance Anomalies of Andesite and Basalt in Southern California and Nevada

Howard A. Pohn
U.S. Geological Survey
Denver, Colorado 80225

ABSTRACT

High-reflectivity anomalies in the near infrared (1.0 to 2.6 μm) have been observed on scanner images obtained by the Environmental Research Institute of Michigan (ERIM) in flights over several geologic units in southern California and southwestern Nevada and by the Skylab II mission in flights over western Nevada. These anomalies almost always occur in rocks that are at least as mafic as andesite. The most reasonable explanation for the anomalies is that the anomalous materials have a 5- μm or finer coating of hematite that was formed during cooling and post-eruptive fumarolic steaming.

INTRODUCTION

Prior to the launching of Skylab, the Environmental Research Institute of Michigan (ERIM), in several aircraft missions flown for the U.S. Geological Survey, used a 12-channel infrared scanner to simulate the various channels of the Skylab S-192 experiment. (The S-192 experiment is an optical mechanical scanner that operates in 13 bands located in visible and infrared regions with high atmospheric transmission.) Data from both missions showed near infrared reflectance anomalies of andesite and basalt in southern California and Nevada.

In September 1972, the ERIM 12-channel scanner was flown over six areas believed to be representative of the major geologic units in the proposed southern California-southwestern Nevada Skylab test site. Although operational constraints prohibited surveillance of this particular area by Skylab, a geologically similar test site in western Nevada was overflown by the spacecraft and similar data on reflectance anomalies were obtained.

The ERIM aircraft scanner was flown in a mode that permitted data collection in nine channels in the ultraviolet, visible, and reflective infrared, and three channels in the thermal infrared. Only the eight channels in the visible and reflective infrared (listed on the following page) are discussed in this report.

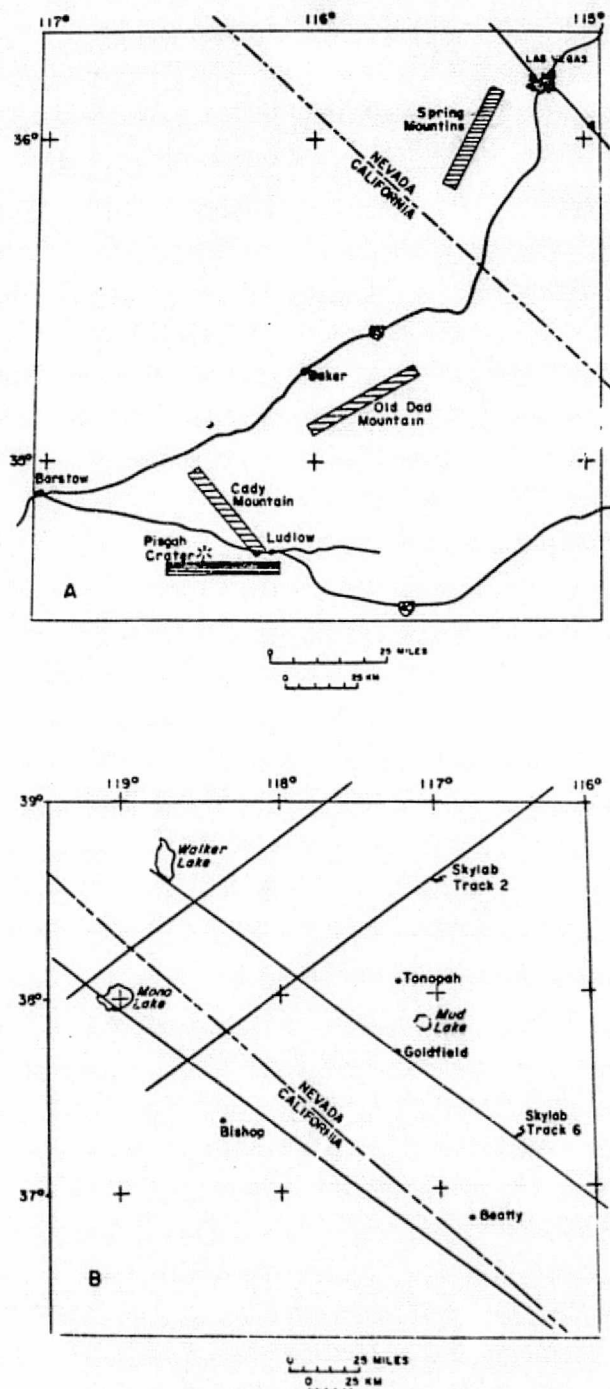


Figure 1. Location maps of test sites: A, four ERIM flight lines in southern California and Nevada; B, Skylab II and III tracks over southwestern California and eastern Nevada.



Figure 2. ERIM scanner images of the cinder cones northeast of Old Dad Mountain: A, channel 6 (0.67 to 0.94 μm); B, channel 8 (1.0 to 1.4 μm); C, channel 9 (2.0 to 2.6 μm).

ticularly common. A location map of four of the six ERIM sites, as well as the Skylab Nevada test site, are shown in Figure 1.

DATA

In the images obtained from the ERIM missions, many small areas of higher or lower reflectivity were noted from channel to channel; however, the most striking contrasts were observed among channels 6, 8, and 9. A typical example is illustrated in Figure 2, which shows an area just northwest of Old Dad Mountain (lat 25° 12' N., long 115° 47' W.). The area is mapped as Quaternary cinder cones underlain by Quaternary basalt (Barca, 1966). The 0.67 to 0.94 μm channel image is similar to the visible channel images; that is, the low reflectivity of the cones and subjacent basalt is relatively constant below 1 μm . The summits of the cinder cones, however, exhibit moderately high reflectivity in channel 8 (1.0 to 1.4 μm) and very high reflectivity in channel 9 (2.0 to 2.6 μm). This type of anomaly was also observed in an area east of Pisgah Crater and southwest of the town of Ludlow (lat 34° 40' N., long 116° 14' W.) and in the Cady Mountains (lat 34° 52' N., long 116° 21' W.), as well as in a number of places shown in the Skylab images of the Nevada test site. In the Skylab S-192 images, anomalies appear in Skylab channel 11 (1.55 to 1.75 μm), but not in images at wavelengths shorter than 1.0 μm (channel 7, 0.78 to 0.88 μm , Fig. 3). In both instances, the anomalies are almost always in volcanic rocks that are reddish, mapped as Tertiary or younger, and at least as mafic as andesite (Ross, 1961; Dibblee, 1966, 1967a, 1967b; Dibblee and Bassett, 1966; Strand, 1967; Cornwall, 1972; Albers and Stewart, 1972); however, most of the andesitic and more mafic rocks in these areas do not show anomalous infrared reflections.

ERIM Channel	Wavelength (μm)
1	0.41 to 0.48
2	0.46 to 0.49
3	0.50 to 0.54
4	0.55 to 0.60
5	0.62 to 0.70
6	0.67 to 0.94
8	1.0 to 1.4
9	2.0 to 2.6

13 channels. Only two have been used in this report.

Skylab Channel	Wavelength (μm)
7	0.78 to 0.88
11	1.55 to 1.75

Both the ERIM test sites and the Skylab Nevada test site contain most of the igneous and sedimentary rock types with the exception of ultramafic. Granite, andesite, basalt, and limestone are par-

DATA REDUCTION

In an attempt to determine the cause of the anomalies, we approximated the spectral reflectivity curves of the anomalies and adjacent materials in the following manner: The reflectivity for typical Mojave Desert materials (soil, playa, basalt) represented in the ERIM images was obtained from the literature (Hovis, 1966); these spectral reflectivity values were assigned to the corresponding units in the image channels and used to

The Skylab scanner was flown in a mode that permitted data collection in

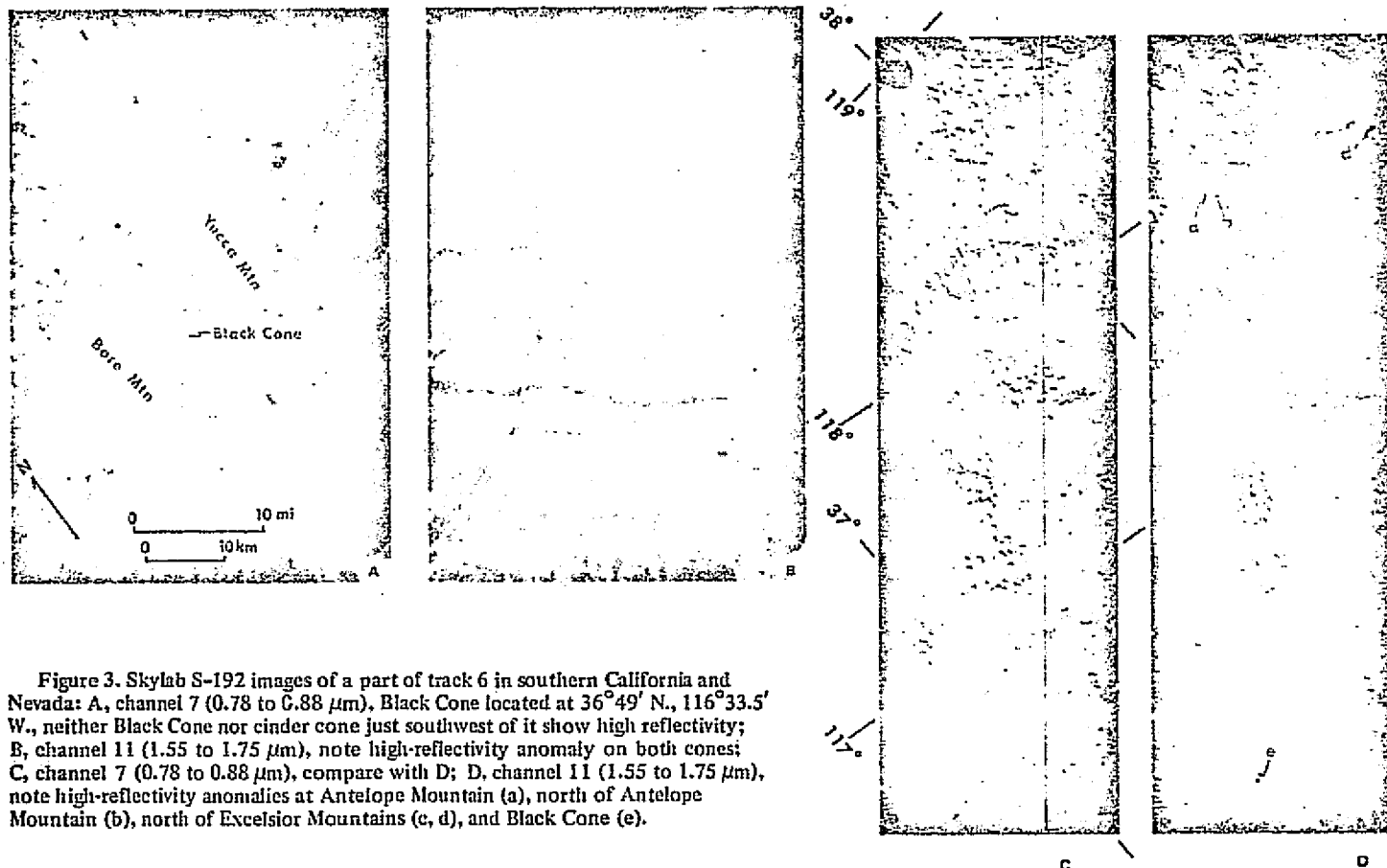


Figure 3. Skylab S-192 images of a part of track 6 in southern California and Nevada: A, channel 7 (0.78 to 0.88 μm), Black Cone located at $36^{\circ}49' \text{ N.}$, $116^{\circ}33.5' \text{ W.}$, neither Black Cone nor cinder cone just southwest of it show high reflectivity; B, channel 11 (1.55 to 1.75 μm), note high-reflectivity anomaly on both cones; C, channel 7 (0.78 to 0.88 μm), compare with D; D, channel 11 (1.55 to 1.75 μm), note high-reflectivity anomalies at Antelope Mountain (a), north of Antelope Mountain (b), north of Excelsior Mountains (c, d), and Black Cone (e).

calibrate the step wedges that accompanied the images. Next, in order to assign spectral reflectivity values to the unknown material, a logarithmic interpolation was made between the known values on the step wedge. Curves were then constructed for several of the anomalies (Fig. 4A). The accuracy of these curves is probably within 10 to 20 percent.

CONCLUSIONS

There is little similarity between the reflectivities derived from the ERIM images (Fig. 4A) and spectral curves for common intermediate and mafic rocks (Hunt and others, 1971; 1973, written commun.). However, inspection of the reflectivity of the oxides (Hunt and others, 1973) hematite, limonite, and goethite shows an increase in reflectivity in the near infrared. Three particle sizes are presented in the spectral data of Hunt and others (1971; Figs. 4B, C, D), but it is only in the smallest size range (0 to 5 μm) that the curves approach the very high reflectivity of the anomalies.

That the mere presence of iron oxides, in any particle size, is not sufficient to produce the anomalies is further demonstrated in the ERIM scanner images of the brick-red Aztec Sandstone in the Spring Mountains (lat $35^{\circ}55' \text{ N.}$, long $115^{\circ}28' \text{ W.}$, Fig. 1A), which showed no high-reflectivity anomalies.

A reasonable geologic explanation for the high-reflectivity anomalies has been proposed by both Ray Wilcox and Richard White of the U.S. Geological Survey (1974, oral commun.). They suggested that the iron oxides (most likely hematite) were produced by late eruptive oxidation of mafic minerals and by precipitation of sublimate during post-eruptive fumarolic steaming. This would account for the high reflectivity, especially in view of the extremely fine particle size (probably $<5 \mu\text{m}$ according to White).

It is also interesting to note that the crater floors of the cones (Fig. 2) typically do not show the anomaly. This is consistent with observations made by Wilcox, who noted that the sublimates are commonly absent in the floors of craters where early cooling, and hence

plugging, of the plumbing systems immediately below the crater floors occurred prior to the post-eruptive steaming.

To date, 107 examples of the anomaly, as described above, have been observed on aircraft and satellite images and correlated with known geology. Of these anomalies, 39 occur in basalt (18 basalt flows, 21 basaltic cinders), 63 in andesite, 2 in alluvium, and one each in intermediate-to-felsic rocks, felsic rocks, and limestone. This last occurrence is mapped as limestone on the geologic reconnaissance map; however, the Skylab S-190-A photographic images show the area to be highly dissected and the anomaly to be reddish brown.

Although these anomalous areas are at present only a geologic curiosity, it is likely that the technique used for discovering them can also be used for rapid discrimination of areas of post-eruptive steaming and sublimation. In addition, investigations are presently under way to see if the intensity of the anomaly can be correlated to the age of the major geologic units.

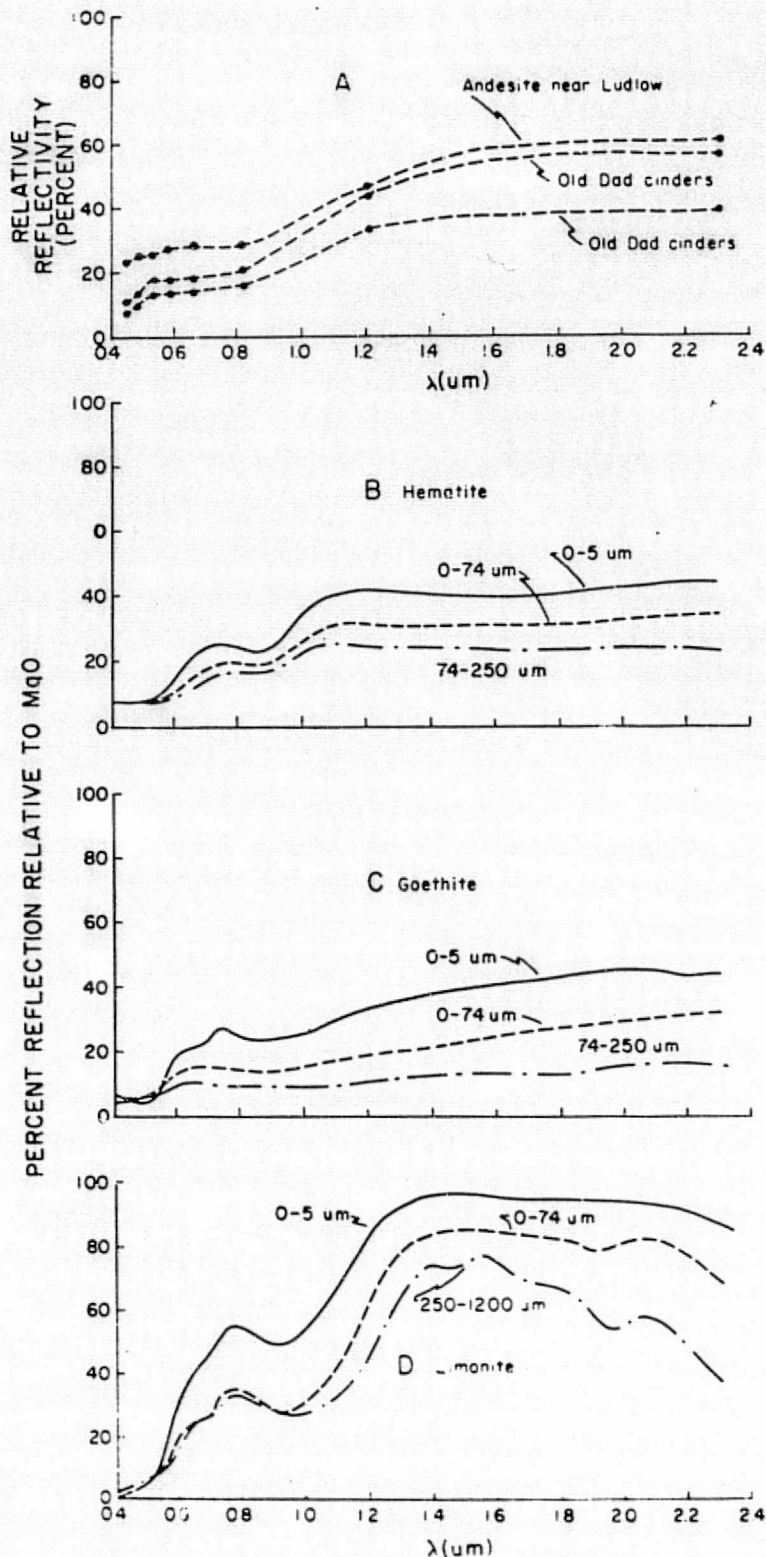


Figure 4. Comparison of (A) spectral reflectivities generated from ERIM scanner and spectral reflectivities of (B) hematite, (C) goethite, and (D) limonite from laboratory data of Hunt and others (1971).

REFERENCES CITED

- Albers, J. P., and Stewart, J. H., 1972, Geology and mineral deposits of Esmeralda County, Nevada: Nevada Bur. Mines and Geology Bull. 78, pl. 1.
- Barca, R. A., 1966, Geologic map and sections of the northern portions of Old Dad Mountain quadrangle, San Bernardino County, California: California Div. Mines and Geology Map Sheet 7.
- Cornwall, H. R., 1972, Geology and mineral deposits of southern Nye County, Nevada: Nevada Bur. Mines and Geology Bull. 77, pl. 1.
- Dibblee, T. W., Jr., 1966, Geologic map of the Lavic quadrangle, San Bernardino County, California: U.S. Geol. Survey Misc. Geol. Inv. Map I-472.
- 1967a, Geologic map of the Ludlow quadrangle, San Bernardino County, California: U.S. Geol. Survey Misc. Geol. Inv. Map I-477.
- 1967b, Geologic map of the Broadwell Lake quadrangle, San Bernardino County, California: U.S. Geol. Survey Misc. Geol. Inv. Map I-478.
- Dibblee, T. W., Jr., and Bassett, A. M., 1966, Geologic map of the Cady Mountains quadrangle, San Bernardino County, California: U.S. Geol. Survey Misc. Geol. Inv. Map I-467.
- Hovis, W. A., Jr., 1966, Optimum wavelength intervals for surface temperature radiometry: *Appl. Optics*, v. 5, no. 5, p. 815-818.
- Hunt, G. R., Salisbury, J. W., and Lenhoff, C. J., 1971, Visible and near-infrared spectra of minerals and rocks—III, Oxides and hydroxides: *Modern Geology*, v. 2, no. 3, p. 195-205.
- 1973, Visible and near-infrared spectra of minerals and rocks—VII, Acidic igneous rocks: *Modern Geology*, v. 4, no. 3, p. 217-224.
- Ross, D. C., 1961, Geology and mineral deposits of Mineral County, Nevada: Nevada Bur. Mines Bull. 58, pl. 11.
- Strand, R. G., 1967, Geologic map of California, Olaf P. Jenkins edition—Mariposa sheet: California Div. Mines and Geology Map Sheet.

ACKNOWLEDGMENTS

Reviewed by Kenneth Watson.
Part of this work was conducted for the National Aeronautics and Space Administration under EREP Inv. No. 487, Kenneth Watson principal investigator.

MANUSCRIPT RECEIVED JUNE 10, 1974

MANUSCRIPT ACCEPTED SEPT. 3, 1974

"Made available under NASA sponsorship in the interest of early and wide dissemination of Earth Resources Survey. Program information and without liability for any use made thereof."

Proc. 10th Intl. Symp. Remote Sensing of Environment, V. 5, 1974.

GEOHERMAL RECONNAISSANCE FROM QUANTITATIVE

ANALYSIS OF THERMAL INFRARED IMAGES

Kenneth Watson

U.S. Geological Survey
Denver, Colorado 80225

ABSTRACT

Remote sensing techniques may be useful in reconnaissance exploration of geothermal systems particularly because of our present limited knowledge of these systems. Although thermal infrared surveys provide a direct measure of surface heating, the variations in surface temperature due to geologic-topographic factors tend to mask the effects of geothermal heating. A thermal model is used to demonstrate that measurements of the mean diurnal temperature together with reflectance measurements and slope information can be used to map the geothermal flux. Theoretical calculations show that the error estimate of the mean diurnal temperature (V_{dc}) falls off rapidly with increasing sample measurements per diurnal cycle (650 HFU at 1 sample/cycle and 75 HFU at 3 sample/cycle).

The thermal model was also used to examine the optimum times in the diurnal cycle in which to obtain an estimate of V_{dc} . A thermal and a reflectance image of the Raft River, Idaho, area, acquired at the optimum time for 1 sample/cycle shows the presence of warm thermal anomalies which do not coincide with changes in the reflectance image. Probe measurements in the vicinity of one of these areas confirm the presence of such an anomaly.

1. INTRODUCTION

Geothermal energy is one of the alternate sources of power currently being evaluated as a supplement to conventional fuels. Because of increasing fuel shortages, it is critical that reconnaissance techniques be developed which will enable us to understand geothermal systems so that we can evaluate their energy potential and develop extraction technology. At present, little is known of this potential and, until recently, exploration techniques were similar to those used in oil exploration during the last century, which relied on location of oil seepage at the surface (Banwell, 1970).

Remote sensing techniques appear to have some promise for reconnaissance use in geothermal exploration. The work conducted in this study is directed at the use of thermal infrared surveys to detect geothermal heat and, in particular, the use of calibrated thermal images, acquired at optimum times during the diurnal cycle, to determine the geothermal detection threshold from thermal infrared surveys.

2. CLASSIFICATION OF GEOHERMAL AREAS

The detection of geothermal anomalies by remote sensing will depend on the recognition of effects due to abnormal heat fluxes at or near the surface. White (1965) classified thermal "systems" into four broad categories: 1) normal systems [1.2 to 1.5 heat flow units (HFU)*; e.g., stable shield areas], 2) higher-than-normal systems [1.5 to 3.0 HFU; e.g., floor of the Gulf of California and its north-

* 1 HFU = 1×10^{-6} cal/cm²/sec

ward extension], 3) composite hydrothermal systems [3.0 to 15 HFU; e.g., floor of the Salton Sea, California, and Larderello, Italy], and 4) hot spring areas [15 to 1500 HFU; e.g., Upper Geyser Basin, Yellowstone National Park, Wyoming; Wairakei, New Zealand; Steamboat Springs, Nevada; The Geysers, California; areas in Ahuachapan, El Salvador; and Reykjavik, Iceland].

Recognizing the importance of separating the solar flux from the geothermal flux, Hase (1971) proposed three classes of geothermal anomalies with intervals based on the absorbed solar flux of 2000 HFU (Sellers, 1967), and his computed value of 240 HFU for the diurnal flux at a depth of one wavelength of the diurnal heating.

A physically more realistic classification of anomalies for thermal surveys would recognize the differences among fluxes detectable by instrument, fluxes detectable on a single thermal image, and fluxes determinable from analyses of several images during a diurnal cycle. A detector thermal resolution of 0.5°C can be equated to a surface flux equivalent to about 50 HFU. The minimum heat flow anomalies (reported in the next section) determined from examination of individual thermal infrared images (generally obtained at night to minimize solar heating effects) have been 100 to 900 HFU's (the lower value is optimistic, as will be shown later in our analysis).

3. PREVIOUS WORK

Remote sensing techniques have been used in geothermal areas both for quantitative measurements of anomalous heat or flux and as a tool for supplementing conventional geologic and geophysical mapping. Those remote sensing techniques which appear applicable to the measurement of heat flow include: 1) direct measurements of heat — thermal infrared imagery and microwave radiometry, and 2) indirect heat measurements, i.e., photography for snowfall calorimetry and mapping thermally stressed vegetation.

Infrared radiometers and scanners have been used to map a wide variety of geothermal features over the last 15 years. A review of the literature for the years 1958-68 by Friedman and Williams (1968) indicates that a preponderance of this work concentrated on volcanic areas. The present paper uses a more limited definition of "geothermal" which excludes active volcanism, because the detection and monitoring of these processes are treated more as hazards than as resources.

One of the earliest direct measurements of surface temperatures in a geothermal area, using thermal IR (infrared), was done in 1961 at Yellowstone National Park by USACRREL (U.S. Army Cold Regions Research and Engineering Laboratory) and the University of Michigan. McLerran and Morgan (1965) reported that geothermal features could be clearly seen, but not identified by type, on the thermal infrared image obtained in this study. Yellowstone National Park was subsequently the site of a variety of geothermal investigations: Miller (1965) used thermal IR in the identification of warm areas and recommended repetitive overflights in order to study dynamic changes in geothermal systems; White and Miller (1969) calculated that 150-500 HFU was the lower limit of the detectable geothermal flux; Hase (1971) determined the detectability limit as 300-900 HFU.

Strangway and Holmer (1966) detected a 600-HFU anomaly in the Lordsburg, N. Mex., area, using instruments capable, according to their estimation, of detecting a temperature difference equivalent to a 15-HFU anomaly. They also noted the importance of certain microclimatological effects which produce anomalies on the radiometer scans; they suggested that microwave observations, being less sensitive to such effects, would provide better data.

In Wairakei area of New Zealand, Hochstein and Dickinson (1970) estimated a detectability limit of 350 HFU for daytime imagery and 150 HFU for nighttime data. The factors which they found affected the images included solar radiation, wind, fog and condensation, and emissivity.

Palmason and others (1970) determined that the thermal infrared scanner was only moderately successful for the detection of anomalous heat flows in geothermal areas in Iceland. Their estimate of 200-700 HFU for the detectability limit closely approximates those determined for Yellowstone National Park and Wairakei. These authors stated that "with a calibrated infrared scanner utilizing a DC restoration

circuit, and a known energy transfer function, by means [sic] of a finer amplitude slicing of the low level anomalies, it may be possible to distinguish better between heretofore undetected low heat flow anomalies and the 'noise' caused by sources other than variations in heat flow to the surface."

Gomez Valle and others (1970) reported that spatial resolution, rather than detectability, limited the thermal resolutions of the infrared images obtained in Michoacan, Mexico. Spatial resolution of 6 m caused the hot pools (with a 1-m average diameter) to merge into their surroundings on the images, therefore lowering the apparent temperatures. Improved scanner resolution and lower aircraft altitudes were suggested as solutions. They also recommended a modification of tape readout levels to drop out all areas below 30°C; such areas would be black on the film image. This modification would allow better discrimination of small changes in temperature above 30°C by "stretching" the temperature levels between 30°C and 100°C over the entire range of film sensitivity. The Michoacan report concluded that thermal infrared studies should be combined with color infrared, electrical resistivity, heat flow, and hydrological and geochemical studies in order to gain a better understanding of geothermal field.

Moxham (1969) reported that the abnormal radiance at The Geysers, California, is restricted to hydrothermal alteration zones and other local features and he found no evidence for a regional anomaly. He concluded that "The aerial IR technique of mapping terrain radiance may find its principal application in preliminary regional assessment of undeveloped geothermal areas." This suggestion proved itself valid in the first small-scale geothermal reconnaissance survey undertaken in unexplored areas of Ethiopia and Kenya by the United Nations Economic and Social Council, Committee on Natural Resources (1971). Flying a scanner with a minimum resolution of 6 m, at altitudes of approximately 3,000 m, the U.N. subcontractor found 105 anomalies of at least 10°C in Ethiopia. Helicopter-borne field investigators found many of the anomalies to be hot springs, fumaroles, and warm fault traces. Similar features were detected in Kenya from a scanner with a 2-m resolution flown by the subcontractor at 915 m.

Indirect methods for determination of anomalous heat flow in geothermal areas include color IR photography, snowfall calorimetry, and vegetation mapping. Color IR photographs were used by Dawson and Dickinson (1970) in New Zealand for mapping heat losses in predominantly conductive parts of geothermal areas. They concluded that their method of contouring heat effects from color differences of vegetation on enlarged color IR images could show 2°C temperature differences at 15-cm depth. They estimated that the accuracy of the method was within 10% of that of a ground survey and took only about 6% of the time.

White (1969) used snowfall calorimetry as a rapid means of determining both conductive and convective heat flow within a factor of two. White mapped the Old Faithful and Sulphur Cauldron areas of Yellowstone National Park using heat flow contours ranging from 450 to 5500 HFU. His method involved mapping of snow-melt lines combined with direct measuring of heat required to melt a known volume of snow along the melt-line contour. Snow must accumulate to a depth of 10 to 15 cm during a 24-hour period for this technique to be practicable.

Vegetation changes near the edges of the geothermal anomaly at Lordsburg, N. Mex., were identified on black and white aerial photographs by Kintzinger (1956). These vegetation changes corresponded to heat flow contours mapped from temperature probe data obtained at 1-m depth. Miller (1968) mapped similar stunted and dying vegetation around a geothermal area in Yellowstone National Park, but concluded that most of the vegetation changes were caused by acid produced in the soil rather than directly by high heat flow. Perhaps both effects are important.

4. THE THERMAL MODEL

Various thermal models have been developed to analyze the surface and near-surface temperature behavior of the ground through a diurnal cycle. In a model developed by Jaeger (1953) for analysis of lunar surface heating a general Laplace transform solution was used which allowed him to treat nonlinear radiative transfer from the surface of a half space. This technique was applied (Watson, 1971; Watson and others, 1971) for interpretation of airborne infrared images, and later extended (Watson, 1973) to the case of periodic heating of a layer over the half space. The Laplace transform solution, however, is time consuming and requires iterative

solutions; in addition, the physical significance of the terms is not clear. Therefore a linearized approximation to the radiative transfer law was introduced, the Fourier series approach was used (Lettau, 1954; Jaeger and Johnson, 1953), and key cases, thus analyzed, were checked using the more precise Laplace transform solution. The numerical agreement was adequate for our purposes.

The model assumptions are those previously introduced (Watson and others, 1971): periodic, one-dimensional, and heat flow with constant thermal properties. The thermal behavior can thus be described using the diffusion equation.

$$\frac{\partial^2 v}{\partial x^2} = \frac{1}{\kappa} \frac{\partial v}{\partial t} \quad (1)$$

surface boundary conditions, at $x=0$

$$-\kappa \frac{\partial v}{\partial x} = \epsilon \sigma (T_{\text{SKY}}^4 - v^4) + (1-A) S_0 f H(t) + Q \quad (2)$$

where

$v(x,t)$ is the ground temperature at distance x below the air-ground interface, at time t measured from local solar noon.

K, κ are, respectively, the thermal conductivity and thermal diffusivity of the ground

ϵ, A are, respectively, the average emissivity and albedo of the ground surface

σ is the Stefan-Boltzmann constant

T_{SKY} is the effective radiant temperature of the sky

S_0 is the solar constant

f is a cloud cover factor to account for daily variations in the insolation

$H(t)$ is the solar incident flux factor at time, t

Q is the geothermal heat flux

A linearized approximation to the radiative transfer term in equation (2) results in

$$T_{\text{SKY}}^4 - v^4 \sim 4T_{\text{SKY}}^3 - 4T_{\text{SKY}}^3 v \quad (3)$$

Now the solar incident flux term is

$$H = M(Z) \cos Z'$$

where $M(Z)$, the atmospheric transmission function, is approximated by

$$M(Z) = 1 - 0.2 \sqrt{\sec Z}$$

Z is the zenith angle

$$\cos Z = \cos \lambda \cos \delta \cos w + \sin \lambda \sin \delta$$

where δ is the solar declination

λ is the latitude of the site

w is the diurnal angular frequency

$$\text{and } \cos Z' = \cos \lambda' \cos \delta \cos(wt)' + \sin \lambda' \sin \delta$$

where Z' is the zenith angle for a nonflat surface

$$\lambda' = \lambda - d \sin \left(\phi - \frac{\pi}{2} \right) = \lambda + d \cos \phi$$

$$(wt)' = wt + d \cos \left(\phi - \frac{\pi}{2} \right) = wt + d \sin \phi$$

d - topographic slope

ϕ - direction of slope

The general method of solution to Eq. 1, subject to the boundary condition Eq. 2 and linearized radiative transfer (Eq. 3) is found in Carslaw and Jaeger (1959, p. 70-71).

We are interested only in the surface temperature:

$$V(0,t) = T_{\text{SKY}} + \frac{Q}{4\epsilon\sigma T_{\text{SKY}}^3} + (1-A)S_0 f \sum_{n=0}^{\infty} C_n \cos nwt + D_n \sin nwt \quad (4)$$

where the harmonic coefficients C_n and D_n are functions of the solar incident flux, H , the sky radiation, T_{SKY} , the emissivity, ϵ , and the thermal property ratio $Kk^{-\frac{1}{2}}$ which is commonly called the thermal inertia. The mean diurnal temperature (V_{dc}) is obtained by integrating the ground temperature over the diurnal cycle, thus

$$V_{dc} = T_{\text{SKY}} + \frac{Q}{4\epsilon\sigma T_{\text{SKY}}^3} + \frac{(1-A)S_0 f}{4\epsilon\sigma T_{\text{SKY}}^3} \int_0^T \frac{H(t)dt}{T}$$

Rearranging the terms yields the geothermal flux

$$Q = (V_{dc} - T_{\text{SKY}}) 4\epsilon\sigma T_{\text{SKY}}^3 - (1-A)S_0 f \int_0^T \frac{H(t)dt}{T} \quad (5)$$

The last term on the right-hand side of equation (5) is a function of the ground albedo and slope and can be directly determined from quantitative reflectance measurements and topographic map data. If the surface bidirectional reflectance can be modeled satisfactorily according to the Lambert law then airborne reflectance measurements acquired at three separate times during the day can be used to compute this term. The three measurements are needed to solve for the unknowns: albedo, slope, and direction of slope.

The T_{SKY} term can be directly determined using a calibrated sky radiometer. Its variations over the site should be negligible under clear sky conditions and a single value should suffice. The remaining unknown term in the equation is the surface emissivity. It may be possible to make thermal measurements in two spectral bands of the 8-14 μm window (Vincent and Thomson, 1972; Vincent and others, 1972) and use a spectral ratio to derive an empirical correction for emissivity variations. In soil-covered areas this spectral contrast will be low and spectral correction may be impossible. Fortunately, in these cases the departure from black-body emission is a second-order effect and an emissivity correction is unnecessary.

5. ESTIMATION OF V_{dc} (MEAN DIURNAL TEMPERATURE)

The mean diurnal temperature (V_{dc}) can be obtained by measuring the average ground temperature with a calibrated thermal scanner from repetitive aircraft

flights throughout the day and night. Theoretical calculations were made of the number of these measurements which are necessary to estimate V_{dc} to various accuracies; the results are shown in figure 1. The temperature difference (ΔV) between this computed average temperature and the true V_{dc} was converted into equivalent heat flow units (ΔQ) from equation (5): $\Delta Q = 4\epsilon\sigma T_{SKY}^4 \Delta V$.

The error bars mark the standard deviation in ΔQ for a 10° slope oriented in the four cardinal directions. The calculations were then repeated but with the sampling times offset from local solar noon by various time lags. The results are plotted in figure 2.

It appears, from the data of figures 2 and 3, that optimum results should be obtainable from three or four samples per diurnal cycle; also, if data are acquired only once in the diurnal cycle then the optimum time is either sunset or shortly after sunrise. Figure 2 illustrates the large heat flux error inherent in data acquired for geothermal analysis in the predawn. Actually, two types of errors are present: 1) an absolute error because the predawn temperature is not a good estimate of the average diurnal temperature, and 2) a relative error because the predawn temperature is still moderately dependent on thermal inertia (the dc temperature is not).

6. INITIAL APPLICATION OF MODEL

Thermal emission and reflectance images of the Raft River, Idaho area were acquired in early November of last year. Much of the area is flat valley alluvium (figure 3), covered with sparse scrub vegetation (figure 4) which on oblique view appears to completely cover the ground (figure 5). Hot wells exist in the area and at one location (figure 6) the hot well water flows out on the ground. There is, however, no altered, steaming ground in the area.

The images (figure 7) were acquired at three different times in the diurnal cycle (08:39, 09:48, and 15:54 MST) using the U.S. Geological Survey dual channel RS-14A scanner in its first operational test. Optical alignment problems, since corrected, prevented a complete evaluation of the model; however, the data are satisfactory for illustration of the major points in the analysis.

Data acquired at 09:48 MST most closely approximate the dc temperature. Comparison of the thermal channel (8-14 μm) data with the reflectance channel (0.5-1.3 μm) data (figure 8) shows the presence of warm thermal anomalies which do not coincide with the reflectance changes. An anomaly is particularly noticeable in the vicinity of the borrow pit where the warm area extends beyond the high reflectivity anomaly. Measurements with l-m probes confirm the anomalous warmth of this area (Paul Williams, oral commun., 1973). The image also defines another warm area near a gravel lens through which warm water rises to the surface. These hypotheses will be examined more intensively using heat flow measurements and repetitive thermal scanner flights.

7. ACKNOWLEDGMENT

I am grateful to Stephen Hart for his assistance in assembling and compiling much of the bibliographic material presented in the section entitled "Previous Work."

8. REFERENCES CITED

- Banwell, C. J., 1970, Geophysical techniques in geothermal exploration (Rapporteur's Report): U. N. Symposium on Development and Utilization of Geothermal Resources, Pisa, Italy, v. 1.
- Carslaw, H. S., and Jaeger, J. C., 1959, Conduction of heat in solids [2d ed.]: Oxford Univ. Press, New York, 510 p.
- Dawson, G. B., and Dickinson, D. J., 1970, Heat flow studies in thermal areas of the North Island of New Zealand: U.N. Symposium on Development and Utilization of Geothermal Resources, Pisa, Italy, v. 2, pt: 1, p. 466-473.

- Friedman, J. D., and Williams, R. S., Jr., 1968, Infrared sensing of active geologic processes: Proc. 5th Internatl. Symposium on Remote Sensing of Environment, Univ. Michigan, p. 787-815.
- Gomez Valle, R. G., Friedman, J. D., Gawarecki, S. J., and Banwell, C. J., 1970, Photogeologic and thermal infrared reconnaissance surveys of the Los Negritos-Ixtland de los Hervores geothermal area, Michoacan, Mexico: U.N. Symposium on Development and Utilization of Geothermal Resources, Pisa, Italy, v. 2, pt. 2, p. 381-398.
- Grose, L. T., 1971, Geothermal energy -- geology, exploration, and developments: Pt. 1, Colo. School of Mines Mineral Industries Bull., v. 14 no. 6.
- Hase, Hirokazu, 1971, Surface heat flow studies for remote sensing of geothermal resources: Proc. 7th Internatl. Symposium on Remote Sensing of Environment, Univ. Michigan, v. 1, p. 237-245.
- Hochstein, M. P., and Dickinson, D. J., 1970, Infrared remote sensing of thermal ground in the Taupo region, New Zealand: U.N. Symposium on Development and Utilization of Geothermal Resources, Pisa, Italy, v. 2, pt. 1, p. 420-423.
- Jaeger, J. C., 1953, Pulsed surface heating of a semi-infinite solid: Quart. Appl. Math., v. 11, p. 132-137.
- Jaeger, J. C., and Johnson, C. H., 1953, Note on diurnal temperature variation: Geofisica Pura E Applicata - Milano, v. 24, p. 104-106.
- Kintzinger, P. R., 1956, Geothermal survey of hot ground near Lordsburg, New Mexico: Science, v. 124, p. 629-630.
- Lettau, Heinz, 1954, Improved models of thermal diffusion in the soil: Geophys. Union Trans., v. 35, no. 1, p. 121-132.
- McLerran, J. H., and Morgan, J. O., 1965, Thermal mapping of Yellowstone National Park: Proc. 3d Internatl. Symposium on Remote Sensing of Environment, Univ. Michigan, p. 517-530.
- Miller, L. D., 1965, Location of anomalously hot earth with infrared imagery in Yellowstone National Park: Proc. 4th Internatl. Symposium on Remote Sensing of Environment, Univ. Michigan, p. 751-769.
- Miller, L. D., 1968, Steaming and warm ground in Yellowstone National Park -- their location, geophysics, vegetation, and mapping with aerial multispectral imagery: Ph.D thesis, Univ. Michigan, 245 p.
- Moxham, R. M., 1969, Aerial infrared surveys at The Geysers geothermal steam field, California, in Geological Survey research 1969: U.S. Geol. Survey Prof. Paper 650-C, p. C106-C122.
- Palmason, G., Friedman, J. D., Williams, R. S., Jr., Jonsson, J., and Saemundsson, K., 1970, Aerial infrared surveys of Reykjanes and Torfajokull thermal areas, Iceland, with a section on the cost of exploration surveys: U.N. Symposium on Development and Utilization of Geothermal Resources, Pisa, Italy, v. 2, pt. 1, p. 399-412.
- Sellers, W. D., 1967, Physical climatology: Univ. Chicago Press, 272 p.
- Strangway, D. W., and Holmer, R. C., 1966, The search for ore deposits using thermal radiation: Geophysics, v. 31, p. 225-242.
- United Nations Economic and Social Council, Committee on Natural Resources, 1971, Recent United Nations experience in the application of remote sensing: United Nations, 6 p.
- Vincent, R. K., and Thomson, Fred, 1972, Spectral compositional imaging of silicate rocks: Jour. Geophys. Research, v. 77, no. 14, p. 2465-2472.

- Vincent, R. K., Thomson, Fred, and Watson, Kenneth, 1972, Recognition of exposed quartz sand and sandstone by two-channel infrared imagery: Jour. Geophys. Research, v. 77, no. 14, p. 2473-2477.
- Watson, Kenneth, 1973, Periodic heating of a layer over a semi-infinite solid: Jour. Geophys. Research, v. 78, no. 26, p. 5904-5910.
- Watson, Kenneth, 1971, A computer program of thermal modeling for interpretation of infrared images: U.S. Geol. Survey Rept. USGS-GD-71-023; available from Dept. Commerce, National Technical Information Service, Springfield, Va. (NTIS No. PB-203-578).
- Watson, Kenneth, Rowan, L. C., and Offield, T. W., 1971, Application of thermal modeling in the geologic interpretation of IR images: Proc. 7th Internatl. Symposium on Remote Sensing of Environment, Univ. Michigan, v. 3. p. 2017-2041.
- White, D. E., 1965, Geothermal energy: U.S. Geol. Survey Circ. 519, 17 p.
- White, D. E., 1969, Rapid heat-flow surveying of geothermal areas utilizing individual snowfalls as calorimeters: Jour. Geophys. Research, v. 74, p. 5191-5201.
- White, D. E., and Miller, L. D., 1969, Calibration of geothermal infrared anomalies of low intensity in terms of heat flow. Yellowstone National Park (abs.): EOS (Am. Geophys. Union Trans.), v. 50, p. 348.

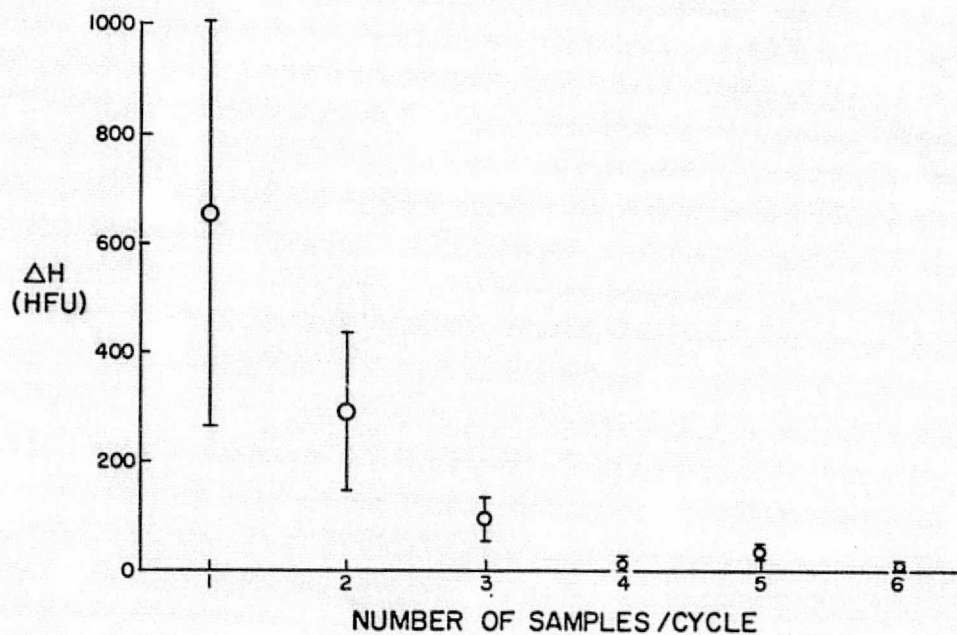


Figure 1. - Equivalent heat flux error, ΔH versus the number of samples per diurnal cycle. The mean values (o) and the standard deviation (bars) were computed for a series of time lags from local noon. Values were computed for the circumstances of the Raft River: latitude 42° , solar declination -15° .

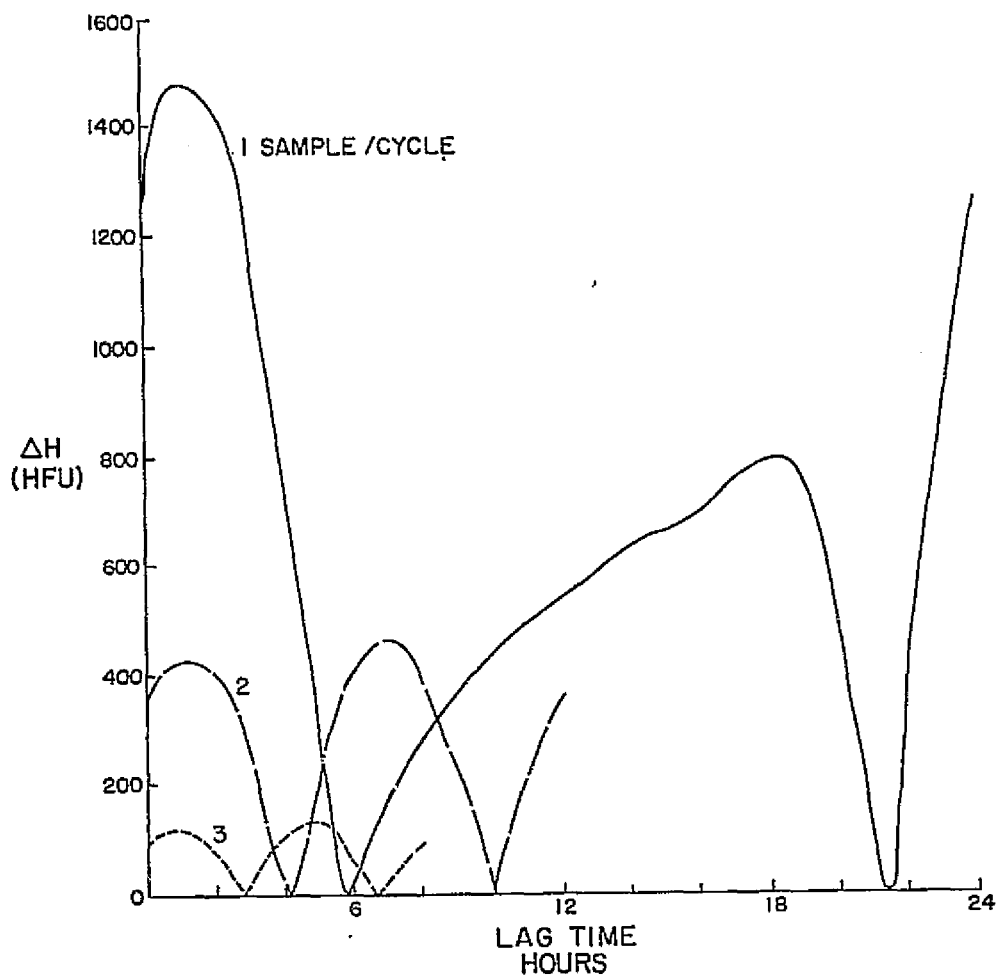


Figure 2. - Equivalent heat flux error, ΔH versus the time lag for one, two, and three samples per diurnal cycle. The mean and standard deviation values for these curves are displayed in figure 1. Optimum times to acquire thermal scanner data are when ΔH is a minimum.

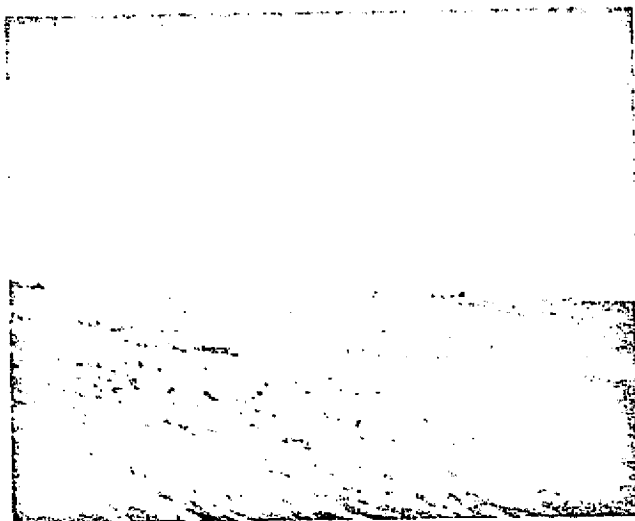


Figure 3. - Raft River area; view looking west.

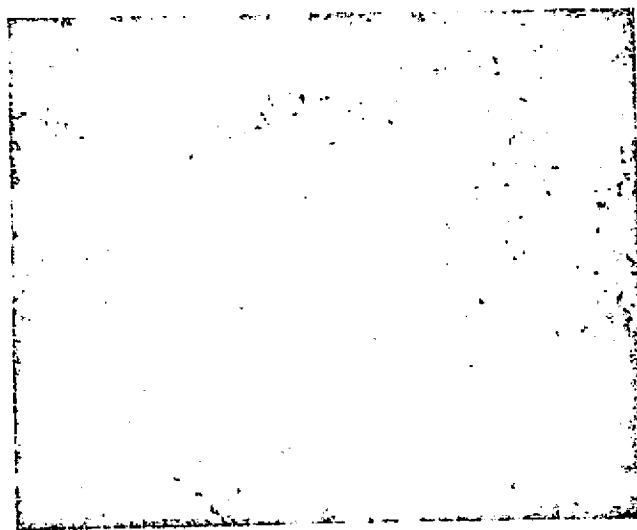


Figure 4. - Vertical view of ground showing scrub vegetation and valley alluvium.



Figure 5. - Oblique view showing vegetation.



Figure 6. - View of hot water overflowing from well.



a



b



c

Figure 7. - Thermal images of the Raft River area at a) 08:39, b) 09:48, and c) 15:54 MST. Local sunrise occurred at 07:00.

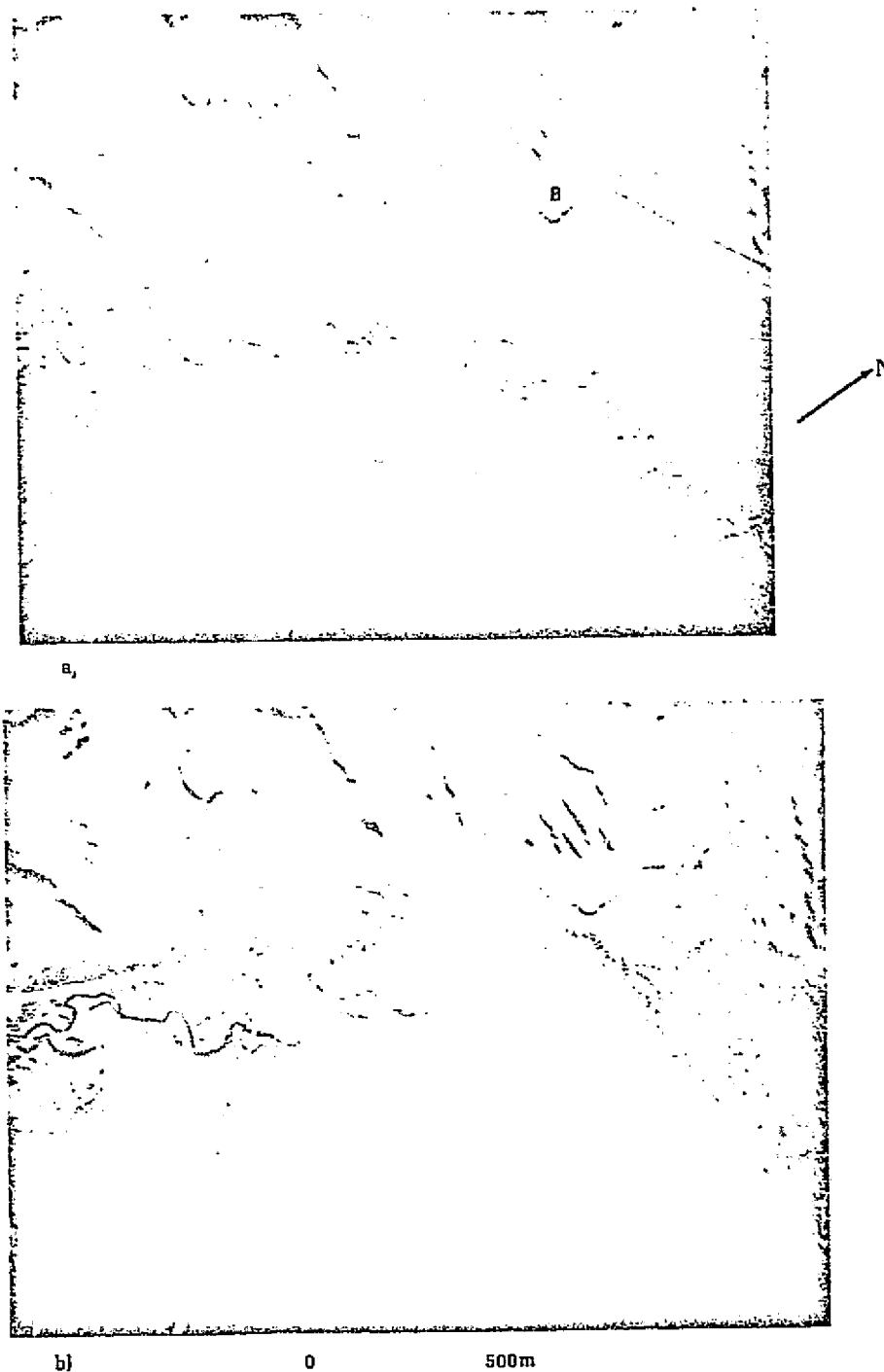


Figure 8. - Thermal (a) and reflectance (b) images of the Raft River at 09:48 MST, corresponding to one of the optimum times for geothermal mapping (see figure 2) for one sample per cycle. The borrow pit (B) is an area of both high reflectivity and high temperature, indicating a region of anomalous reflectance and thermal inertia. The westward extension of the thermal anomaly beyond the anomalous reflectance region is consistent with increased geothermal heating.

"Made available under NASA sponsorship
in the interest of early and wide dis-
semination of Earth Resources Survey
Program information and without liability
for any use made thereof."

ORIGINAL PAGE IS
OF POOR QUALITY

NASA Scientific and Technical Information Facility

Geologic Applications of Thermal Infrared Images

KENNETH WATSON

Invited Paper

Abstract—Thermal infrared images provide information about the near-surface physical state of geologic materials, particularly, the density, water content, and heat transfer. Nonterrestrial planetary studies, conducted at fairly coarse resolution, have been useful primarily in determining the distribution of rock fragments. Terrestrial studies, conducted from satellite and aircraft at coarse to fine resolutions, have been successful for monitoring effusive volcanism, delineating areas of steaming altered ground and hot-spring activity, detecting fractures expressed hydrologically and topographically, and distinguishing a variety of geologic materials with physical and compositional differences.

Interpretation of thermal images is complicated by the various types of physical processes involved and commonly requires an assessment of many different factors. A simple theoretical model was used in this analysis to provide quantitative assessment of some of these factors, to predict optimum times to acquire thermal data, and to determine quantitative values of various properties of terrain.

Two geologic applications were studied in some detail: geothermal mapping and thermal inertia mapping. Initial results indicate that both techniques have considerable potential, especially in reconnaissance studies. These data were acquired under optimal meteorological conditions and at sites where the geologic materials were well exposed. A realistic assessment of the limitations of these techniques must await future studies.

INTRODUCTION

OPTICAL-MECHANICAL scanners provide the means to monitor the temporal and spatial variations in the natural thermal emission from planetary surfaces. These variations, observed at a great variety of altitudes from low-

flying aircraft to orbiting satellites, can be used to deduce physical properties of terrain materials and thus to infer geologic processes which have occurred. The interpretation of these data can range from direct visual examination of photographic recordings of the measured signal (using techniques developed in photogeology) to sophisticated digital processing using modeling analysis and pattern recognition techniques. These investigations are limited, however, by the complexity of the problem, in terms of both the physical phenomena and the number of different factors that influence the result. Of necessity, the interpretation of thermal infrared data has been based on quite simple theoretical models, involving very limiting assumptions and fairly ideal circumstances (both meteorologically and geologically). Future refinements in observational technique and theoretical analysis will be required in order to apply the technique routinely to the diverse terrain conditions found in nature.

This paper describes the development of one theoretical model for analysis of the surface temperature distribution. The results provide a quantitative estimate of the effects of various geologic, meteorologic, and topographic factors and hence can be used as a basis for direct interpretation of the thermal images. In addition, the model curves can be used to predict optimum times to acquire the data in order to enhance specific effects and features. Finally, the model can be used to determine quantitative values of various properties of the terrain. This last aspect of the model has greatest impact in future geologic applications and receives the most attention in this paper.

Manuscript received August 13, 1974; revised August 27, 1974.

The author is with the U.S. Geological Survey, U.S. Department of the Interior, Denver, Colo. 80225.

A mathematical model of the near-surface conductive heat transfer was used to develop a means to interpret thermal infrared images in terms of the relevant physical properties and processes. For simplicity, I assumed one-dimensional periodic heating of a uniform half-space (a region bounded by a plane on its upper side and extending downward to infinity) of constant thermal properties. The temperature obeys the diffusion equation:

$$\kappa \frac{\partial^2 v}{\partial x^2} = \frac{\partial v}{\partial t} \quad (1)$$

where $v = v(x, t)$ is the temperature at distance x below the surface and time t , from local solar noon, and κ is the thermal diffusivity of the half-space. The solution to (1) for periodic heating of angular frequency ω is [4, p. 81]

$$v(x, t) = \sum_{n=0}^{\infty} D_n \exp(-k\sqrt{n}x) \cos(n\omega t - \xi_n - k\sqrt{n}x) \quad (2)$$

where D_n and ξ_n are arbitrary coefficients and $k \equiv \sqrt{\omega/2\kappa}$ is the wavenumber of the first harmonic. The arbitrary coefficients are evaluated by expressing the surface boundary condition as an energy balance between incoming solar and sky radiation, outgoing ground radiation, and conduction into the ground. For the moment, I shall ignore other heat transfer mechanisms (atmospheric conduction and convection, convective heat transfer in the ground, and latent heat effects due to evaporation or condensation of water).

Thus at $x = 0$

$$-K \frac{\partial v(0, t)}{\partial x} = -\epsilon \sigma v^4 + I \quad (3)$$

where I is the absorbed incoming radiation composed of both the short-wavelength solar flux (less than $4 \mu\text{m}$) and the long-wavelength atmospheric flux (greater than $4 \mu\text{m}$), ϵ is the mean emissivity of the surface, σ is the Stefan-Boltzmann constant, and K is the thermal conductivity of the half-space.

The quadratic temperature term precludes direct substitution of (2) in (3). Jaeger [15] used Laplace transforms to develop a relation between the surface flux and the surface temperature, and solved for surface temperature by iteration.

$$f_n = \frac{P}{\sqrt{\pi\tau}} \sum_{s=1}^m v_s \phi_{n-s+1}, \quad n = 1, 2, \dots, m \quad (4)$$

where f_n is the average flux into the ground in the n th interval, P is the thermal inertia of the ground ($P = K/\sqrt{\kappa}$), τ is the period of the heating flux, v_s is the average surface temperature in the s th interval, and the ϕ 's are a set of numerical coefficients determined solely by m , the total number of intervals in τ . The term f_n which is equal to the right-hand side of (3) contains a v_s^4 term thus requiring an iterative solution for v_s . This approach has been used both to analyze planetary data [16] and to interpret aircraft thermal images [44], [45]. The technique has been extended to the case of a layer over the half-space [43] in order to examine the effects of surface coatings and lichen cover.

A second approach to the nonlinear transfer problem is the method of finite differences [46]. Care must be taken in selecting the spatial and time increments to ensure that convergence is achieved. Both the finite difference and the

Laplace transform technique obscure the physical significance of the terms and can be computationally time-consuming. It was decided to linearize the radiative flux term in the boundary condition and then check the numerical results with the more exact Laplace transform solution. The comparison was satisfactory for terrestrial diurnal temperature ranges. The linearized solution [9] is too inaccurate for the temperature variations encountered on the lunar surface [16].

The incoming radiation term I is composed of the short-wavelength radiation from the sun I_s (modulated by the atmospheric transmission) and the long-wavelength radiation from the sky. This latter term can be approximated by an expression σT_{sky}^4 where T_{sky} is an effective sky radiance temperature; hence the absorbed flux is $\epsilon \sigma T_{\text{sky}}^4$. The long-wavelength terms of the right-hand side of (3) can then be linearized as

$$\epsilon \sigma v^4 - \epsilon \sigma T_{\text{sky}}^4 \sim 4\epsilon \sigma T_{\text{sky}}^3 (v - T_{\text{sky}}), \quad \text{for } \frac{v - T_{\text{sky}}}{T_{\text{sky}}} \ll 1. \quad (5)$$

The solution of the diffusion equation (1) subject to the boundary condition (3) modified by (5) can be obtained by a simple substitution [4, p. 70]; let

$$\phi(x, t) = v - \frac{1}{h} \frac{\partial v}{\partial x} \quad (6)$$

where

$$h = 4\epsilon \sigma T_{\text{sky}}^3 / K.$$

Then

$$\kappa \frac{\partial^2 \phi}{\partial x^2} = \frac{\partial \phi}{\partial t} \quad (7)$$

subject to the boundary condition at $x = 0$

$$\phi = T_{\text{sky}} + I_s / Kh \quad (8)$$

where I_s is the short-wavelength absorbed flux. This term is a function of the ground albedo A , the solar declination δ , the site latitude λ , and the local slope and can be expressed as follows:

$$I_s = (1 - A) S_0 CM(Z) \cos Z' \quad (9)$$

where S_0 is the solar constant, C is a factor to account for the reduction in solar flux due to cloud cover, $M(Z)$ is the atmospheric transmission as a function of the zenith angle Z , and Z' is the local zenith angle for an inclined surface.

The atmospheric attenuation can be approximated by a square root of zenith angle law [1]; let

$$M(Z) = 1 - 0.2 \sqrt{\sec Z} \quad (10)$$

where

$$\cos Z = \cos \lambda \cos \delta \cos \omega t + \sin \lambda \sin \delta. \quad (11)$$

The local zenith angle Z' can be computed from

$$\begin{aligned} \cos Z' = & \cos d \cos Z - \sin d \{ \sin \phi \cos \delta \sin \omega t \\ & - \cos \phi \sin \delta \cos \lambda - \sin \delta \sin \lambda \cos \omega t \} \end{aligned} \quad (12)$$

where d is the surface slope angle measured downward from the horizontal, and ϕ is the azimuth of the slope angle measured counterclockwise from north. For convenience, I shall define an additional parameter $H(t)$ which is the local

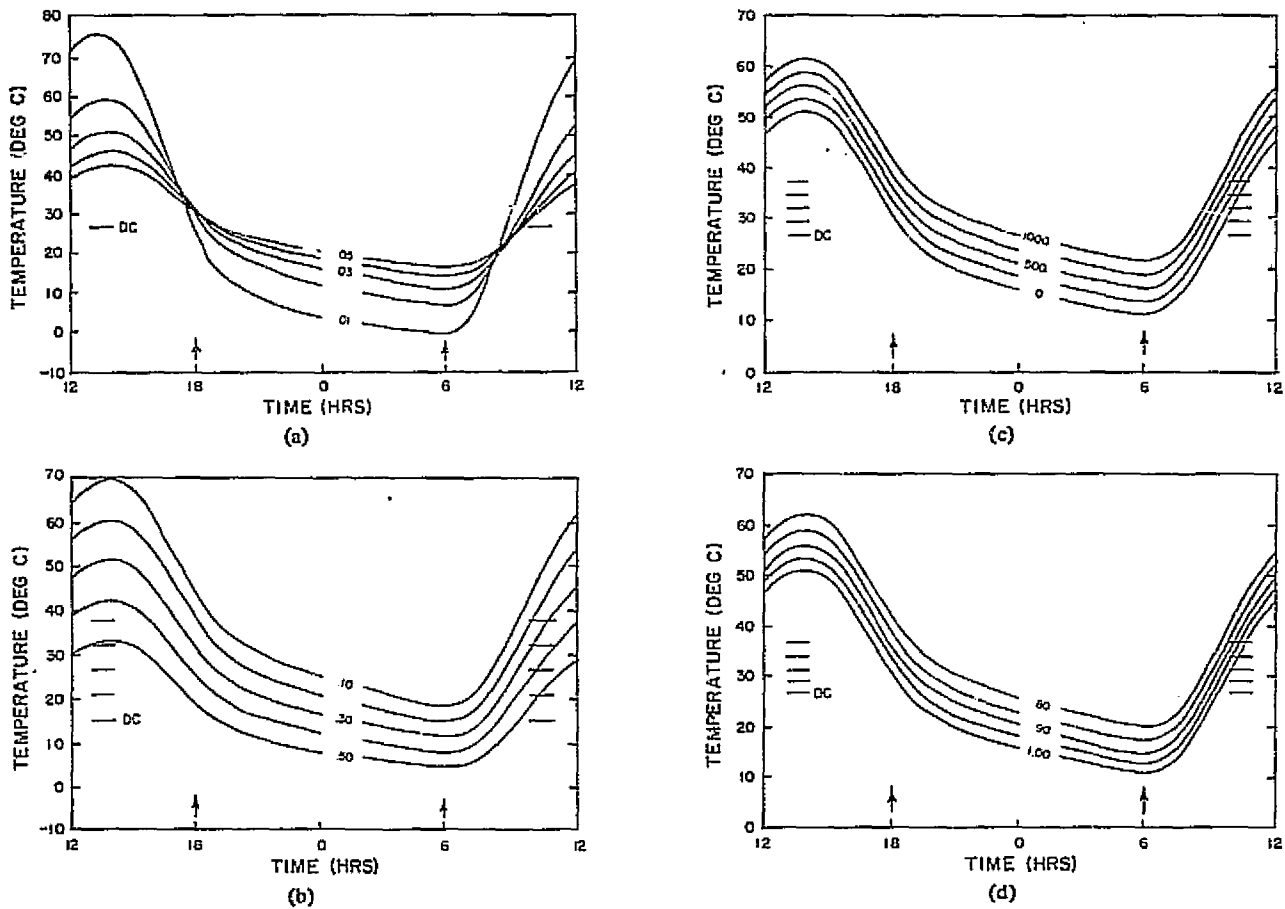


Fig. 1. Diurnal temperature curves for varying (a) thermal inertia (in $\text{cal/cm}^2/\text{s}^{1/2}$), (b) albedo (in fractions <1), (c) geothermal heat flux (in HFU), and (d) emissivity (in fractions <1). Times are local solar values. The mean diurnal temperature DC is indicated by a horizontal line for each curve. Note that this value is constant for varying thermal inertia [see 1(a)] and that the amplitude of each curve is reasonably independent of geothermal flux [see 1(c)] and emissivity [see 1(d)]. The vertical arrows near the time axis mark the sunset and sunrise times. Fixed parameter values used in the computation of these curves are: inertia $0.03 \text{ cal/cm}^2/\text{s}^{1/2}$, albedo 0.3 , emissivity 1.0 , latitude 30° , solar declination 0° , sky radiant temperature 260° , dip 0° , cloud cover 0.2 .

insolation:

$$H = \begin{cases} M(Z) \cos Z', & -t_R < t < t_S \\ 0, & t_S < t < t_R \end{cases}$$

where t_S and t_R are the local sunset and sunrise times (measured from local solar noon), and are chosen so that for $-t_R > t > t_S$, $\cos Z > 0$, and $\cos Z' > 0$.

Hence

$$I_s = (1 - A) S_0 CH \quad (13)$$

and the boundary condition at $x = 0$ (8) becomes

$$\phi = T_{\text{sky}} + (1 - A) S_0 CH / Kh. \quad (14)$$

The solution to (7) subject to (14) is

$$\phi(x, t) = T_{\text{sky}} + \frac{(1 - A) S_0 C}{Kh} \sum_{n=0}^{\infty} A_n \exp(-k\sqrt{n}x) \cos(n\omega t - \epsilon_n - k\sqrt{n}x) \quad (15)$$

where A_n and ϵ_n are the amplitude and phase of the harmonic components of the local insolation H .

The surface temperature can then be determined from equation (6) by integration [4, p. 70]

$$u(0, t) = h \int_0^{\infty} \phi(\eta, t) \exp(-h\eta) d\eta \\ = T_{\text{sky}} + \frac{(1 - A) S_0 C}{K} \sum_{n=0}^{\infty} \frac{A_n \cos(n\omega t - \epsilon_n - \delta_n)}{\sqrt{(h + k\sqrt{n})^2 + (k\sqrt{n})^2}} \quad (16)$$

where $\delta_n = \tan^{-1}(k\sqrt{n}/h + (k\sqrt{n}))$.

The effect of a geothermal heat flux Q can now be introduced by adding a second solution $v = Qx/K + Q/Kh$ which satisfies the boundary condition (3) and the differential equation (1).

Recall that

$$k = \sqrt{\omega/2K}$$

$$h = 4\epsilon\sigma T_{\text{sky}}/K.$$

Introduce $r = P\sqrt{n}/\tau$, where $\tau = 2\pi/\omega$ and $s = hK$, then $k\sqrt{n}/h = r\sqrt{n}/s$ and

$$\sqrt{kn + h^2} = h\sqrt{(r\sqrt{n}/s)^2 + 1}.$$

Hence

$$v(0, t) = T_{\text{sky}} + Q/s + (1 - A)S_0C$$

$$\sum_{n=0}^{\infty} A_n \frac{\cos(n\omega t - \epsilon_n - \delta_n)}{\sqrt{(s + r\sqrt{n})^2 + (r\sqrt{n})^2}} \quad (17)$$

where

$$\delta_n = \tan^{-1}(r\sqrt{n}/s + r\sqrt{n})$$

$$r = P\sqrt{\pi/\tau}$$

$$s = 4\epsilon\sigma T_{\text{sky}}^3.$$

Fig. 1 illustrates the diurnal temperature behavior exhibited for variations in four important geologic parameters: thermal inertia, albedo, geothermal flux, and emissivity.

The mean diurnal temperature v_{dc} is computed by integrating (17) over the diurnal cycle

$$v_{dc} = \frac{1}{\tau} \int_0^{\tau} v(0, t) dt = T_{\text{sky}} + \frac{Q}{s} + (1 - A)S_0CA_0 \cos \epsilon_0/s \quad (18)$$

where $A_0 \cos \epsilon_0 = (1/\tau) \int_0^{\tau} H(t) dt$.

It is important to note that v_{dc} is independent of the thermal inertia of the ground and can be used in conjunction with albedo measurements and topographic information to derive the geothermal flux Q .

The day-night temperature difference (Δv) is computed by forming the difference between the noon and midnight temperatures.

$$\Delta v = v(0, 0) - v(0, \tau/2)$$

$$= 2(1 - A)S_0C \sum_{m=1}^{\infty} \frac{A_{2m-1} \cos(\epsilon_{2m-1} + \delta_{2m-1})}{\sqrt{(s + r\sqrt{2m-1})^2 + (r\sqrt{2m-1})^2}} \quad (19)$$

The quantity $\Delta v/(1 - A)$ which is a function of the thermal inertia P (through dependence on r) can be determined observationally and thus used to map thermal inertia variations.

GEOHERMAL MAPPING

Thermal images display the spatial surface temperature variations of the ground and thus thermal infrared mapping is an obvious technique to consider for reconnaissance exploration of geothermal areas. Success has been achieved in monitoring worldwide areas of effusive volcanism (for example, in Hawaii [10], Iceland [25], and Italy [5]) and in delineating areas of steaming altered ground and hot-spring activity in the western United States (for example, Yellowstone National Park [19], [20], The Geysers, Calif. [21]). Considerable reservations remain, however, about the general application of thermal mapping to the detection of lower level geothermal anomalies principally because of the noise effect of geologic-hydrologic-topographic variations [2]. Estimates which have been made of the minimum detectable geothermal flux are based largely on the assumption that predawn measurements are optimum, because they minimize the effects of solar heating: Hochstein and Dickinson [13], 150-350 HFU; White and Miller [47], 150-500 HFU; Hase [12],

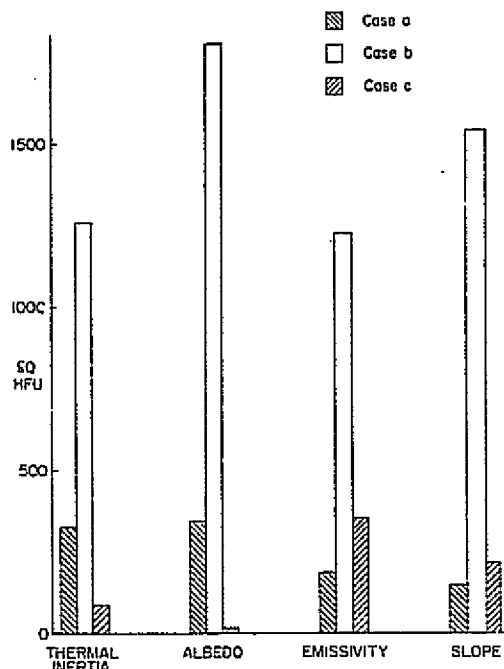


Fig. 2. Equivalent heat flux error δQ computed from temperature difference values between standard and comparative values for different geologic-topographic properties: thermal inertia P , albedo A , emissivity ϵ , and slope d . The assumed standard values are $P = 0.03 \text{ cal/cm}^2\text{s}^{1/2}$, $A = 0.3$, $\epsilon = 1.0$, and $d = 0^\circ$ and comparative values are $P = 0.04$, $A = 0.2$, $\epsilon = 0.95$, and $d = 10^\circ$. Case *a* is computed from differences in the predawn values and is a measure of the "noise" present on predawn images which are used to make relative estimates of the geothermal flux. Case *b* is computed from differences between predawn comparative and mean diurnal DC standard values and is a measure of the absolute error in predawn measurements. Case *c* is computed as in case *b* but using midmorning (10 A.M.) comparative values. Case *c* illustrates the significant reduction in the "noise" effects that can be achieved by correct selection of data acquisition times.

>240 HFU (theoretical) and 900 HFU (measured); and Palmason *et al.* [25], 200-700 HFU. It is instructive to compare these values with quantitative estimates of the effects of various geologic-topographic factors. The comparison is made more meaningful by converting temperature differences into equivalent heat fluxes, and this is done by a theoretical computation of the temperature change which occurs for variations in the geothermal flux. The results (Fig. 2) illustrate that natural variations in geologic properties or topography can easily overwhelm internal heat fluxes of several hundred HFU in all but the flattest and most homogeneous terrains.

The next step is to see whether some analysis scheme can be developed which will reduce the effect of some of these factors. In the section on the thermal model (18), I demonstrated a relationship between the mean diurnal temperature v_{dc} and the internal heat flux (Q). v_{dc} is independent of the thermal inertia of the ground and the equation provides a formulation to correct quantitatively for variations in albedo and slope. To compute Q there remains the problem of determining v_{dc} , albedo, and emissivity by remote measurement. A computation of v_{dc} can be made by measuring the ground temperature at several times in the diurnal cycle. The number of times required can be evaluated by comparing the mean of several measurements with v_{dc} and converting this temperature difference into the equivalent heat flux.

¹ 1 HFU = $1 \times 10^{-6} \text{ cal/cm}^2\text{s}$.

Let

$$\delta v(m) \equiv \frac{1}{m} \sum_{k=1}^m v(0, t_k) - v_{dc}$$

The calculation of δv can be further refined by the introduction of a variable lag (θ) measured from local noon.

Let $t_k = \theta + (k-1)\tau/m$, where $\theta < \tau/m$. Therefore,

$$\delta v(m, \theta) = (1-A)S_0C \sum_{p=0}^{\infty} A_{pm} \frac{\cos(pm\omega\theta - \epsilon_{pm} - \delta_{pm})}{\sqrt{(s+r\sqrt{pm})^2 + (r\sqrt{pm})^2}} \quad (20)$$

Now from (17) it is possible to convert δv into an equivalent heat flux (δQ), i.e., $\delta Q = s\delta v$. The results, plotted in Fig. 3, show that the estimate of v_{dc} can be significantly improved by increasing the number of samples to 3 or 4 samples per cycle. The gain achieved by further increase to 5 or 6 samples per cycle is largely illusory, because measurement errors and calibration problems will most certainly exceed the gain.

The ground albedo can be determined by combining reflectance measurements with topographic map information, provided that we have an adequate model of the bidirectional reflectance. For simplicity, we can assume that bare and sparsely vegetated soils can be approximated as Lambert reflectors [8]. In that case, reflectance measurements at three times in the diurnal cycle can be used to correct for albedo and slope.

Let the measured reflectivity at time t_j be r_j . Then

$$r_j = A \cos Z'_j, \quad j = 1, 2, 3$$

where $\cos Z'_j$ is defined as in (12). Then

$$A = r_2 / \cos Z'_2$$

where

$$d = -\tan^{-1} \{ (x_1 \cos \lambda \cos \delta + Z_1 \sin \delta \sin \delta) / (x_1 \sin \lambda \sin \delta - y_1 \sin \phi \cos \delta + Z_1 \cos \phi \sin \delta \cos \lambda) \}$$

$$\phi = \pi + \tan^{-1} \{ DF - E\sqrt{D^2 + E^2 - F^2} / EF + D\sqrt{D^2 + E^2 - F^2} \}$$

and

$$D = \cos \delta \{ (x_3 y_1 - x_1 y_3) \cos \lambda \cos \delta + (y_1 Z_3 - y_3 Z_1) \sin \lambda \sin \delta \}$$

$$E = \sin \delta \cos \delta \cos^2 \lambda (x_1 Z_3 - x_3 Z_1)$$

$$F = -\sin^2 \delta \sin^2 \delta (x_1 Z_3 - x_3 Z_1)$$

$$x_i = r'_i \cos \omega t_2 - \cos \omega t_i$$

$$y_i = r'_i \sin \omega t_2 - \sin \omega t_i$$

$$Z_i = r'_i - 1$$

$$r'_i = r_i / r_2, \quad i = 1, 3.$$

The remaining unknown in the geothermal equation (18) is the emissivity of the surface. Actually, emissivity variations enter the problem in two ways: emitted radiation and kinetic temperature. The thermal scanner measures the effective radiative temperature of ground and this can be approximated by $\epsilon^{1/4} v$, where v is the ground kinetic temperature, and ϵ is the surface emissivity.

But the ground kinetic temperature and hence its mean v_{dc} are also functions of emissivity. Because the kinetic temperature decreases with increasing emissivity while the radiative temperature increases, the two effects work against each other and reduce the net effect of emissivity variations.

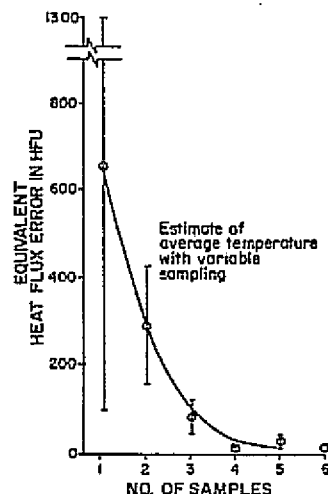


Fig. 3. The equivalent heat flux error (in HFU) versus number of samples/diurnal cycle. The mean and standard deviations are computed over variable time lags (computed from local noon).

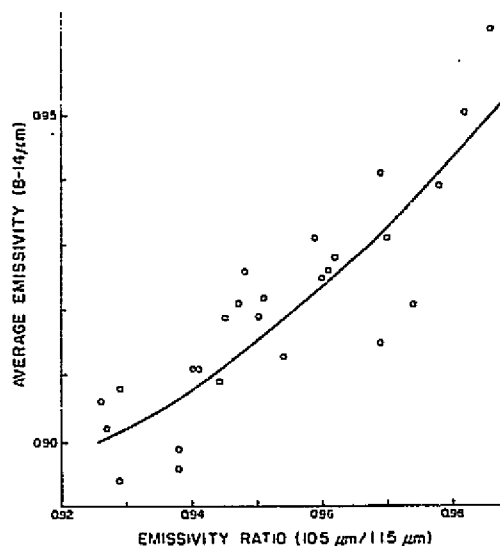


Fig. 4. The average emissivity (8-14 μ m) versus the emissivity ratio (computed over 1- μ m bandwidths centered at 10.5 μ m and 11.5 μ m) for various igneous rocks whose spectral reflectance was measured in the laboratory [40]. The line is the computed quadratic least squares fit to the data; the standard deviation of this fit is 0.01 or approximately 1 percent of the average emissivity.

For most soils, the effect of fine grain size is to reduce the spectral contrast and raise the emissivity in the 8-14- μ m region [36], producing a fairly constant value of 0.95. The most significant departure from this value occurs for silicate-rich soils or rocks, owing to the reststrahlen features near 10 μ m [7], [14], [18]. In these cases it may be possible to correct for emissivity variations by measuring the spectral emission ratio in two adjacent spectral bands. Spectral band ratios have been previously applied to enhance the spectral contrast of rocks and soils [37]-[39]. Using published laboratory reflectance data of natural surfaces [40], I have computed the average 8-14- μ m emissivity and the emissivity ratio in two adjacent bands. A quadratic least squares fit to these data (Fig. 4) shows that by this ratio the net emissivity can be estimated to an accuracy of 1 percent. Further examination of natural surfaces on a scale comparable to aircraft

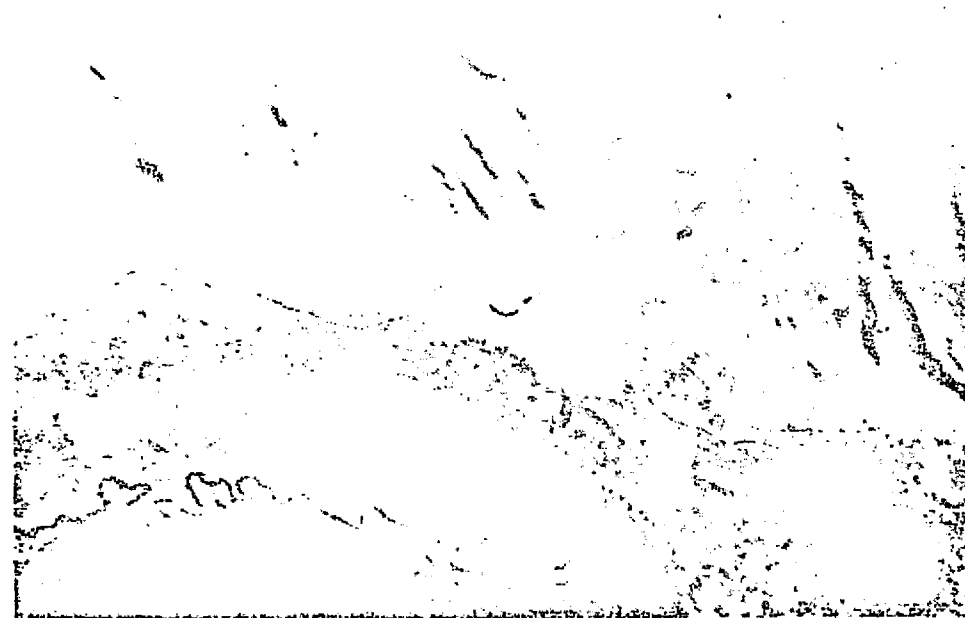
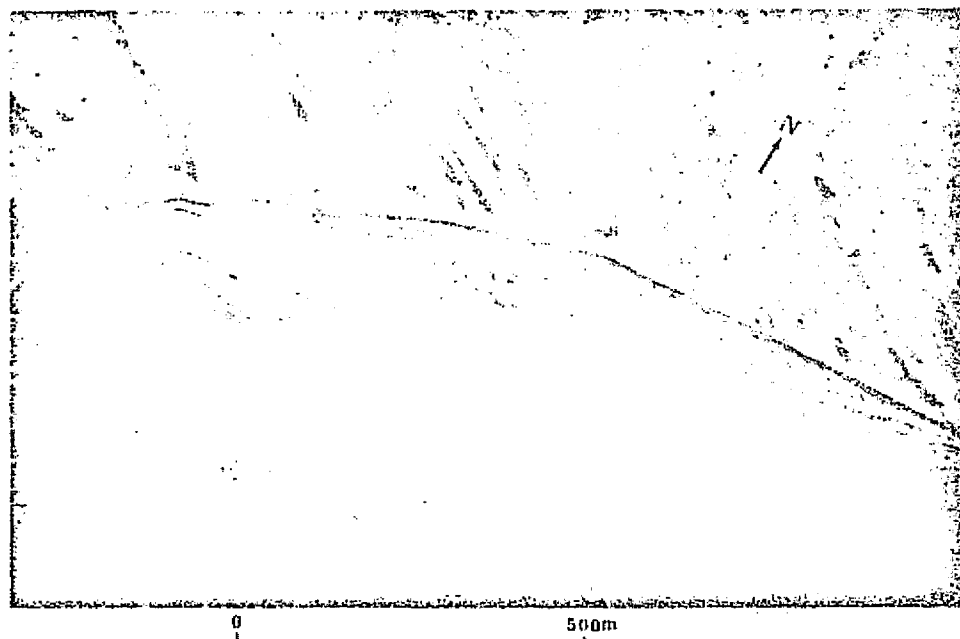


Fig. 5. Thermal (8-14 μm [upper]) and reflectance (0.3-1.2 μm [lower]) image pair for the Raft River, Ida., area. The image acquisition time (09:48) corresponds to an optimum time to estimate the DC temperature. Note the warm area in the vicinity of a borrow pit (just above center of upper image). It coincides, in part, with a high-reflectance anomaly [lower image] but extends beyond it.

scanner resolution of several meters will be necessary to evaluate the practicality of this approach.

An initial test of our technique to use v_{dc} for mapping geothermal heat flux was performed at Raft River, Idaho [42]. A thermal image, acquired at the optimum time for one sample per cycle, is shown in conjunction with the reflectance image obtained at the same time (Fig. 5).

An interesting thermal anomaly is present in the vicinity of a borrow pit. Part of the warm ground corresponds with a high-reflectance anomaly associated with vegetation differences. The remaining anomaly lies outside this area and is not due to reflectance or slope effects. Because the data were acquired at an optimum time for geothermal mapping,

the ground temperature is not strongly dependent on thermal inertia differences. It seems reasonable to attribute the entire anomaly to geothermal heating. This conclusion is consistent with probe measurements at the site.

It is tempting but still premature to speculate on the minimum detectable heat flux that can be achieved with this technique. The model results suggest that v_{dc} can be estimated by repeated scanner overflights to an accuracy of a few tens of HFU. Conventional thermal scanners can collect calibrated high-resolution images with an NETD (noise equivalent temperature difference) of 0.1°C which translates to less than 10 HFU. But this must be tempered by a comparison with other energy sources which have been neglected in our

analysis. For example, although we define the incident solar flux as short-wavelength radiation (occurring below $4\ \mu\text{m}$), about 1 percent of the solar flux occurs beyond $4\ \mu\text{m}$ and this amounts to about 300 HFU. Under stable atmospheric conditions, radiation is the dominant heat transfer mechanism from the surface. At 300 K this flux is approximately 10 000 HFU. Convective heat transfer, under moderately windy conditions, can equal this, and thus even under stable conditions, subtle microclimatic and surface roughness variations could produce heat flux errors of many tens of HFU. Then, too, errors in estimating the surface albedo, atmospheric transmission, and scattered sky radiation are significant because these factors modulate the solar flux. A realistic estimate will have to await more observational tests and a detailed comparison with near-surface probe data of the geothermal flux.

THERMAL INERTIA MAPPING

Previous investigators recognized the utility of thermal infrared surveys to discriminate geologic materials based on differences in their thermal properties. The earliest geologic application was the telescopic observations of the moon [22], [26], [30], [33], [34], which demonstrated the presence of the lunar dust layer and the many anomalies caused by rock fragments in the vicinity of bright-ray craters.

Terrestrial studies have been conducted both from aircraft and from satellite. Aircraft overflight data have been used to distinguish various geologic materials: olivine, basalt, and lapilli (ash beach deposits) and lacustrine carbonate deposits in the Mono Lake area, Calif. [11]; sedimentary bedrock versus windblown sand cover and individual siltstone and sandstone strata in the Imperial Valley, Calif. [31]; alluvial soils in the Rio Grande Valley, Tex. [23]; dolomites and limestones including facies changes between them in Mill Creek, Okla. [29]; soils of varying density in the Caliente and Temblor Ranges, Calif. [48].

Terrestrial satellite observations have indicated thermal property differences which are measurable from space [24], and which have been used to map different geologic materials [28]. Planetary probe data acquired of Mars [17] and Mercury [6] show the presence of some thermal property variations at a fairly coarse resolution (50–100 km) which are probably due, as in the Moon case, to surface and near-surface rock fragments.

The surface temperature variation of a periodically heated homogeneous half-space is dependent on a single thermal property called the thermal inertia (4) and (17). This property, which is the ratio of thermal conductivity to the square root of the thermal diffusivity, correlates somewhat linearly with the density for most dry geologic materials (Fig. 6). In addition, minerals and rocks high in silica (e.g., quartz, rhyolite, granite) lie above the correlation line (having somewhat higher thermal inertias than expected for their densities), and minerals and rocks low in silica and high in iron (e.g., olivine, basalt, gabbro, dunite) lie below the correlation line (having somewhat lower thermal inertias than expected for their densities). Due primarily to their higher conductivity and specific heat, dolomites generally have higher thermal inertias than limestones. The addition of moisture to a dry soil results in a significantly larger increase in thermal inertia than should be expected for the increased density. This result is due to the replacement of air with water, significantly changing both the specific heat and the conductivity. For example, a dry sandy soil (density $1.65\ \text{g/cm}^3$, specific heat $0.19\ \text{cal/g}$, and conductivity 0.00063

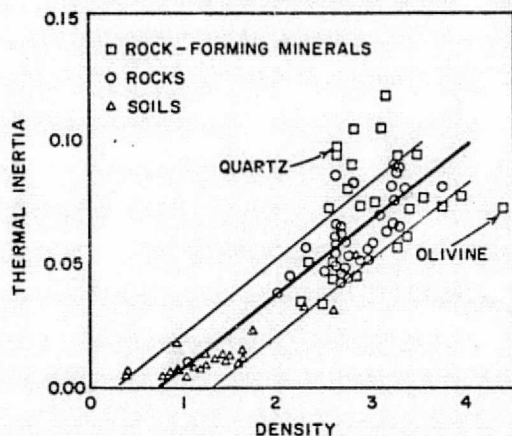


Fig. 6. Thermal inertia ($\text{cal/cm}^2/\text{s}^{1/2}$) versus density (g/cm^3) for a variety of rock-forming minerals, rocks, and soils. The linear correlation line, bracketed by lines showing the standard deviation, shows the increase of thermal inertia with increasing density. Rocks and rock-forming minerals which are high in silica tend to fall above the line (see quartz). Those which are low in silica and high in iron oxide tend to fall below the line (see olivine).

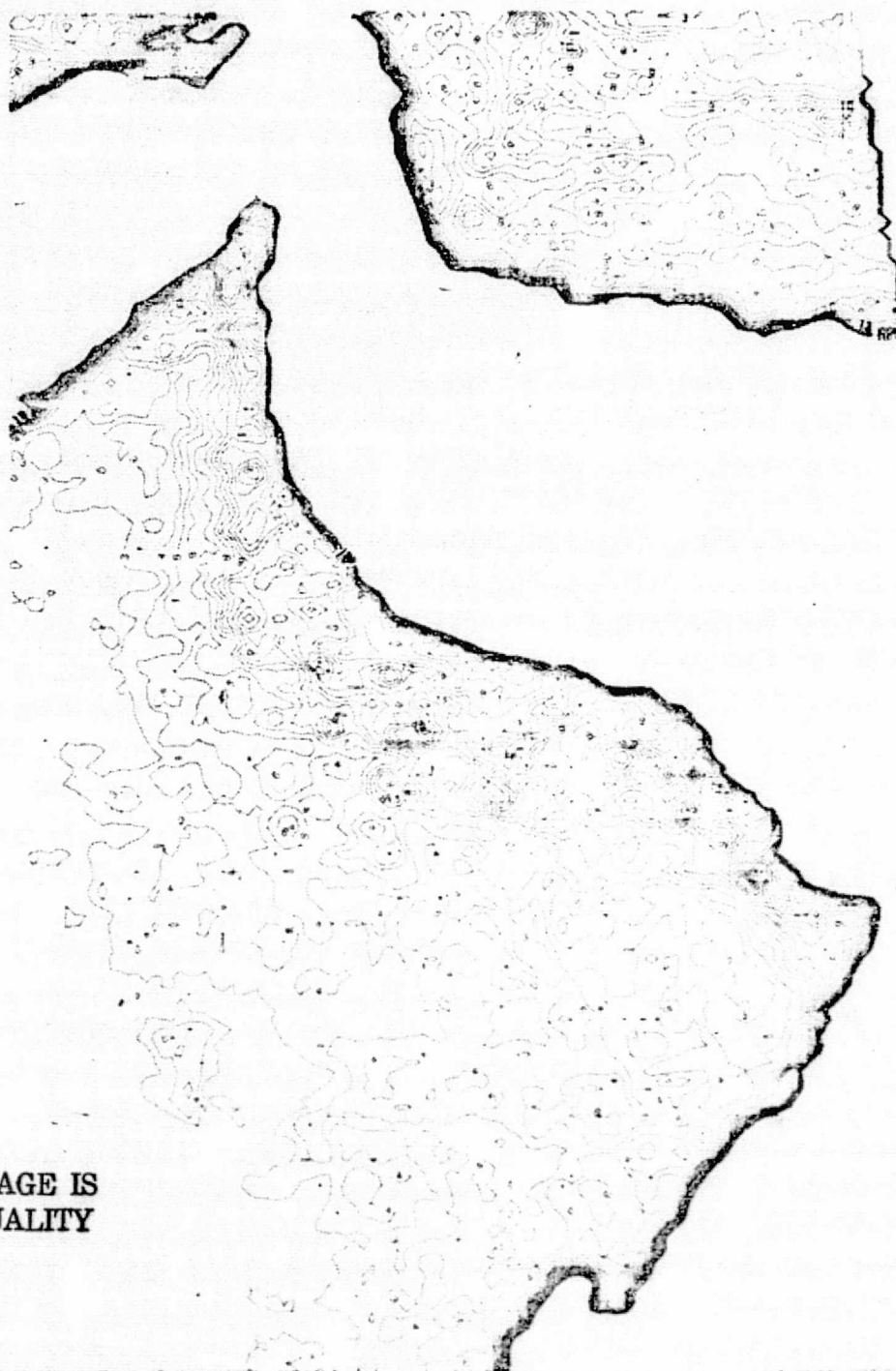
$\text{cal/cm}^2/\text{cm/s/degree}$ [4]) has a thermal inertia of $0.014\ \text{cal/cm}^2/\text{s}^{1/2}$. On the other hand, a thermal inertia value of 0.043 for a water-saturated soil (density $1.93\ \text{g/cm}^3$) can be derived from the expression in [45] based on Sugawara and Yoshizawa's equation for the thermal conductivity of porous material [35]. The saturated soil has a thermal inertia only slightly less than that of a sandstone— 0.056 (density $2.3\ \text{g/cm}^3$).

In their natural state, geologic materials are commonly oxidized, stained, lichen covered, and covered with residual soils and various types of vegetation. Discrimination of geologic units by the thermal inertia technique depends on the extent to which these surface effects provide distinguishable thermal characteristics. A model consisting of an insulating layer over a homogeneous half-space was constructed [43] in order to examine the extent of some of these surface effects. Both a 0.01-cm "lichen" layer and a 0.1-cm "soil" layer have a negligible effect; a 1-cm lichen layer and a 10-cm soil layer produce a surface temperature similar to an infinitely thick soil cover. Clearly then, the thermal inertia mapping technique is only applicable to rock-type discrimination in areas of good geologic exposure such as those found in arid and semiarid regions.

The technique has been applied using data acquired from the Nimbus meteorological satellites (8-km resolution) for part of Oman in the Arabian peninsula [28]. The test site was selected mainly because of excellent exposures of diverse rock and soil types of large areal extent. The resulting map showed gross agreement with the major units on a reconnaissance geologic map. Some anomalies which did not correspond to features on the reconnaissance map, subsequently, were found to match features on a more detailed geologic map or in a more detailed image obtained by the ERTS spacecraft [27]. The technique has now been computer-automated and refined using atmospheric correction models. A preliminary map of the eastern part of the Arabian peninsula is shown in Fig. 7. Higher resolution data from existing and future satellites should make it possible to apply the thermal inertia technique to discrimination of geologic materials and to study soil moisture conditions.

ADDITIONAL APPLICATIONS

So far I have discussed those geologic applications which are based on a quantitative analysis of repetitively acquired images using a theoretical model. Other applications have been devel-



ORIGINAL PAGE IS
OF POOR QUALITY

Fig. 7. Thermal inertia map of part of the eastern Arabian peninsula from 20 to 27° N latitude and from 55 to 60° E longitude. Contour values are multiplied by 0.005 to yield thermal inertia in $\text{cal/cm}^2/\text{s}^{1/2}$.

oped from visual examination of the image data. Reference has already been made to their use to monitor effusive volcanism and to detect steaming ground and hot springs. Groundwater migration to the surface can cause, in addition to the obvious thermal property change, surface-temperature cooling due to evaporation (from bare ground) or evapotranspiration (from vegetation). In some instances this enables recognition of fractures and fault zones [29], [32], [41]. In other cases, the surface cooling can lead to the recognition of areas of potential land slippage [49], [3].

Thermal images showing contrasts due to differential warming of oppositely facing surfaces commonly provide an enhanced display of various topographic features. In some instances, this has resulted in the detection of lineaments which can provide information on the regional structure, and in some cases, may be related to the deposition of economically valuable minerals [49]. Topographic effects can also produce a thermal image pattern which provides geomorphic information ultimately related to such matters as rock type, fracturing, and erosion. In some cases, this prompted the conclusion that post-

sunrise images resemble low-sun angle photography [48]. In other cases, the images have aided in recognizing stratigraphic and structural detail [29], [31]. Rowan *et al.* report enhancement of small-scale bedding detail in morning images and of alternating formations that form hogbacks and valleys in afternoon images. It may be possible to apply pattern recognition criteria to these images in order to develop discrimination criteria for different geologic materials, and to quantify the effects of various geomorphic processes which act to modify the surfaces.

SUMMARY

Thermal infrared images have been used to monitor effusive volcanism, delineate areas of steaming altered ground and hot-spring activity, detect fractures, and discriminate a variety of geologic materials. Because the interpretation of these images is complicated by the effects of many geologic, meteorologic, and hydrologic factors, a theoretical model was developed which can be used to predict optimum times for data acquisition to determine quantitative values of various terrain properties.

The model assumes one-dimensional periodic heating of a uniform half-space conductive heat transfer in the ground, and radiative transfer in the atmosphere. The resulting diurnal temperature variation is expressed as a function of geologic properties (albedo, thermal inertia, emissivity, and geothermal flux), topography (slope and azimuth), and solar-atmospheric properties (transmission, sky radiance, site latitude, solar declination, and cloud cover). Two important properties of the diurnal temperature variation are computed: the mean diurnal temperature and the day-night temperature difference. The mean diurnal temperature is independent of the thermal inertia of the ground, and can be used in conjunction with albedo measurements and topographic data to derive the geothermal flux. The ratio of day-night temperature difference to the complement of albedo is dependent, to first order, only on the thermal inertia and hence the ratio can be used to discriminate geologic material.

Geothermal application of thermal images has been limited in the past by the geologic-topographic "noise" factors which can easily overwhelm all but the most intense anomalies. A theoretical analysis suggests that both thermal and reflectance image data should be acquired at least three times in the diurnal cycle. A limited application of the model to data acquired at an optimum time illustrated the presence of a weak thermal anomaly which was confirmed by ground measurements. It is still premature, however, to estimate a minimum detectable flux using this technique.

Thermal inertia mapping from Nimbus satellite data has already demonstrated the feasibility of discriminating a variety of geologic materials. Planetary probe data display thermal-property variations which are probably due to near-surface rock fragments. The dependence of thermal inertia on density, on moisture content, and, to some degree, on composition suggests that the technique should be useful to discriminate a great variety of geologic materials and conditions. Other geologic applications of thermal mapping include ground-water monitoring and geomorphic and structural studies.

ACKNOWLEDGMENT

The author is indebted to Anne B. Kahle of the Jet Propulsion Laboratory, California Institute of Technology, Pasadena, Calif., for correcting an error in the author's previous formulation for the local zenith angle.

REFERENCES

- [1] C. W. Allen, *Astrophysical Quantities*. London, England: Athlone Press, 1963, p. 127.
- [2] C. J. Banwell, "Geophysical techniques in geothermal exploration," in *U.N. Symp. Development and Utilization of Geothermal Resources*, vol. 1, 1970.
- [3] M. B. Blanchard, R. Greeley, and R. Goettelman, "Use of visible, near-infrared, and thermal infrared remote sensing to study soil moisture," NASA Tech. Memo. TM X-62,343, Apr. 1974.
- [4] H. S. Carslaw and J. C. Jaeger, *Conduction of Heat in Solids*, 2d ed. New York: Oxford Univ. Press, 1959.
- [5] R. Cassinis, C. M. Mar. ., and A. M. Tonelli, "Ground and airborne thermal imagery on Italian volcanic areas," in *U.N. Symp. Development and Utilization of Geothermal Resources*, vol. 2, pt. 1, pp. 413-419, 1970.
- [6] S. C. Chase *et al.*, "Preliminary infrared radiometry of the night side of Mercury from Mariner 10," *Science*, vol. 185, no. 4146, pp. 142-144, 1974.
- [7] W. W. Coblenz, "Radiometric investigations of infrared absorption and reflection spectra," *U.S. Nat. Bur. Stand. Bull.*, vol. 2, pp. 457-462, 1906.
- [8] K. L. Coulson and D. W. Reynolds, "The spectral reflectance of natural surfaces," *J. Appl. Meteorol.*, vol. 10, pp. 1285-1295, 1971.
- [9] P. S. Epstein, "What is the Moon made of," *Amer. Phys. Soc.*, vol. 33, p. 269, 1929.
- [10] W. A. Fischer, R. M. Moxham, F. Polcyn, and G. H. Landis, "Infrared surveys of Hawaiian volcanoes," *Science*, vol. 146, pp. 733-742, 1964.
- [11] J. D. Friedman, "Thermal anomalies and geologic features of the Mono Lake area, California as revealed by infrared imagery," *U.S. Geol. Surv. Tech. Lett. NASA-82*, Sept. 1968.
- [12] H. Hase, "Surface heat flow studies for remote sensing of geothermal resources," in *Proc. 7th Int. Symp. Remote Sensing of Environment*, vol. 1, pp. 237-245, 1971.
- [13] M. P. Hochstein and D. J. Dickinson, "Infrared remote sensing of thermal ground in the Taupo region, New Zealand," in *U.N. Symp. Development and Utilization of Geothermal Resources*, vol. 2, pt. 1, pp. 420-423, 1970.
- [14] W. A. Hovis, Jr., "Optimum wavelength intervals for surface temperature radiometry," *Appl. Opt.*, vol. 5, pp. 815-818, 1966.
- [15] J. C. Jaeger, "Pulsed surface heating of a semi-infinite solid," *Quart. Appl. Math.*, vol. 11, pp. 132-137, 1953a.
- [16] —, "Conduction of heat in a solid with periodic boundary conditions, with an application to the surface temperature of the Moon," *Proc. Cambridge Phil. Soc.*, vol. 49, pt. 2, pp. 355-359, 1953b.
- [17] H. H. Kieffer, S. C. Chase, Jr., E. Miner, G. Munch, and G. Neugebauer, "Preliminary report on infrared radiometric measurements from the Mariner 9 spacecraft," *J. Geophys. Res.*, vol. 78, no. 20, pp. 4291-4312, 1973.
- [18] R. J. P. Lyon, "Evaluation of infrared spectrophotometry for compositional analysis of lunar and planetary soils (Part III)," NASA Rep. NASA-CR-100, Nov. 1964.
- [19] J. H. McLerran and O. J. Morgan, "Thermal mapping of Yellowstone National Park," in *Proc. 3rd Int. Symp. Remote Sensing of Environment*, pp. 517-530, 1965.
- [20] L. D. Miller, "Location of anomalously hot earth with infrared imagery in Yellowstone National Park," in *Proc. 4th Int. Symp. Remote Sensing of Environment*, pp. 751-769, 1965.
- [21] R. M. Moxham, "Aerial infrared surveys at The Geysers geothermal steam field, California," *U.S. Geol. Surv. Prof. Paper* 650-C, pp. C106-C122, 1967.
- [22] B. C. Murray and R. L. Wildey, "Surface temperature variations during the lunar nighttime," *Astrophys. J.*, vol. 139, pp. 734-750, 1964.
- [23] V. J. Myers and M. D. Heilman, "Thermal infrared for soil temperature studies," *Photogrammetr. Eng. J.*, pp. 1024-1032, 1969.
- [24] W. Nordberg and R. E. Samuelson, "Terrestrial features observed by the high resolution infrared radiometer," observations from the Nimbus I satellite, NASA Rep. NASA-SP-89, pp. 37-46, 1965.
- [25] G. Palmason, J. D. Friedman, R. S. Williams, Jr., J. Jonsson, and K. Saemundsson, "Aerial infrared surveys of Reykjanes and Torfajökull thermal areas, Iceland, with a section on the cost of exploration surveys," in *U.N. Symp. Development and Utilization of Geothermal Resources*, vol. 2, pt. 1, pp. 399-412, 1970.
- [26] E. Pettit and S. B. Nicholson, "Lunar radiation and temperature," *Astrophys. J.*, vol. 71, pp. 102-135, 1930.
- [27] H. A. Pohn, "A comparison of ERTS images and Nimbus thermal-inertia mapping of Oman," unpublished (in review by U.S. Geol. Surv.).
- [28] H. A. Pohn, T. W. Offield, and K. Watson, "Thermal inertia mapping from satellite-Discrimination of geologic units in Oman," *J. Res. U.S. Geol. Surv.*, vol. 2, no. 2, pp. 147-158, 1974.
- [29] L. C. Rowan, T. W. Offield, K. Watson, J. P. Cannon, and R. D.

- Watson, "Thermal infrared investigations, Arbuckle Mountains, Oklahoma," *Geol. Soc. Amer. Bull.*, vol. 81, pp. 3549-3562, 1970.
- [30] J. M. Saari and R. W. Shorthill, "Isotherms of crater regions on the illuminated and eclipsed moon," *Icarus*, vol. 2, p. 115, 1963.
- [31] F. F. Sabins, Jr., "Thermal infrared imagery and its application to structural mapping in southern California," *Geol. Soc. Amer. Bull.*, vol. 80, pp. 397-404, 1969.
- [32] —, "Infrared imagery and geologic aspects," *Photogrammetric Eng. J.*, pp. 743-750, July 1967.
- [33] R. W. Shorthill and J. M. Saari, "Nonuniform cooling of the eclipsed Moon: A listing of thirty prominent anomalies," *Science*, vol. 150, no. 3693, pp. 210-212, 1965.
- [34] W. M. Sinton, "Temperatures of the lunar surface," in *Physics and Astronomy of the Moon*, Z. Kopal, Ed. New York: Academic Press, 1962, ch. 11.
- [35] A. Sugawara and Y. Yoshizawa, "An investigation on the thermal conductivity of porous materials and its application to porous rock," *Aust. J. Phys.*, vol. 14, p. 469, 1961.
- [36] R. S. Vickers and R. J. P. Lyon, "Infrared sensing from spacecraft: A geologic interpretation," in *Thermophysics of Spacecraft and Planetary Bodies*, G. B. Heller, Ed. New York: Academic Press, 1967, pp. 585-607.
- [37] R. K. Vincent and F. Thomson, "Spectral compositional imaging of silicate rocks," *J. Geophys. Res.*, vol. 77, no. 14, pp. 2465-2472, 1972a.
- [38] —, "Rock-type discrimination from ratioed infrared scanner images of Pisgah Crater, California," *Science*, vol. 175, no. 4025, pp. 986-988, 1972b.
- [39] R. K. Vincent, R. Thomson, and K. Watson, "Recognition of exposed quartz sand and sandstone by two-channel infrared imagery," *J. Geophys. Res.*, vol. 77, no. 14, pp. 2473-2477, 1972.
- [40] R. K. Vincent, "The NASA Earth resources spectral information system: A data compilation, second supplement," *Environ. Res. Inst. Mich.*, NASA Rep. NASA-CR-ERIM 31650-156-T, pp. 101-1-103-10, Apr. 1973.
- [41] R. E. Wallace and R. M. Moxham, "Use of infrared imagery in study of the San Andreas fault system, California," *U.S. Geol. Surv. Prof. Paper* 575-D, pp. 147-156, 1967.
- [42] K. Watson, "Geothermal reconnaissance from quantitative analysis of thermal infrared images," in *Proc. 10th Int. Symp. Remote Sensing of Environment*, vol. 5, 1974.
- [43] —, "Periodic heating of a layer over a semi-infinite solid," *J. Geophys. Res.*, vol. 78, no. 26, pp. 5904-5910, 1973.
- [44] —, "A computer program of thermal modeling for interpretation of infrared images," U.S. Geol. Surv. Rep. USGS-GD-71-023; available from Dep. Commerce, Nat. Tech. Inform. Serv., Springfield, Va., NTIS PB-203-578, 1971.
- [45] K. Watson, L. C. Rowan, and T. W. Offield, "Application of thermal modeling in the geologic interpretation of IR images," in *Proc. 7th Int. Symp. Remote Sensing of Environment*, vol. 3, pp. 2017-2041, 1971.
- [46] A. F. Wesselink, "Heat conductivity and nature of the lunar surface material," *Bull. Astron. Inst. Neth.*, vol. 10, no. 390, pp. 351-363, 1948.
- [47] D. E. White and L. D. Miller, "Calibration of geothermal infrared anomalies of low intensity in terms of heat flow," *EOS (Amer. Geophys. Union Trans.)*, vol. 50, p. 348, 1969.
- [48] E. W. Wolfe, "Thermal IR for geology," *Photogrammetric Eng. J.*, vol. XXXVII, no. 1, pp. 43-52, 1971.
- [49] a) T. W. Offield, oral communication, 1974.
b) —, unpublished data, 1974.

Thermal microwave emission from a halfspace containing scatterers

A. W. England

US Geological Survey, Denver, Colorado 80225

(Received November 5, 1973.)

The microwave brightness of heterogeneous materials is decreased by internal scattering. This study, based upon radiative transfer theory, shows that for low loss media darkening can be many tens of degrees, that the effect is greater for materials of lower dielectric constant, that darkening depends upon the dominance of scattering over absorption, that volume scattering tends to mask a temperature gradient, that darkening is slightly greater for V - than for H -polarized radiation, and that darkening increases slightly with view angle. For isotropic scattering, the analysis yields the brightness temperature as a function of the scattering albedo, the complex dielectric constant, thermal temperature, and the temperature gradient.

INTRODUCTION

Thermal radiation from rock, soil, or snow may be used remotely to infer physical properties such as temperature, dielectric constant, moisture content, or thermal inertia. Interpreting thermal-infrared emission (8 to 14 μ) is eased by assuming that the radiation is diffuse and that it originates at the optical surface. Interpreting microwave emission (10^{-3} to 10^0 m) is, in this sense, less simple. Surfaces are seldom sufficiently rough to produce diffuse radiation nor are they quasi-specular. Much of the radiated energy may originate several wavelengths below the optical surface forcing consideration of the physical characteristics of an emitting volume as well as the roughness of the surface. Pebbles in soil, ice glands in snow, vesicles in lava, stratification, or foliation scatters the radiation internally and so the emitter cannot be modeled as a homogeneous halfspace bounded by a rough interface. The contributing effects of surface roughness, volume scattering, and layering must be unraveled before thermal temperature or dielectric properties can be ferreted from thermal microwave emission.

Stogryn [1970] solved the theoretical problem of emission from a uniformly layered halfspace, and Blinn *et al.* [1972] have observed the expected interference patterns. Edgerton *et al.* [1971] discussed emission from a non-uniformly layered halfspace in an attempt to explain the anomalous microwave signature of a metamorphosed, layered snowpack. Emission through a rough surface might be treated

similarly to problems of radar backscatter [e.g., Beckman and Spizzichino, 1963; Peake, 1959; Stogryn, 1967].

This paper concerns emission from a halfspace containing randomly distributed scatterers embedded in a low loss dielectric and considers the relative influences of a temperature gradient, the dielectric constant, and absorption.

THEORY

The model in Figure 1 is of an isotropic, low loss dielectric occupying the negative halfspace bounded at $z = 0$. The surface is quasi-specular (effectively specular at the wavelength of concern), the temperature within the dielectric is a function of depth ($-z$), and the complex dielectric constant is ϵ^* ($= \epsilon' - i\epsilon''$). The dielectric contains randomly distributed scattering centers of cross section σ , and density N . These are point scatterers and neither absorb nor emit but merely scatter. The radiation intensity at a point within the dielectric is specified completely by four parameters—those typically chosen are the Stokes parameters. Because the radiation intensity is rotationally symmetrical about the z axis, phase information need not be preserved and the required number of Stokes parameters is reduced by half. That is, the total intensity can be written as the sum of horizontally and vertically polarized radiation, $I_H + I_V$. The radiation intensity at wavelength λ_0 within the dielectric is an explicit function only of z , and of angle ϕ' between the direction of energy flow and $+z$. If μ is the cosine of the angle ϕ' , then the intensity can be written $I_p(z, \mu)$ where

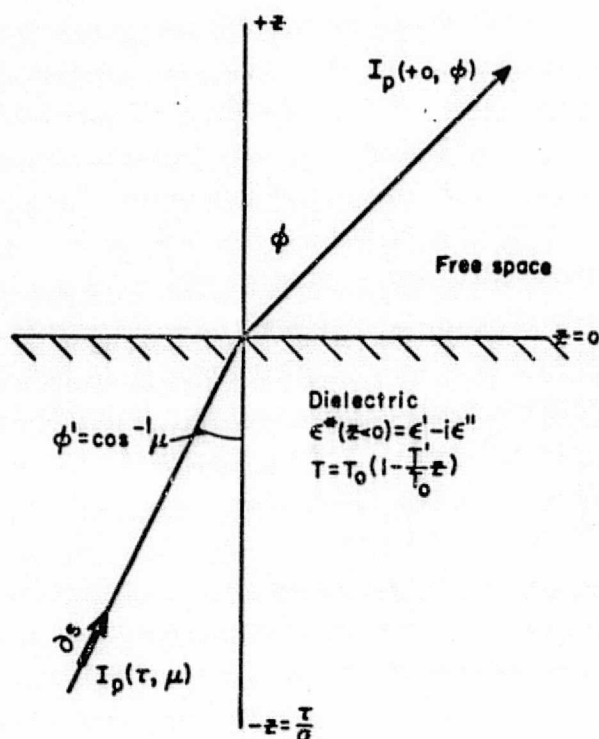


Fig. 1. Model for thermal emission for an isotropic dielectric occupying the halfspace $z < 0$. At a specific wavelength, $I_p(\tau, \mu)$ is the radiation intensity within the dielectric where τ is the optical depth below the surface, and μ is $\cos \phi'$, cosine of the angle between the direction of propagation and vertical. The radiation intensity above the surface is denoted $I_p(+0, \phi)$ where ϕ is view angle. The subscript p refers to either horizontally or vertically polarized radiation.

polarization p is either H or V . The explicit dependence upon wavelength is suppressed. Note that ϕ' and μ , whether μ is primed or not, refer to direction within the dielectric. By convention, ϕ is reserved for view angle above the dielectric.

The equation for radiative transfer at $z < 0$ becomes

$$\partial I_p(z, \mu) / \partial s = -\alpha I_p(z, \mu) + E_p(z) + (\omega_0 \alpha / 2) \sum_{q=H,V} \int_{-1}^{+1} P_{pq}'(\mu, \mu') I_q(z, \mu') d\mu' \quad (1)$$

where ∂s is an interval along the direction of energy flow, and α is defined as

$$\alpha \equiv 2\beta + N\sigma \quad (2)$$

i.e., the sum of the absorption and scattering coefficients respectively. In terms of the complex dielectric constant or of the loss tangent, $\tan \delta$,

$$2\beta = [2\pi(\epsilon')^{1/2}/\lambda_0] \epsilon'' / \epsilon' = [2\pi(\epsilon')^{1/2}/\lambda_0] \tan \delta \quad (3)$$

$E_p(z)$ is the directional spectral emissive power in p , polarization, and ω_0 is the scattering albedo,

$$\omega_0 \equiv N\sigma/\alpha \quad (4)$$

$P_{pq}'(\mu, \mu')$ is the normalized scattering phase function applicable where there exists rotational symmetry. That is, $P_{pq}'(\mu, \mu')$ relates the radiation in all azimuths of μ' to that scattered into one azimuth of μ . To paraphrase equation 1, the change in intensity along ∂s is less by the radiation absorbed and scattered and greater by the self-emission of the material along ∂s and greater by the radiation scattered into the direction of ∂s from all other directions. Recast in a more convenient form, equation 1 becomes

$$\mu \partial I_p(\tau, \mu) / \partial \tau = I_p(\tau, \mu) - E_p/\alpha - (\omega_0/2) \sum_{q=H,V} \int_{-1}^{+1} P_{pq}'(\mu, \mu') I_q(\mu, \mu') d\mu' \quad (5)$$

where $\tau (= -\alpha Z)$, called the optical depth, is the optical thickness with reference to the surface.

Equation 5 is a perfectly general integro-differential equation describing radiative transfer within a scattering and absorbing medium provided that the scatters are randomly distributed in a matrix whose properties vary slowly with respect to the wavelength, and that scatter interaction is not dependent upon the path length between scatterers. In practice, the latter requirement, that of far-field interactions, is seldom realized in solid body geophysics. This constitutes a basic limitation to the quantitative, unqualified application of this theory. The notation and formulation leading to equation 5 follow closely that of Chandrasekhar [1960] as will the means to a solution. The problem differs from most problems of atmospheres as treated by Chandrasekhar in that the dielectric is strongly self-emitting, that the scatterers do not emit or absorb, and that the interface serves as a partial, specular reflector. One should note, however, that the validity of the approach is not compromised by these differences.

A boundary condition for solution of equation 5 is that the Fresnel reflection coefficients govern the intensity of radiation reflected into the medium by the surface, i.e.,

$$I_p(0, -\mu) = R_p(\mu) I_p(0, \mu) \quad (\mu > 0) \quad (6)$$

where $R_p(\mu)$ are the Fresnel coefficients. The coefficients, expressed in terms of μ , are [Stratton, 1941]

$$R_V(\mu) = \left\{ \frac{\mu - (\epsilon')^{1/2}(1 - \epsilon' + \epsilon'\mu^2)^{1/2}}{\mu + (\epsilon')^{1/2}(1 - \epsilon' + \epsilon'\mu^2)^{1/2}} \right\}^2$$

$$R_H(\mu) = \left\{ \frac{(\epsilon')^{1/2}\mu - (1 - \epsilon' + \epsilon'\mu^2)^{1/2}}{(\epsilon')^{1/2}\mu + (1 - \epsilon' + \epsilon'\mu^2)^{1/2}} \right\}^2 \quad (7)$$

for ϕ' less than the angle of total reflection and $R_p(\mu) = 1$ for ϕ' greater than the angle of total reflection.

The emissive power of a dielectric is dependent upon the complex dielectric constant and upon thermal temperature, and, for isotropic media, is not dependent upon polarization. Consider an $E(z)$ that is a linear function of z . In the absence of scatterers, i.e., $\omega_0 = 0$, the solution to equation 5 for $\mu > 0$ is

$$I_p(\tau, \mu)_{\omega_0=0} = (E_0/2\beta)[1 - (E'/2\beta E_0)(\tau + \mu)] \quad (8)$$

where

$$E_0 = E_p(0)$$

$$E' = [\partial E_p(z)/\partial z]_{z=0} \quad (9)$$

Note that equation 8 is not the general solution to equation 5. A particular solution to the homogeneous equation is $Ae^{\tau/\mu}$. This, however, would apply to the radiation reflected downward by the surface, i.e., $A = 0$ for $\mu > 0$ and $A = I_p(0, \mu)$ for $\mu < 0$.

Immersed in a blackbody cavity of thermal temperature T_0 , the dielectric will acquire uniformly the temperature T_0 , and E' will be zero. By Kirchhoff's law [Siegel and Howell, 1968], the radiation absorbed by the dielectric must be balanced by escaping radiation. Accordingly,

$$[1 - R_p(\mu)]I_{bp}(T_0)$$

$$= \{[1 - R_p(\mu)]/\epsilon'\} I_p(0, \mu)_{\omega_0=0} \quad (\mu > 0) \quad (10)$$

where $[1 - R_p(\mu)]$ is the fraction of blackbody intensity, $I_{bp}(T_0)$, absorbed and $[1 - R_p(\mu)] I_p(0, \mu)_{\omega_0=0}/\epsilon'$ is the intensity of thermal radiation emitted. The ϵ' divisor results from the divergence as a beam passes into a medium of lower dielectric constant. The microwave blackbody intensity given by the Rayleigh-Jeans law [Slater, 1939] is

$$I_{bp}(T) = CT \quad (11)$$

where C is a constant. Therefore, the emissive power resulting from equations 8, 10, and 11 is

$$E = (2\beta)(\epsilon')CT \quad (12)$$

and the intensity within the dielectric becomes

$$I_p(\tau, \mu)_{\omega_0=0} = \epsilon'CT_0[1 - (T'/2\beta T_0)(\tau + \mu)] \quad (13)$$

where T_0 is the surface temperature and T' is the temperature gradient.

The solution to the transfer equation is greatly simplified by assuming isotropic scattering. That is, radiation impinging upon a scatterer is redistributed evenly in all directions. If, for further mathematical tractability, the energy is partitioned according to polarization, then

$$P_{pq}'(\mu, \mu') = \delta_{pq} \quad (14)$$

where δ_{pq} is the Kronecker delta. Making this simplification is troublesome because all realistic scattering phase functions have off-diagonal terms. The consequences of this simplification will be apparent. Incorporating this, the emissive power (equation 12), and an assumed constant temperature gradient into equation 5 yields

$$\mu \partial I_p(\tau, \mu)/\partial \tau = I_p(\tau, \mu) - (2\beta\epsilon'CT_0/\alpha)$$

$$\cdot (1 - T'\tau/\alpha T_0) - (\omega_0/2) \int_{-1}^{\tau+1} I_p(\tau, \mu') d\mu' \quad (15)$$

Equation 15 is not amenable to solution in closed form. Physically, $I_p(\tau, \mu)$ is expected to be continuous through τ and μ . Consequently, the integral can be replaced by a Gaussian quadrature, i.e., an appropriately weighted sum over $2n$ intervals between the $2n$ zeroes of the even-order Legendre polynomial $P_{2n}(\mu)$. The solution achieved is at least as good as a power series in μ to degree $(4n - 1)$. The approximation in terms of $\mu (= \cos \phi')$ is appropriate because the intensity is symmetric with respect to ϕ' , i.e., $I_p(z, +\phi') = I_p(z, -\phi')$. The resulting approximation to equation 15 is

$$\mu_i \partial I_p(\tau, \mu_i)/\partial \tau = I_p(\tau, \mu_i) - (2\beta\epsilon'CT_0/\alpha)$$

$$\cdot (1 - T'\tau/\alpha T_0) - (\omega_0/2) \sum_{i=-n}^{+n} a_i I_p(\tau, \mu_i) \quad (16)$$

where $i = \pm 1, \dots, \pm n$, and the a_i , called the Christoffel numbers, are the weighting coefficients [Love, 1966]. The zeroes and coefficients obey the following:

$$a_i = a_{-i}; \mu_i = -\mu_{-i}; \sum_{i=1}^n a_i = 1 \quad (17)$$

The solution to equation 16 is

$$I_p(\tau, \mu_i) = \sum_{j=1}^n L_{ij} e^{-k_j \tau} / (1 + k_j \mu_i)$$

$$+ \epsilon'CT_0[1 - T'(\tau + \mu_i)/\alpha T_0] \quad (18)$$

where k_j are the n positive roots of the characteristic equation

TABLE 1. Combinations of the parameters for which brightness temperatures were computed.

ω_0 (scattering albedo)	0.1, 0.3, 0.5, 0.7, 0.9
ϵ' (dielectric constant)	1.0, 2.25, 6.25, 12.25
α (dielectric loss)	1.0 (m ⁻¹)
$\partial T/\partial z$ (negative thermal gradient)	0, -1.0, -10.0, -100.0 (K m ⁻¹)
T_0 (surface thermal temperature)	300 K
n (order of approximation)	1, 3, 5, 7, 8, 9, 10, 11, 14, 15

$$1 = \omega_0 \sum_{i=1}^n a_i / (1 - \mu_i^2 k_i^2) \quad (19)$$

and the L_{pi} are defined by the boundary conditions at $\tau = 0$ (equation 6). Using equation 17

$$I_p(0, \mu_i) = \sum_{i=1}^n L_{pi} / (1 + k_i \mu_i) + \epsilon' C T_0 [1 - T' \mu_i / \alpha T_0]$$

$$I_p(0, -\mu_i) = \sum_{i=1}^n L_{pi} / (1 - k_i \mu_i) + \epsilon' C T_0 [1 + T' \mu_i / \alpha T_0] \quad (20)$$

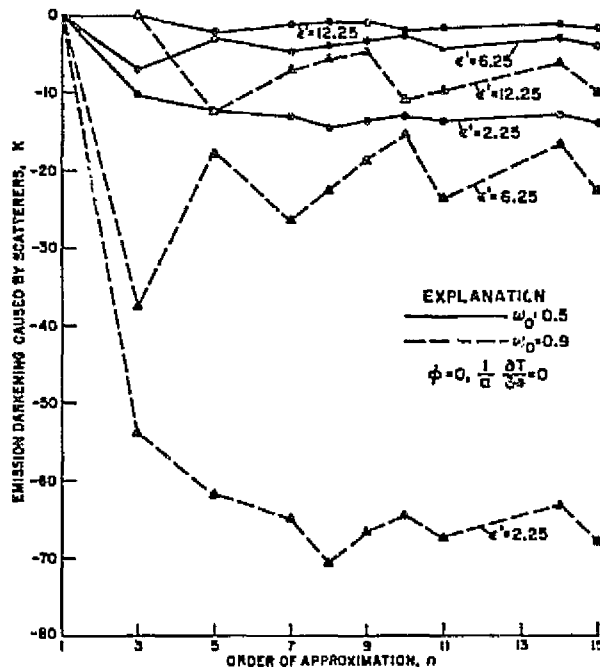


Fig. 2. Convergence of the solutions for emission darkening as a function of the order of the approximation. Cases are shown for an extreme scattering albedo, $\omega_0 = 0.9$, and an intermediate scattering albedo, $\omega_0 = 0.5$.

These and equation 6 have the solution

$$R_p L_p + A_p = 0 \quad (21)$$

where the elements of the matrices R_p and A_p are

$$R_{pji} = \frac{\{[1 - R_p(\mu_i)] + k_i \mu_i [1 + R_p(\mu_i)]\}}{(1 - k_i^2 \mu_i^2)} \quad (22)$$

and

$$A_{pi} = \epsilon' C T_0 \{[1 - R_p(\mu_i)] + (T' \mu_i / \alpha T_0) [1 + R_p(\mu_i)]\} \quad (23)$$

Therefore, the elements, L_{pi} , of the coefficient matrix L_p are

$$L_{pi} = - \sum_{i=1}^n R_{pji}^{-1} A_{pi} \quad (24)$$

where R_{pji}^{-1} are the elements of the $n \times n$ inverse matrix of R_p .

The radiation intensity above the dielectric is

$$I_p(+z, \phi_i) = \{[1 - R_p(\mu_i)] / \epsilon'\} I_p(0, \mu_i) \quad (25)$$

where the view angle, ϕ_i , and μ_i are related by Snell's law,

$$\sin \phi_i = (\epsilon')^{1/2} \sin(\cos^{-1} \mu_i) \quad (26)$$

$I_p(+z, \phi_i) / C$ has the dimension of temperature and is commonly called the brightness temperature, $T_{Bp}(\phi_i)$. Therefore, equations 18 and 25 specify the brightness temperature

$$T_{Bp}(\phi_i) = \{[1 - R_p(\mu_i)] / \epsilon'\} \cdot \left\{ \sum_{i=1}^n L_{pi} / C(1 + k_i \mu_i) + \epsilon' T_0 (1 - T' \mu_i / \alpha T_0) \right\} \quad (27)$$

Similarly, from equations 13 and 25, $T_{Bp}(\phi_i)_{\omega_0=0}$ is

$$T_{Bp}(\phi_i)_{\omega_0=0} = [1 - R_p(\mu_i)] [T_0 (1 - T' \mu_i / 2\beta T_0)] \quad (28)$$

and the difference, $\Delta T_{Bp}(\phi_i)$, caused by scattering is

$$\Delta T_{Bp}(\phi_i) = T_{Bp}(\phi_i) - T_{Bp}(\phi_i)_{\omega_0=0} \quad (29)$$

ΔT_{Bp} is always negative and can be called the scatter-induced emission darkening.

RESULTS AND DISCUSSION

A set of solutions for ΔT_{Bp} (equation 29) was generated at each level of approximation $n = 1, 3, 5, 7, 8, 9, 10, 11, 14$, and 15. Each set consisted of solutions for every combination of parameters listed in Table 1. The convergence of the solutions with higher level approximations is illustrated in Figure

2. The relative convergence is more rapid the lower the dielectric constant. This can be understood from Table 2. The transmissivity of the dielectric's surface is relatively high for all values of μ_i between $\mu = 1.0$ and $\mu = \mu_{crit}(\epsilon')$. The transmissivity rapidly drops to zero at μ_{crit} (total reflection) and remains zero for $\mu < \mu_{crit}(\epsilon')$. The higher the dielectric constant the nearer $\mu_{crit}(\epsilon')$ is to 1.0. In the cases for $\epsilon' = 2.25$, the intervals of the Gaussian quadrature are well-spaced with respect to μ_{crit} (2.25). For $\epsilon' = 12.25$, however, there are only two intervals in the transmission window ($1.0 > \mu_i > \mu_{crit}(12.25)$) for $n = 10$, three for $n = 15$, and 4 for $n = 21$. The fidelity of the partitioned, isotropic scattering model probably does not warrant going to the twenty-first approximation. Data in this paper will be from the fifteenth approximation. Fortunately, the more interesting ΔT_B occur at low dielectric constants.

Solutions to equation 29 (Figure 3) for a dielectric whose temperature is uniform ($T' = 0$) show three relationships: (a) darkening caused by scattering depends upon the dominance of scattering over absorption (upon ω_0); (b) darkening is not explicitly dependent upon loss, α ; and (c) scatterers have greater effect, the lower the dielectric constant. Consider, for example, a homogeneous dielectric occupying the halfspace in Figure 1. If its loss tangent lies around 10^{-3} , most of the emergent microwave energy will originate many wavelengths below the surface. Adding a few percent liquid water to the medium scarcely affects its dielectric constant but increases its loss tangent by an order of magnitude. Because the emissivities of such relatively low loss homogeneous media depend only upon their dielectric constants, adding a few percent moisture would not affect the brightness temperature. The source of the radiation, however, would tend to be far deeper in the dry, lower loss case. If the dielectric contained scatterers, whether they are voids or are dielectrically contrasting inclusions, the effect upon brightness temperature would be greater for the dry medium. In the dry case, the deeper source of the radiation would insure that more energy is scattered and, subsequently, reabsorbed. In a low loss, scattering medium, the introduction of small amounts of liquid water reduces or even effectively eliminates scatter-induced darkening. Therefore, scatterers tend to play an insignificant role in emission from moist soil or from wet snow. In contrast, they can influence greatly the emission characteristics of porous ice, of

TABLE 2. Ratio of the number of zeroes of the n th-degree Legendre polynomial within the transmission window, $1.0 > \mu_i > \mu_{crit}(\epsilon')$, to the number at angles of total reflection, $\mu_i < \mu_{crit}(\epsilon')$. Note that $\mu_{crit}(2.25) = 0.74$, $\mu_{crit}(6.25) = 0.92$, and $\mu_{crit}(12.25) = 0.96$.

Order of approximation, n	ratio at		
	$\epsilon' = 2.25$	$\epsilon' = 6.25$	$\epsilon' = 12.25$
1	0/1	0/1	0/1
3	1/2	1/2	0/3
5	2/3	1/4	1/4
7	3/4	2/5	1/6
8	4/4	2/6	1/7
9	4/5	2/7	1/8
10	5/5	2/8	2/8
11	5/6	3/8	2/9
13	6/7	3/10	2/11
15	7/8	4/11	3/12
17	8/9	4/13	3/14
19	9/10	5/14	3/16
21	10/11	5/16	4/17

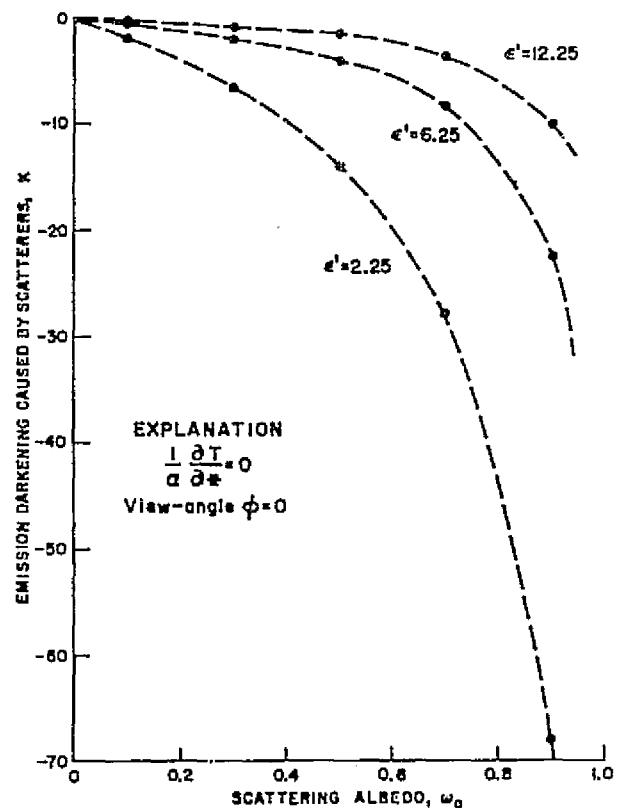


Fig. 3. The effect of scattering albedo upon emission darkening. ϵ' is the real part of the dielectric constant within the scattering volume. Note that darkening increases with the dominance of scattering over absorption (with ω_0), and that darkening increases with decreasing dielectric constant.

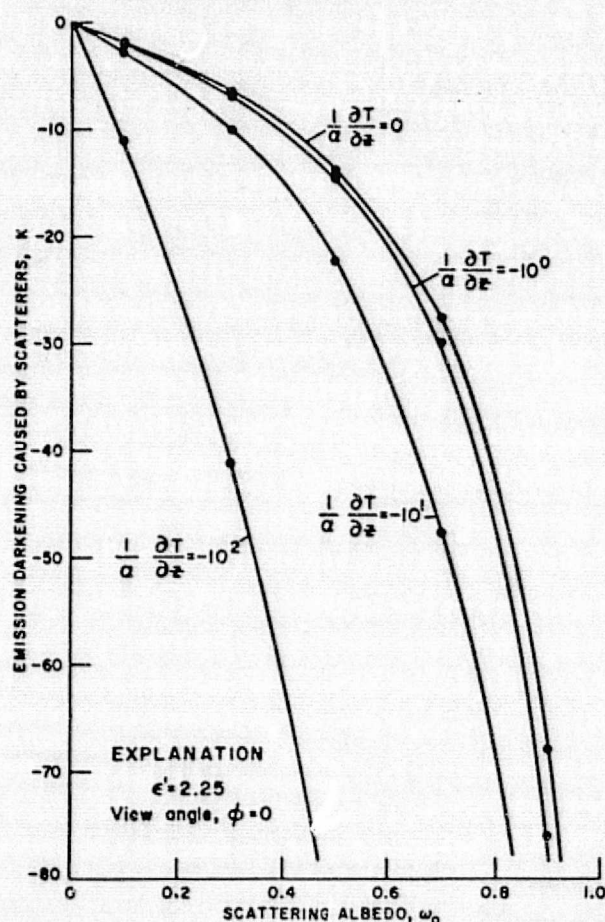


Fig. 4. Emission darkening caused by scattering within a medium where the temperature gradient is nonzero, $\epsilon' = 2.25$. Note that $+z$ is upward and so $\partial T/\partial z < 0$ represents an increasing temperature with depth. The degree of darkening increases with decreasing dielectric constant, as is evident in comparisons between this figure and Figures 5 and 6.

dry snow, of very dry soils such as those found on the Moon or in some deserts, and of dry, frothy volcanics.

The penetrating power of radiation in a dielectric depends upon the reciprocal of the loss, α . Decreasing α affects the brightness temperature by permitting radiation from greater depth to reach the surface. If the thermal temperature at depth differs from that at the surface, the emitted radiation will mirror that difference. Adding scatterers reduces the penetration power. Therefore, an anticipated increase in brightness temperature caused by a positive temperature gradient with depth might well be masked by scatterers. The extent of the masking is demonstrated in Figures 4, 5, and 6.

Radiation emitted from the specular surface of a homogeneous dielectric follows the law of darkening $[1 - R_p(\mu)]$. An integration of this directional emissivity over $1 > \mu > 0$ yields the hemispherical emissivity, e_p , for each polarization, p . e_H is slightly less than e_V and, therefore, the hemispherical reflectivity, $(1 - e_p)$, is slightly greater for H - than for V -polarized radiation. Radiation originating within the dielectric is reflected by the surface according to $(1 - e_p)$ and is reabsorbed by the dielectric. Scatterers, however, return some of the reflected radiation to the surface. Because reflected H -polarized radiation is slightly more intense than reflected V -polarized radiation, more H - than V -polarized radiation is returned to the surface causing ΔT_{BH} to be slightly less than ΔT_{BV} . The process is apparent in Figure 7.

The dependence, evident in Figure 7, of ΔT_{Bp} upon view angle derives principally from the directional emissivity $[1 - R_p(\mu)]$. Reducing ΔT_{Bp} by

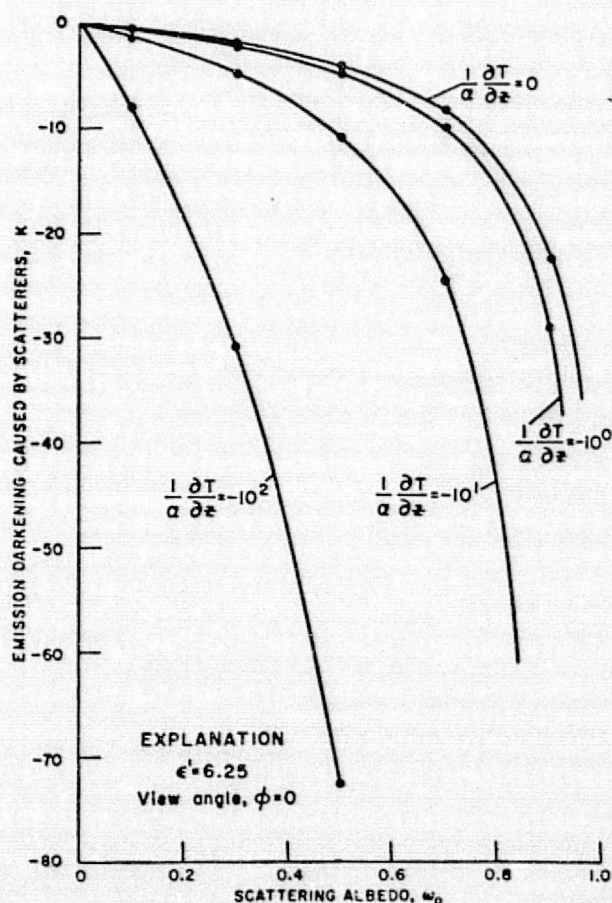


Fig. 5. Same as Figure 4, $\epsilon' = 6.25$.

$[1 - R_p(\mu)]$ reveals scatter-induced changes with polarization and view angle (Figure 8). Realistically, ΔT_{HV} and ΔT_{HH} should be equal at $\phi = 0$. The difference results from the assumed but artificial partition between polarizations, i.e., the scattering phase function, $P_{pq}(\mu, \mu')$, should have had off-diagonal terms. Because the hemispherical reflectivity, $(1 - e_p)$, is normally greater in H - than in V -polarization, more scattered radiant energy is stored in the H - than in the V -polarized radiation fields. Without off-diagonal terms in the scattering phase matrix, there is no opportunity for a natural adjustment and, consequently, the ΔT_{HP} differ anomalously. This anomaly disappears when the hemispherical reflectivities are equal, as illustrated by the curve, $\epsilon' = 1.0$, in Figure 8. The inference is, however, that $|\Delta T_{HV}|$ will tend to be greater than $|\Delta T_{HH}|$, and that the darkening in both polarizations will tend to be greater at larger view angles.

CONCLUSIONS

Scattering theory previously applied to atmospheric radiative transfer or to neutron scattering

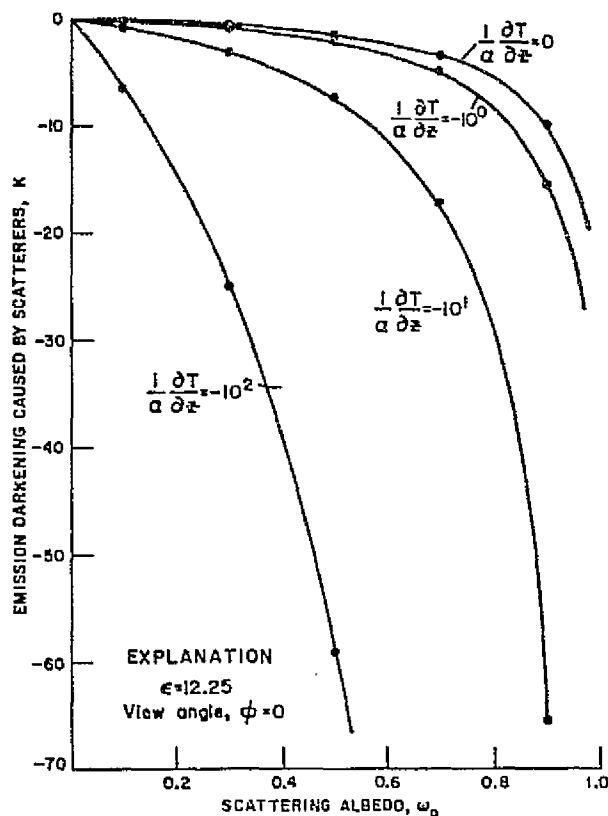


Fig. 6. Same as Figure 4, $\epsilon' = 12.25$.

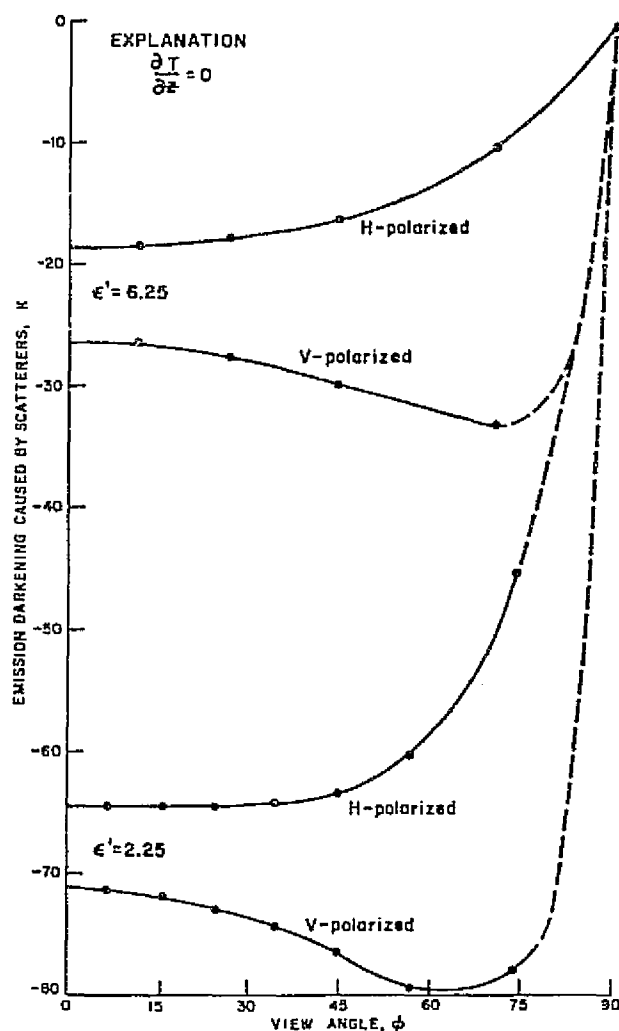


Fig. 7. Emission darkening caused by volume scattering as a function of view angle. Cases for two media are shown, one whose dielectric constant is 2.25 and another whose dielectric constant is 6.25. The general shape of the darkening law, $\Delta T_{np}(\phi)$, derives from the directional emissivity of a homogeneous halfspace, $[1 - R_p(\mu)]$.

can be modified to describe the volume scattering of microwave radiation within dielectrics. The limitations to this particular application result from the assumptions of partitioned, isotropic scattering, of randomly distributed scatterers, of far-field interactions (or, equivalently, of point scattering), and of a linear temperature variation with depth. Resulting salient inferences are: that the darkening can be many tens of degrees, that volume scatterers play a greater role the lower the dielectric constant, that the degree of darkening depends upon the dominance of scattering over absorption, that volume scatterers

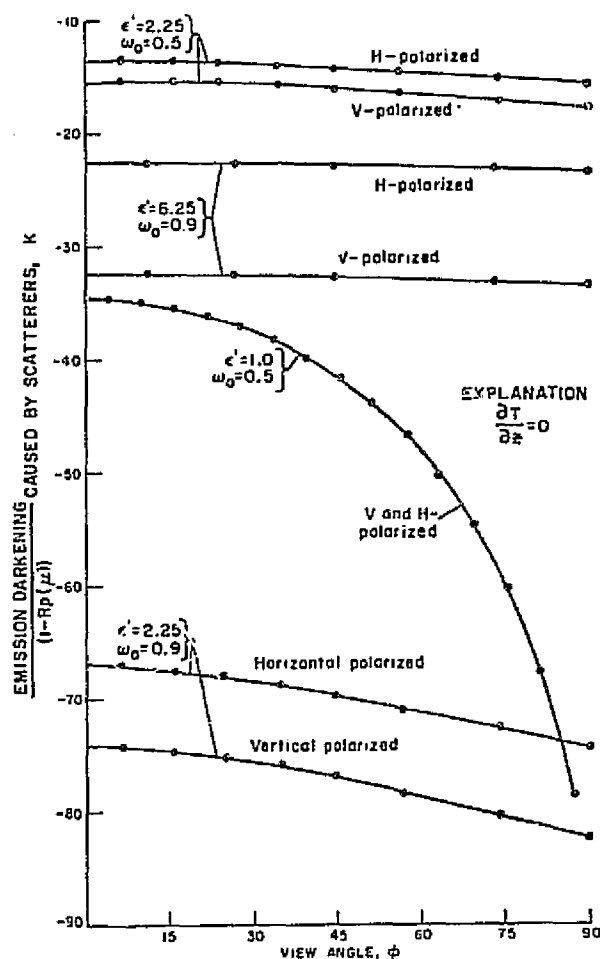


Fig. 8. The decrease in radiant energy available for emission as a function of view angle. The darkening, unmasked of its dependence upon directional emissivity, $[1 - R_p(\mu)]$, shows that relatively less energy is reaching the surface at the higher view angles. The effect is greater the lower the dielectric constant. $\Delta T_{hv}(0) \neq \Delta T_{hh}(0)$ is an artifact of the partition between polarizations within the scattering phase function. The anomaly diminishes with decreasing dielectric constant and disappears at $\epsilon' = 1.0$.

tend to mask the effects of a temperature gradient, that darkening tends to be greater for V - than H -polarized radiation, and that darkening increases with view angle. This solution, equation 27, represents the functional relationships between the brightness temperature, the concentration of scatterers, the complex dielectric constant, the surface temperature, and the thermal gradient.

Acknowledgments. I am most grateful to K. Watson, M. Meier, and W. Linlor for their discussions and comments on this manuscript.

REFERENCES

- Beckman, P., and A. Spizzichino (1963), *The Scattering of Electromagnetic Waves from Rough Surfaces*, pp. 239-291, Pergamon, New York.
- Blinn, J., J. Conel, and J. Quade (1972), Microwave emission from geological materials: Observations of interference effects, *J. Geophys. Res.*, 77, 4366-4378.
- Chandrasekhar, S. (1960), *Radiative Transfer*, pp. 70-88, Dover, New York.
- Edgerton, A., A. Stogryn, and G. Poe (1971), Microwave radiometric investigations of snowpacks, *Final Rep. 1285R-4*, pp. 2-14-2-23, Aerojet ElectroSystems Co., 1100 W. Hollyvale Str., Azusa, Calif. 91702.
- Love, C. (1966), Abscissas and weights for Gaussian quadrature for $N=2$ to 100, and $N=125, 150, 175, 200$, *Monogr. 98*, pp. 11-21, National Bureau of Standards, Washington, DC.
- Peake, W. (1959), Interaction of electromagnetic waves with some natural surfaces, *IRE Trans. Antennas Propagat.*, AP-7, S324-S329.
- Siegel, R., and J. Howell (1968), Thermal radiation heat transfer, Vol. I, *NASA SP-164*, pp. 65-71.
- Slater, J. (1939), *Introduction to Chemical Physics*, pp. 313-314, McGraw-Hill, New York.
- Stogryn, A. (1967), Electromagnetic scattering from rough, finitely conducting surfaces, *Radio Sci.*, 2, 415-428.
- Stogryn, A. (1970), The brightness temperature of a vertically structured medium, *Radio Sci.*, 5, 1397-1406.
- Stratton, J. (1941), *Electromagnetic Theory*, pp. 492-494, McGraw-Hill, New York.

REPRODUCIBILITY OF THE
ORIGINAL PAGE IS POOR

Part III, Final report of EREP Investigation 487

Branch of Petrophysics and Remote Sensing

"Made available under NASA sponsorship
in the interest of early and wide dissemination of Earth Resources Survey
Program information and without liability
for any use made thereof."

U.S. Geological Survey

Denver, Colorado 80225

DISCRIMINATION OF GEOLOGIC MATERIALS

USING SKYLAB S-192 DATA

by Howard A. Pohn

Introduction

The Skylab S-192 multispectral scanner has proved to be useful in the probable discrimination of several types of materials in the southwestern Nevada desert. Although the extremes in DN (density number) in any single channel are small, a comparison within and among channels has shown that five different types of materials can be distinguished.

Technique

An S-192 multispectral scanner tape (accession number 33-32882) for a portion of the U.S. Geological Survey Nevada test area (fig. 1) was supplied to us by the Johnson Space Center. This tape was reformatted using the U.S. Geological Survey DEC-1070 so as to be compatible with our Optronics Photomation 1700 write/scan microdensitometer. The images produced by the DEC-1070 were played back on film with the Optronics system using software written by the Remote Sensing Image Processing Group.

The images thus produced were compared with a geologic map of the area (Stewart and Carlson, 1974) and two or three test sites were selected for each of five different materials. The location of the test sites is seen on figure 2. The materials included basalt, andesite, welded ash flow tuff, playa and salt marsh deposits. The DN values (density number, values of brightness in a 256-step gray scale) for each test site were extracted from the tape, and means and standard deviations were determined for each of the channels. The results are given in Table 1.

Analysis

It can be seen that although, in most channels, the basalts cannot be distinguished from andesites, channels 1 and 17 (0.52-0.56 μm and 12.0-13.0 μm respectively) give a reasonably unambiguous set of densities which can be used to discriminate basalt from andesite. This observation is borne out by examining the laboratory spectral curves for the two materials in Hunt et al (1973, 1974). The curves show a relatively high reflectivity for andesite at 0.5-0.6 μm when compared with basalt. This is likely due to the higher percentage of ferric iron and concomitant reddish color observed on the surface of many andesites. The ambiguity of the rest of the characteristic spectra of andesites and basalts may well be because of the unusually low albedo of the andesites in this region (L. Rowan, personal communication). The higher DN for andesites in the daytime image at 12.0-13.0 μm is at present unexplained, but may be due to the lower percentage of mafic minerals

(and lower density) in the andesites. This would also cause the andesites to have a lower thermal inertia and suggests that they could be discriminated from basalts with thermal images.

Welded ash flow tuffs are easily distinguishable from basalts and andesites from the higher DN values of the tuffs at all wavelengths except for 1.09-1.19 μm where it is ambiguous.

A rather peculiar phenomenon occurs in the spectra of the playas and salt marshes. It can be seen that the spectra for playas are relatively higher than for salt marshes at all wavelengths from 0.46-1.03 μm . However, in the two channels from 1.09-1.75 μm this relationship is reversed. At still longer wavelengths the higher DN values of the playas persist.

The cause of this phenomenon is not known but the observations appear to be contrary to the expected result. The channel from 1.55-1.75 μm occurs at the edge of a water absorption band and it would be expected that a salt marsh (most probably a deposit of evaporites and muds containing a large amount of water) would have a lower DN value than a playa, which, in the Nevada desert, is typically a deposit of silts and clays with very low water content.

Qualifications.

The preceding statements must be qualified. First, the test areas have not been carefully examined in the field. Thus, it is difficult to say with certainty that we are detecting differences in playa and salt marsh deposits, because the compositions of salt marsh and playa

were inferred. Second, a sampling of two or three areas on a single Skylab image is not felt to be sufficiently representative to make a broad unequivocal statement as to the capability to discriminate materials using spectral information. And third, the calibrated Skylab S192 radiance values need to be correlated with field and laboratory spectra of the test areas to see if they are comparable.

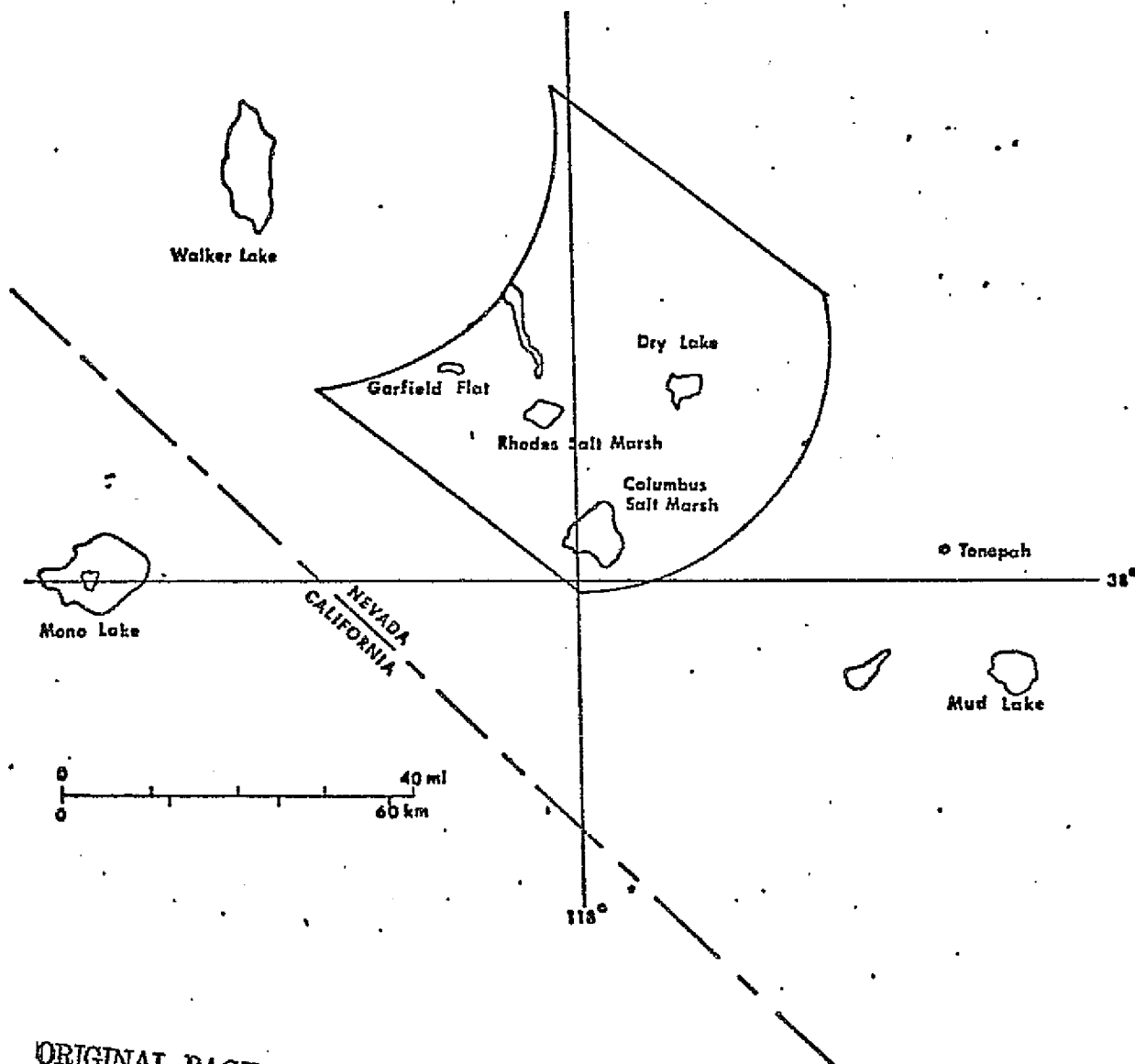
Figure 1 Location map of the U.S. Geological Survey
Nevada test area

Figure 2. Negative print of S-192 channel 5 (.62-.67 μm)
showing location of the test sites. B=basalt,
A=andesite, W=welded ash flow tuff, P=playa
S=salt marsh. Note: the incompatibility
between figures 1 and 2 is due to the fact that
the S-192 tape received by the USGS was not
corrected for the circular scan mode used on
board the spacecraft. There is extreme distortion
in the southwest; for this reason, no scale is
provided.

Table 1 Means and standard deviations in DN for the test
sites. (0 is dark, 255 is bright).

References Cited

- Hunt, G.R., Salisbury, J.W., and Lenhoff, C.J. 1973, Visible and near-infrared spectra of minerals and rocks-VIII. Intermediate igneous rocks: Modern Geology, v.4, pp 237-244.
- 1974, Visible and near infrared spectra of minerals and rocks: IX. Basic and ultrabasic igneous rocks, Modern Geology, v.5, pp 15-22.
- Stewart, J. H., and Carlson, J.E., 1974, Preliminary geologic map of Nevada, U.S. Geological Survey Miscellaneous field studies, MF-609.



ORIGINAL PAGE IS
OF POOR QUALITY

Fig. 1

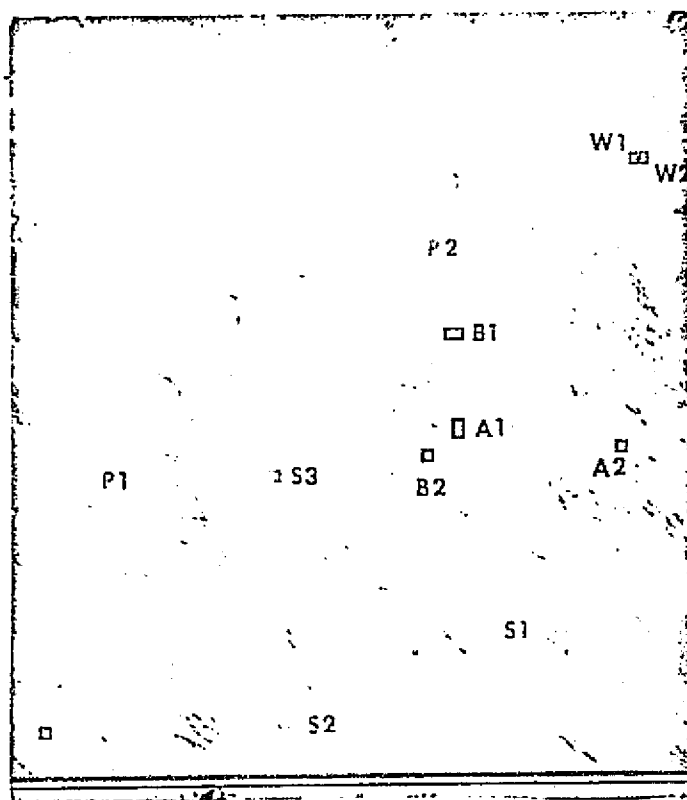


Fig. 2

ORIGINAL PAGE IS
OF POOR QUALITY

Table 1

Channel	18		1		3		5		7		9		19		20		11		13		21		17	
(1-3)	.46-.51		.52-.56		.56-.61		.62-.67		.68-.76		.78-.88		.98-1.05		1.09-1.19		1.55-1.75		2.10-2.35		10.2-12.5		12.0-13.0	
	N	σ	N	σ	N	σ	N	σ	N	σ	N	σ	N	σ	N	σ	N	σ	N	σ	N	σ	N	σ
Basalt 1	29.8	4.6	43.1	4.3	30.9	6.1	41.8	4.7	25.3	3.7	38.3	3.9	35.0	5.6	156.0	6.1	26.3	6.3	33.1	5.6	50.0	5.2	77.2	4.9
Basalt 2	21.7	4.4	40.4	2.6	27.4	5.8	34.3	5.5	20.2	3.4	23.9	4.0	25.5	4.1	152.3	6.3	19.6	4.8	25.0	5.7	46.6	5.4	81.4	5.0
Andesite 1	28.3	4.3	47.5	4.1	33.9	6.3	43.7	6.9	25.2	3.5	29.3	3.1	32.8	4.5	150.5	8.4	27.2	4.5	30.5	4.9	49.3	5.4	80.9	5.6
Andesite 2	32.7	6.3	47.7	3.8	37.3	6.1	47.1	10.3	30.0	4.6	30.3	7.0	38.0	6.3	152.6	9.3	27.2	7.0	35.3	8.1	52.5	6.3	97.3	6.1
Basalt Ash 1	41.4	4.8	58.9	4.3	46.0	7.2	67.1	7.6	37.8	4.6	42.4	4.6	50.4	5.4	155.2	6.0	37.2	5.2	46.2	6.5	59.5	5.2	94.8	5.5
Basalt Ash 2	40.0	5.9	58.0	4.3	44.4	6.9	65.5	7.5	38.4	5.4	40.7	5.2	50.8	6.7	155.0	8.1	37.2	6.4	45.6	8.2	59.2	5.4	94.8	5.5
Diase 1	49.8	6.1	92.0	5.3	84.9	6.5	110.3	6.4	63.3	3.5	66.3	2.9	76.0	5.9	141.0	4.4	53.3	5.4	71.8	5.2	71.7	6.0	111.7	7.5
Diase 2	61.2	1.2	81.7	3.7	76.7	6.3	105.3	5.0	59.2	3.3	63.8	2.2	74.8	4.6	146.1	5.3	55.6	4.9	69.7	4.5	69.5	5.5	120.6	5.7
Wet Marsh 1	59.2	5.2	86.0	6.2	72.8	7.0	101.9	8.5	58.5	5.1	60.5	4.4	68.4	5.8	151.6	4.6	61.6	5.2	67.2	6.6	73.2	6.5	131.9	6.0
Wet Marsh 2	60.8	5.7	77.0	6.3	69.6	8.1	95.1	7.5	55.8	4.2	63.2	3.1	69.2	4.2	151.9	4.7	59.3	5.7	67.7	4.6	70.6	6.4	119.8	8.6
Wet Marsh 3	59.4	4.5	80.0	4.6	68.8	7.6	95.3	5.8	53.8	3.9	60.1	3.0	65.7	3.6	153.7	5.1	52.6	4.9	62.8	5.1	68.3	5.5	121.3	6.0

REPRODUCIBILITY OF THE
ORIGINAL PAGE IS POOR